EFFECT OF THE HOLLOW TOPOLOGY ON THE LOCAL SPIN DYNAMICS IN MAGNETIC IRON OXIDE NANOPARTICLES

Martina Basini

Università degli Studi di Milano
2017

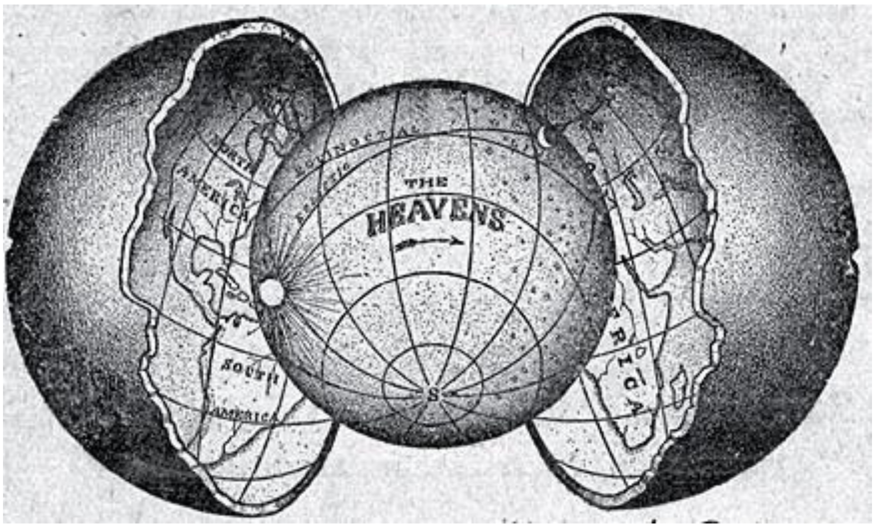

A Nic, senza il quale l'amore per la vita, per la fisica e per me stessa non esisterebbe. Grazie per avermi permesso di guardare il futuro.

Alla Prof. Lentini, grazie alla quale tutto ebbe inizio. Per aver saputo così abilmente tentarmi "nel peccato originale" di voler mettere a nudo la realtà tramite lo studio della fisica.

Al nonno Gianluigi che mi ha sempre guidato con saggezza in questo mondo troppo veloce attraverso le sue pungenti storie e filastrocche poco riservate.

Alla mia mamma per l'infinito amore e supporto che mi ha dimostrato durante tutta la vita e che continua ancora oggi. Per metà del cervello e per tutto il senso del dovere che ho ereditato da lei, senza il quale non avrei mai potuto raggiungere il grado di istruzione che mi ha portato a scrivere questa tesi.

Al mio papà "autorevole" che da dietro le quinte è riuscito ad essere protagonista di molte tra le mie scelte che hanno portato a questo successo, ma non solo. Oltre a questo lo ringrazio per l'altro mezzo cervello e per la vena artistica che ho ereditato da lui e che mi ha sempre permesso di immaginare la fisica come un vero scopritore.

A Toto-fratello-amico per avermi sempre voluto bene e per aver sopportato con eleganza le ingerenze di una sorella prevaricatrice. Oltre a questo lo ringrazio del supporto che è stato cruciale nei momenti difficili che solo noi fratelli conosciamo.

Alla zia Aluccia che mi ha dimostrato che non si è mai troppo grandi per crescere e che, con il suo esempio, mi ha dato la forza di cambiare me stessa in meglio.

A Paolo e Mario due chimici-fisici-tuttologi, amici e collaboratori che mi hanno sempre saputo consigliare con saggezza e onestà se pur in momenti diversi ma equivalentemente importanti della mia carriera. Vi voglio bene.

A Fra, ex addestratore di tigri e ora collega, grazie di avermi saputo spiegare (a volte anche senza usare le parole) quali sono le nostre priorità all'interno del mondo moderno. Confido sempre nell'azoto in spiaggia.

A Tomas, amico, collega e mentore a cui devo gran parte della conoscenza della tecnica sperimentale che oggi mi ha portato qui. Oltre a questo lo ringrazio delle lezioni che ha tenuto per me sulla birra..e perché no, anche sull vita. Ho imparato molto.

Ad Alessandro per le enormi possibilità di crescita personale e professionale che mi ha offerto e che ho cercato di sfruttare al meglio se pur evitando accuratamente i consigli di fede calcistica.

Grazie professore, è tutt'oggi un onore lavorare con lei, che nonostante l'acuta indole, fa parte di quella razza ormai rara chiamata "gente per bene"

Grazie a tutti

Overview and introduction

Due to their peculiar properties, the spin dynamics of confined magnetic materials has nowadays reached great interest both in fundamental and applied physics. Among them, the iron oxides magnetic nanoparticles (MNPs) have been widely investigated, and particular attention was devoted to the effects of the magnetic core size and the spin topology, in order to correlate all possible physical mechanisms active at the nanoscale to their macroscopic properties. The great interest arised from the possibility to synthesize MNPs well-defined in size and shape is due not only to their several applications (e.g. photonics, catalysis, magnetic recording, biological sensing, and biomedical applications such as targeting, drug delivery, magnetic fluid hyperthermia and MRI contrast agents), but also to the new fundamental physics that they show. In particular these systems display different thermally activated magnetic phases (spin glass, ferrimagnetism, superparamagnetism) that are consequence of the competition between mainly the exchange coupling, the surface effects and the interparticle interactions. Such competition is driven by the available thermal energy and leads to different regimes of spin dynamics.

Even though the dynamics in iron oxide MNPs have been investigated over the past 20 years, its complete knowledge is still unreached, in particular when surface effects are included. The effect of the spin disorder near the surface in full iron oxide MNPs is indeed not easy to be detected experimentally, due to the low number of surface spins compared to the core ones. Moreover, even if an excellent control of the crystallinity and the size distribution has recently been achieved, different synthesis procedures strongly affect the properties and the thickness of the surface spins corona.

In this thesis we propose the idea of increasing the surface to volume ratio by the synthesis of “hollow” magnetic nanoparticles (HMNPs) in order to enhance the chance to observe the dynamics of surface spins. Despite the interest on the hollow geometry which could lead to great advantages not only in biomedical application but also in sensoristics, only few works are focused on the static magnetic properties of hollow nanoparticles (see chapter 1) and still no work in literature is dedicated to their spin dynamics

Common experimental techniques to investigate spin dynamics in MNPs are AC susceptibility , Mössbauer spectroscopy, neutron scattering, nuclear magnetic resonance (NMR) and muon spin relaxation (MuSR). In particular, the application of NMR and MuSR to the study of the magneto-dynamics in MNPs is growing and nuclear and muon spin relaxation behaviour helps to unravel the temperature and field behavior of the electronic spin correlation times, thus giving access to local spin dynamics.

In this thesis we present a full investigation of the magnetic properties and of the NMR and MuSR dynamic parameters on 5 hollow and 2 full nanoparticles samples, the full ones used as reference for the “core” spin dynamics.

The first chapter proposes an overview of the state-of-the-art on superparamagnetic iron oxide full nanoparticles and few theoretical and experimental works on hollow systems.

The second chapter contains the morphological characterization (TEM images and size distributions) of the investigated samples together with the static magnetic characterization as a function of temperature (ZFC/FC curves) and of the external magnetic field (hysteresis). Experimental data showing the presence of two spin populations in the hollow samples are here presented, analysed and discussed. The two spin populations were ascribed to the surfaces (paramagnetic) and the core (superparamagnetic) spins.

The third chapter is devoted to the spin dynamics characterization of the investigated samples through nuclear magnetic resonance (NMR) relaxometry studies. The first part of the chapter contains general information on the fundamentals of the NMR technique and a description of the technical details of the main instrumentations. Experimental NMR-dispersion curves (NMR-D) are then presented in a wide frequency range (10^4-10^7 Hz). The experimental data of HMNPs show the presence of an extra contribution to the relaxation rates which was ascribed to the surface spins (inner and outer). The longitudinal relaxivities were successfully analysed by means of a novel phenomenological model accounting for the two spin populations (surface and core spins), here proposed for the first time. The fit of the NMR-D allowed the estimation of the

SPM spin dynamics correlation times and the PM hyperfine coupling constant. The description of the transverse relaxivity still remains a challenge for the future.

The fourth chapter is devoted to the spin dynamics characterization of the investigated samples through muon spin resonance (MuSR) experiments performed at the Paul Scherrer Institute facility, Villigen, Switzerland. The first part of the chapter contains general information on the fundamental concepts of the MuSR technique and a description of the technical details of the main instrumentation. The dynamics of one full and one hollow sample as seen in the muon time window (10^5-10^8 Hz) under the application of an external longitudinal magnetic field is then presented. The evolution of the dynamics was studied as a function of temperature in a wide range (2-300K). The temperatures at which the muon's relaxation rate exhibits a maximum (T_B^{μ}) were compared with the temperature of the maximum in the ZFC (T_B^{ZFC}) curves presented in chapter 2. The relaxation rates as a function of temperature were successfully analysed by means of a BPP model and the spin dynamics correlation times and hyperfine constants were evaluated. Moreover, the experimental observation of the internal magnetic field generated by the freezed spins at $T< T_B^{\mu}$ is presented here for the first time in literature. The dependence of the internal magnetic field temperature was fitted by means of a mean-field-like model with a variable critical exponent.

No clear observation of the two spin populations is evident in the experimental data, even if the mismatch between the experimental data and the BPP fits at low temperature could tentatively be ascribed to the presence of the surface spins.

In conclusion the work presented in this thesis suggests a possible interpretation of mechanism underling both static and dynamic properties of a class of hollow magnetic nanoparticles, and significantly contributes to the study of systems of interest for potential applications in nano-medicine.

CHAPTER 1
SUPERPARAMAGNETISM: Fundamentals and hollow geometry

Overview

The main purpose of this chapter is to resume the models and previous experiments to which we will refer in the next chapter. In particular it is proposed an overview of the state-of-the-art on superparamagnetic iron oxide "full" nanoparticles and few theoretical and experimental works which are known until now regarding the hollow ones.

The goal of this thesis is to understand the effect of surfaces on the thermodynamics and on the static magnetic properties of hollow nanoparticles and subsequently on their dynamics. This requires an approach which accounts for the local enviroment inside the particle, the interactions such as dipole-dipole and exchange ones, other than the magnetocrystalline bulk and surface anisotropy. In the following, first we studied the magnetic static properties before investigating the dynamics.

I. Introduction to nanomagnetism

I.i Magnetism in condensed matter

In condensed matter, atomic magnetic moments can mutually act together (*cooperative magnetism*), leading to a variety of behaviors from which it can be deduced if all magnetic moments are reciprocally isolated (*noncooperative magnetism*). The atomic magnetic moments can be coupled together with different types of magnetic interactions, leading to a rich variety of magnetic properties in real systems [1–4]. On the other hand the two basic types of noncooperative magnetism are paramagnetism and diamagnetism.

Paramagnetism arises from identical, uncoupled atomic moments located in an isotropic environment. Hence, in a paramagnetic material, there is no long range order and the magnetic moments tend to align under an external magnetic field.

Diamagnetism, which is always present in the matter, is due to the reaction of the atomic inner electrons to the external magnetic field [4, 5]: it is manifested by the insurgence of a local field opposite to the external one.

In a cooperative magnetic system, the interactions between adjacent magnetic moments determine the kind of magnetic order in the material. Among the different interactions, the exchange interaction is generally the dominant one. Two classes of exchange interactions can be distinguished, i.e. direct and indirect exchange interaction. *Direct exchange* occurs between moments that are close enough to have a significant overlap of their wave functions, whereas i*ndirect exchange* arises when the atomic magnetic moments are coupled over relatively large distances. The interaction can be mediated also by a nonmagnetic ion that is placed in between the magnetic ions (e.g., oxygen atoms in oxides), and in this case it is called *superexchange* [2]. Generally speaking, the exchange interaction between magnetic centers in a three-dimensional solid can be quantitatively described by the Heisenberg spin Hamiltonian[2]:

$$H_{exc} = -2\sum_{i,j} J_{ij}\ \boldsymbol{s}_i \cdot \boldsymbol{s}_j$$

where J_{ij} is the exchange integral describing the magnitude of coupling between the spins $\boldsymbol{s}_{\mathbf{i}}$ and $\boldsymbol{s}_{\mathbf{j}}$. If the exchange integral has a positive value, below a critical temperature T_{C} (*Curie temperature*), the magnetic moments align parallel to each other and the substance is said to be *ferromagnetic* (FM). Above T_{C}, the material is no longer FM but reverts to paramagnetic because the thermal energy becomes higher than the exchange energy, destroying the magnetic order. On the contrary, if J_{ij} is negative, the spins are aligned antiparallel to each other, and below a critical temperature called *Néel temperature* (T_N) the material is said to be *antiferromagnetic* (AFM), if the total magnetic moments is zero and the moments are perfectly compensated or *ferrimagnetic* (FiM), if there is no compensation due to some difference between the individual moments pertaining to each sub-lattice. Then, in principle, magnetic properties in condensed matter can be explained by different kinds of magnetic coupling that are closely related also to the chemical composition and crystalline structure of the material [6-7].

Minimization of energy provides a basis for predicting the direction of events in the universe. This is why a bulk cooperative magnetic system, to minimize its energy, organizes in a certain number of small regions, with different sizes and shapes, called domains, that is, uniformly magnetized regions having atomic magnetic moments oriented in the same direction [8]. Two adjacent domains are separated by transition regions, called *domain walls*, in which the spins gradually rotate coherently or incoherently * from one domain to the other. In an unmagnetized FM or FiM material, magnetic domains have random directions so that the sum of the overall domain moments is essentially zero [2].

When placed in a sufficiently large external magnetic field, the spins in each domain rotate and align parallel to the direction of the applied field. Typically, magnetization increases sharply at low field, as the domains with a more favorable alignment expand at the expense of others, and saturate when the maximum domain alignment is reached (see Figure 1.a; inset). This corresponds macroscopically to a plateau region of the magnetization curve (saturation magnetization, M_s), and when the applied field is decreased the magnetization also decreases. The magnetization remaining at zero-applied field is called remanent magnetization (M_r). Very often, for the characterization of a magnetic hysteresis, the reduced remanent magnetization, defined as M_r/M_s, is also used. The magnetic field to which corresponds a magnetization equal to 0 is called coercive field, or coercivity (H_c) (Figure1b) [9-10].

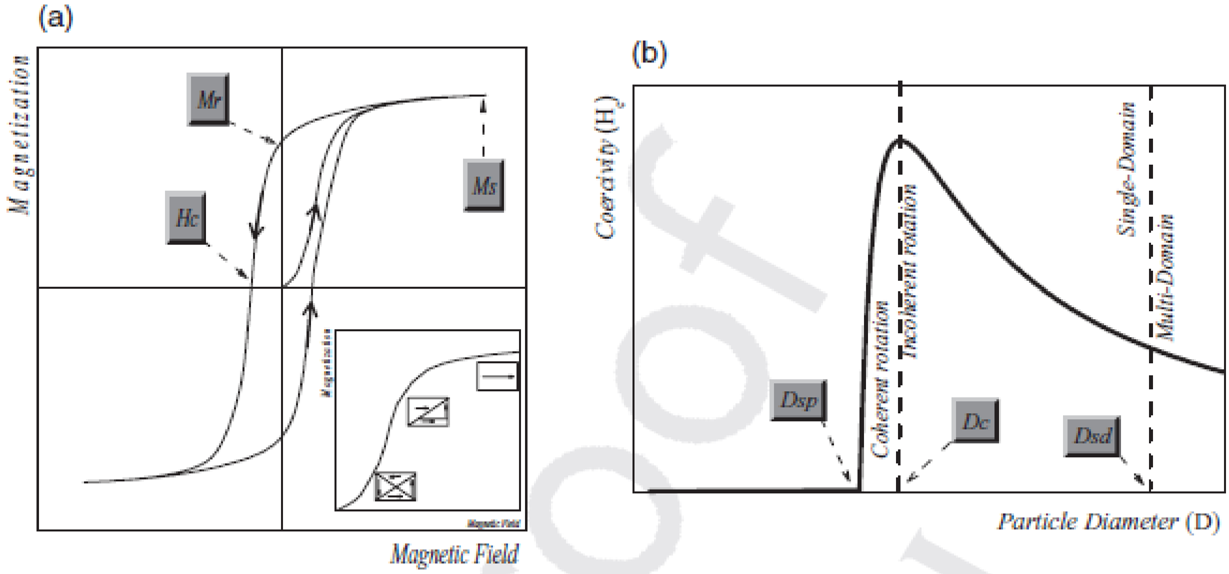

Figure 1 (a) Magnetization beahviour as a function of the external applied field; (b) cohercive field as a function of the particle diameter.

All the magnetic properties are strictly dependent on the particle size, and a new physical world opens up when the materials are nanoscaled.

---

* In the coherent rotation mode, all spins remains parallel to each other, whereas in the incoherent reversal mode a nonuniform magnetization process occurs

An experimental investigation of the dependence of coercivity on particle size is shown schematically in Figure 1.b.

Below a certain critical particle size (D_{sd}), a magnetic multidomain structure is not energetically favored and particles with dimension below this size therefore consist of a single magnetic domain. Typical D_{sd} values for magnetic iron oxides are ~160 nm for γ-Fe_2O_3 and ~130 nm for Fe_3O_4 [11]. Generally, the rotation of the spins (i.e., the reversal process) occurs at high field by incoherent rotation of the spins, and this leads to an increase of coercivity with respect to a multidomain structure. For smaller particles, below a given size (D_c) depending on the material, the rotation is coherent and this induces a decrease in the coercivity.

One of the fundamental motivations for the investigation of magnetic nanomaterials is the impressive change of magnetic properties that occurs when the critical length governing some phenomena is comparable to the size of the nanoparticle. Changes in the magnetization of a material occur via activation over an energy barrier, and each physical mechanism responsible for an energy barrier has an associated length scale. The fundamental magnetic lengths for magnetic materials mainly include the crystalline anisotropy length, l_K, the applied field length, l_H , and the magnetostatic length, l_S, as defined below [12]:

$$l_K = \sqrt{J/K} \qquad l_H = \sqrt{2J/HM_S} \qquad l_S = \sqrt{J/2\pi M_S^2}$$

where K is the anisotropy constant of a bulk material due to the dominant anisotropy, and J is the exchange within a grain. The fundamental magnetic lengths for most magnetic materials are on the order of 1–100 nm. If there is more than one type of energy barrier, the magnetic properties of the magnetic material are dominated by the shortest characteristic length which is often the anisotropy one.

In bulk materials, magnetocrystalline and magnetostatic energies are the main sources of anisotropy. In nanosystems the source of anisotropy can be summarized as follows.

Magnetocrystalline anisotropy: this property is intrinsic to the material, being related to the crystal symmetry and to the arrangement of atoms in the crystal lattice. Magnetocrystalline anisotropy can show various symmetries, but uniaxial and cubic ones cover the majority of cases.

Magnetostatic anisotropy (shape anisotropy): this contribution is due to the presence of free magnetic poles on the surface of a magnetized body. The poles create a magnetic field inside the system, the demagnetizing field, which is responsible for the magnetostatic energy. For a particle with finite magnetization and nonspherical shape, the magnetostatic energy will be larger for some orientations of the magnetic moments than for others. Thus, the shape determines the magnitude of magnetostatic energy and this type of anisotropy is often known as shape anisotropy [13]. Particle shape has been identified as a major tool for engineering the magnetic properties of nanomaterials, with additional attractive feature of displaying different properties in different directions [14,15]

Surface anisotropy: the surface atoms have a lower symmetry compared to that of atoms within the particle. This gives rise to surface anisotropy, which increases with the increase in surface-to-volume ratio (i.e., a decrease in particle size)[16]. Surface anisotropy is also strictly related to the chemical and/or physical interactions between surface atoms and other chemical species. The coating and functionalization of the nanoparticle surface can induce important modifications in its magnetic properties, which are mainly due to the surface spin canting induced by the coating ligands [17,8].

Dipolar energy anisotropy: mutual anisotropy induced by the dipolar coupling between intra and inter crystals spins, which is still a controversial issue [19,20].

I.ii Nanomagnetism: theoretical approach

In this section we describe the Hamiltonian and introduce the basic notions of the induced and the intrinsic magnetization in small systems (i.e. magnetic nanoparticle).

Within the classical approssimation it is convenient to represent the atomic spin as the three-component spin vector $\boldsymbol{s_i}$ of unit length on the lattice site i. The Hamiltonian in general includes the exchange interaction, the Zeeman energy , the magneto-crystalline anisotropy energy, and the energy of dipole-dipole interactions (DDI):

$$H = -2\sum_{i,j} J_{ij}\ \boldsymbol{s}_i \cdot \boldsymbol{s}_j - \mu_0 \boldsymbol{H} \cdot \sum_i \boldsymbol{s}_i + H_a + H_{DDI}$$

(1)

As previously discussed, the magnetocrystalline anisotropy can have mutiple symmetries even if the uniaxial and cubic ones cover the majority of cases.

The Hamiltonian for the magneto-crystalline uniaxial anisotropy can be written $H_a{}^{uni} = -\sum_i K_i(\boldsymbol{s}_i \cdot \boldsymbol{e}_i)^2$ with easy axis $\boldsymbol{e}_i$ and constant $K_i > 0$.. This anisotropy model can be used to describe surface effects if one attributes the same easy axis and the same anisotropy constant K_c for all core spins, and different easy axis and anisotropy constants to the surface spins. Within the simplest transverse surface anisotropy (TSA) model all surface spins have the same anisotropy constant K_S, whereas their easy axes are perpendicular to the surface . More realistic is the Néel surface anisotropy (NSA) model [20]

$H_a{}^{NSA} = -L\sum_i \sum_{j=1}^{z_i} \left(\boldsymbol{s}_i \cdot \boldsymbol{e}_{ij}\right)^2$, $\boldsymbol{e}_{ij} \equiv \boldsymbol{r_{ij}}/r_{ij}$, $\boldsymbol{r_{ij}} \equiv \boldsymbol{r_i} - \boldsymbol{r_j}$

where z_i is the coordination number of state i that for the surface atoms is smaller than the bulk value z, and $\boldsymbol{e}_{ij}$is the unit vector connecting site *i* to its nearest neighbors *j*.

The hamiltonian for the magneto-crystalline cubic anisotropy can be written $H_a{}^{cub} = -K^{(cub)}\sum_i (s_{ix}^2 + s_{iy}^2 + s_{iz}^2\,)$ for $K^{(cub)} > 0$ the energy has minima for six orientation of type [100] and maxima for eight orientations of type [111].

Since the Hamiltonian (1) describes the total energy, it drives the motion of the spin system such as the magnetization dynamics. In particular we will refer to the magnetization "reversal" as the macroscopic evidence of the local spin dynamics in nanostructured materia. In figure (2) the principal reversal mechanism as a function of the number of magnetic moments in a magnetic system (roughly corresponding to the number of atoms) are resumed.

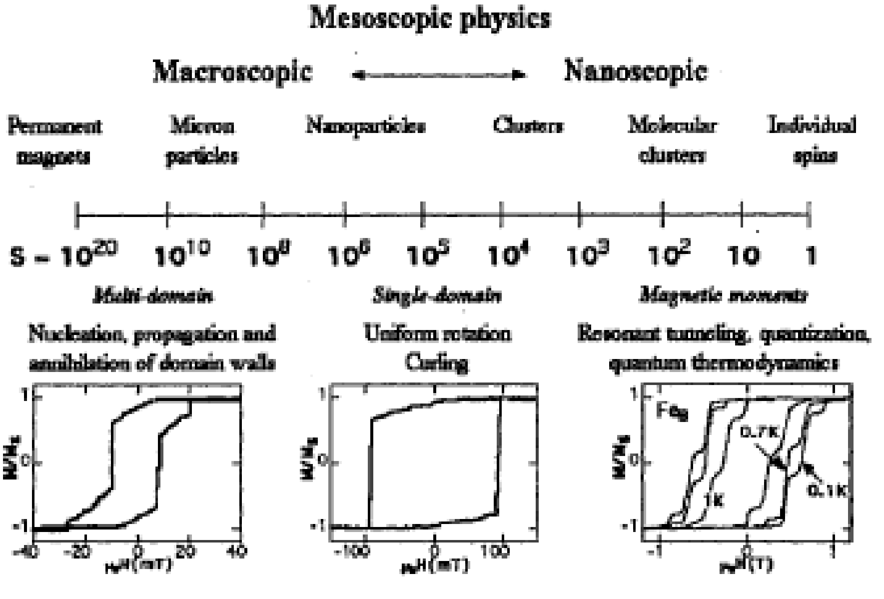

Figure 2 Scale size of magnetic systems, going from macroscopic down to nanoscopic ones. The unit of measure of this scale is the number of magnetic moments in a magnetic system. The hysteresis loops are typical example of magnetization reversal via nucleation, propagation and annihilation of domain walls (left), via uniform rotation (middle), and via quantum tunneling (right).

When the magnetization is in the so called single domain state its direction can be along a fixed nuber of directions (depending on the magnetocrystalline anisotropy) and it might reverse by uniform rotation, curling or other nonuniform modes. For systems of size well below the domain wall width or the exchange length, one must thake into account explicitly the magnetic moments (spins) and their couplings. The theoretical description is complicated by the particle's boundary. In the next paragraphs we review the most important theories and experimental results concerning the magnetization reversal of single domain nanoparticles.

I.iii Magnetization reversal at zero kelvin: uniform rotation

For the smallest single-domain particles the magnetization is expected to reverse by uniform rotation if no thermal energy is available. The model of uniform rotation developed by Stoner and Wohlfarth (SW) [46] and Néel [47] is the simplest classical model describing the magnetization reversal. One considers a particle of an ideal magnetic material where the exchange coupling holds all spins tightly parallel to each other, and the magnetization magnitude does not depend on the space. In this case the exchange energy is constant, and it plays no role in the energy minimization. Consequently there is competition only between the anisotropy energy of the particles and the effect of the applied field. The original model of SW assumed only uniaxial shape anisotropy with one anisotropy constant that is one second-order term. However real systems are often quite complex and the anisotropy is a sum of mainly shape, magnetocrystalline and surface anisotropy. One additional complication arises because the different anisotropies favor the magnetization alignment in different directions. All these facts motivated a generalization of the SW model for an arbitrary effective anisotropy which was done by Thiaville in 1998 [21,22].

One suppese that the exchange interaction couples all the spins strongly together to form a giant spin whose direction is described by the unit vector $\vec{m}$. The only degrees of freedom of the particle's magnetization are the two angles of orientation of $\vec{m}$. The reversal of the magnetization is described by the potential energy

$$E(\vec{m},\vec{H}) = E_0(\vec{m}) - \mu_0 V M_s \vec{m}\cdot\vec{H}$$

(2)

Where V and M_s are the magnetic volume and the saturation magnetization of the particle respectively, $\vec{H}$ is the external magnetic field and $E_0(\vec{m})$ is the magnetic anisotropy energy which is given by

$$E_0(\vec{m}) = E_{Shape}(\vec{m}) + E_{MC}(\vec{m}) + E_{Surf}(\vec{m})$$

(3).

E_{Shape} is the magnetostatic energy related to the shape, E_{MC} is the magnetocrystalline anisotropy (MC) arising from the coupling of the magnetization with the crystal lattice, similar to the bulk-case and E_{Surf} is due to simmetry breaking and surface strains; - $\mu_0 V M_s \vec{m}\cdot\vec{H}$ represents the Zeeman interaction.

I.iv Magnetization reversal: the influence of temperature

The thermal fluctuations of the magnetic moment of single-domain ferromagnetic particles and its dacay toward thermal equilibrium were introduced by Nèel [23,24] and further developed by Bean and Livingston [25,26] and Brown [27,28,29]. The simplest case is an assembly of indipendent particles having no magnetic anisotropy. In the absence of an applied magnetic field, the magnetic moments are randomly oriented. The situation is similar to paramagnetic atoms where the temperature dependence of the magnetic susceptibility follows a Curie behaviour, and the field dependence of magnetization is described by the Brillouin function. The only difference is that the magnetic moments of the particles are much larger than those of the paramagnetic atoms. Therefore, the quantum mechanical Brillouin function can be replaced by the classical limit for larger magnetic moments, namely the Langevin function (i.e. $L(x) = coth\left(\frac{\mu H}{k_B T}\right) - \frac{k_B T}{\mu H}$). This theory is called superparamagnetism. The situation changes as soon as the magnetic anisotropy is present and one or more preferred orientations of the particle's magnetization are established. In the Néel and Brown model of thermally activated magnetization reversal, a magnetic single-domain particle has an uniaxial anisotropy and consequently two equivalent ground states of opposite magnetization separated by an energy barrier which is due to shape and crystalline anisotropy. The system can switch from one direction to another by thermal activation over the energy barrier. Just as in the SW model, they assumed uniform magnetization and uniaxial anisotropy in order to derive a single relaxation time. Néel supposed further that the energy barrier between the two equilibrium states is large in comparison with the thermal energy $k_B T$ which justify a discrete orientation approximation [23,24]. Brown went further and cosidered the magnetization vector in a particle to wiggle around an energy minimum, then jump to the vicinity of another minimum, then wiggles around there before jumping again. He supposed that the orientation of the magnetization can be described by a Gilbert equation $\frac{d\boldsymbol{M}}{dt} = \gamma(\boldsymbol{M} \times \boldsymbol{H_{eff}} - \eta \boldsymbol{M} \times \frac{d\boldsymbol{M}}{dt})$ with a random field term that is assumed to be a white noise. On the basis of this assumption, Brown was able to derive a Fokker-Planck equation for the distribution of magnetization orientations. However Brown did not solve the equation but tried some analytical approximations. More recently Coffey *et al.* [30,31] found by numerical methods an exact solution of Brown's differential equation for uniaxial anisotropy and an arbitrary applied field direction. They also derived an asymptotic general solution for the case of large energy barriers in comparison to the thermal energy $k_B T$. This solution is of particular interest for single-particle measurements and is reviewed by the following.

Lets consider a general asymmetric bistable energy potential $E = E(\vec{m}, \vec{H})$ of equation (2) with the orientation of the magnetization $\vec{m} = M/M_S$ ($M_S$is the spontaneous magnetization). Suppose that $E(\vec{m}, \vec{H})$ has minima $\overrightarrow{m_1}$ and $\overrightarrow{m_2}$ separated by a potential barrier. In the case $\beta(E_0 - E_i) \gg 1$ where $\beta = 1/k_B T$ and $E_i = E_i(\overrightarrow{m_i}, \vec{H})$ Coffey *et al.* showed that the longest relaxation time (the inverse of the longest relaxation time is determined by the smallest nonvanishing eingenvalue of the appropriate Fokker-Plank equation [30,31]) is given by the following equation which is valid for $\beta(E_0 - E_i) > 1$ (i.e. intermediate to high damping limit, IHD)

$$\tau^{-1} = \frac{\Omega_0}{2\pi\omega_0}\left[\omega_1 e^{-\beta(E_0 - E_1)} + \omega_2 e^{-\beta(E_0 - E_2)}\right]$$

(4)

Where ω_0 and Ω_0 are the saddle and damped saddle angular frequencies

$$\omega_0 = \frac{\gamma}{M_s}\sqrt{-c_1^{(0)} c_2^{(0)}}$$

$$\Omega_0 = \frac{\gamma}{M_s}\frac{\alpha}{1+\alpha^2}\left[-c_1^{(0)}-c_2^{(0)} + \sqrt{\left(c_1^{(0)}-c_2^{(0)}\right)^2 - 4\alpha^{-2}c_1^{(0)}c_2^{(0)}}\right]$$

ω_1 and ω_2 are the angular frequencies :

$$\omega_i = \frac{\gamma}{M_s}\sqrt{c_1^{(i)}c_2^{(i)}}$$

with i=1,2. $c_1^{(j)}$ and $c_2^{(j)}$ (j = 0,1,2) the coefficients in the truncated Taylor series of the potential at well and saddle points, that is the curvature of the potential at well and saddle points. γ is the gyromagnetic ratio, $\alpha = \eta\gamma M_s$ is the dimensionless damping foctor and η is the friction of in Gilbert's equation (ohmic damping).

In the low damping limit (LD), defined by $\beta(E_0 - E_i) < 1$ the longest relaxation time is given by [32,33]:

$$\tau^{-1} = \frac{\alpha}{2\pi}\left[\omega_1\beta(E_0 - E_1)e^{-\beta(E_0-E_1)} + \omega_2\beta(E_0 - E_2)e^{-\beta(E_0-E_2)}\right]$$

(5)

In this case, the energy dissipated in one cycle of motion in the well is very small in comparison to the thermal energy k_BT.

Experimentally relaxation is observed only if τ is of the order of magnitude of the measuring time of the experiment. This implies for all known single-particle measurements technique that $(E_0 - E_i) \gg 1$, that is, the asymptotic solutions (4) are always a very good approximation to the exact solution of Brown's Fokker-Planck equation [34]. In applied field, the condition $\beta(E_0 - E_1) \gg \beta(E_0 - E_2)$ (taking E_2 as metastable minimum) might become true. Then the first exponential in eq (5) can be neglected.

Concerning the possible value of α it has to be said that little information is available. Typical values should be between 0.01 and 5 [35]. Finally, we note that $c_1^{(j)}$ and $c_2^{(j)}$ (j = 0,1,2) can be found experimentally by measuring the critical surface of the switching field and applying the calculation of Thiaville (see section *I.iii*) [21].

II. Full maghemite (γ-Fe2O$_3$) nanoparticles

In this thesis we deal with the ferrimagnetic iron oxide nanoparticles composed by magnetite (Fe_3O_4) and/or maghemite (γ-Fe_2O_3).

II.i Magnetite (Fe_3O_4) and Maghemite (γ-Fe_2O_3) structure

Magnetite has a cubic crystal structure with the space group of Fd3m .Theoretically, the unit cell is made up of eight cubic units with a lattice *d*-spacing of 8.396 Å. It contains 56 atoms, including 32 oxygen atoms, 16 $Fe^{3+}$and 8 Fe^{2+} and may be denoted as $(Fe^{3+})^{tetr}{}_8[Fe^{3+}Fe^{2+}]^{oct}{}_8O_{32}$. In its unit cell as shown in figure 3, the oxygen anions form a closed-packed FCC lattice. Also, there is 32 octahedral (B site) and 64 tetrahedral (A site) sites in the unit cell. The Fe^{2+} cations occupy 1/4 of the octahedral interstitial sites (i.e. 8 Fe^{2+}) and Fe^{3+} onesevenly ll 1/4 of the octahedral (i.e. 8 Fe^{3+}) and 1/8 of the tetrahedral (i.e. 8 Fe^{3+}) sites. This crystallographic configuration is denoted inverse spinel.

From the magnetic moment configuration point of view, magnetite is categorized as ferrimagnetic materials. Its magnetic properties is reflected by the splitting of the 5d orbitals as visualized in figure 5. The 5d orbitals are split into two subsets due to the influence of oxide ligands, implying that all Fe^{3+}+ and Fe^{2+} ions have five and four unpaired electrons, respectively.

As can be seen, in the octahedral coordination, Fe^{3+} and Fe^{2+} ions are coupled ferromagnetically through a so called double exchange mechanism. The electron whose spin is directed in the opposite direction of the others and colored red, can be exchanged between two octahedral coordination. On the other hand, the Fe^{3+} ions in tetrahedral and octahedral sites are coupled antiferromagnetically via the oxygen atom, implying that the Fe^{3+} spins cancel out each other and thus merely unpaired spins of Fe^{2+} in octahedral coordination contribute to the magnetization. This magnetic moment configuration accounts for the ferrimagnetism seen in magnetite.

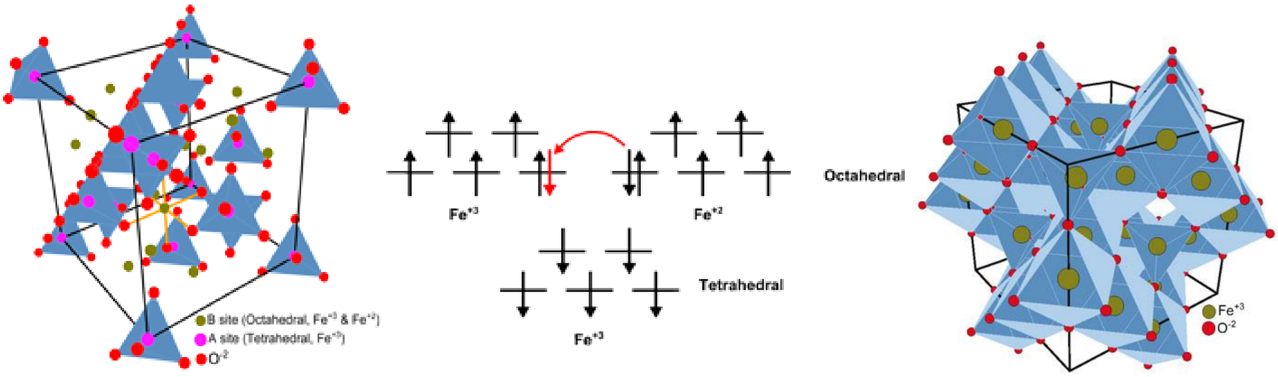

Figure 3 (a) Crystalline structure of magnetite and (b) electronic configuration of maghemite; (c) crystalline structure of maghemite.

Maghemite likewise to magnetite has a cubic crystal structure with the lattice *d*-spacing of 8.33 Å. As it can be deduced from its chemical formula γ-Fe_2O_3, there only exists Fe^{3+} cations which are arbitrarily distributed in 16 octahedral and 8 tetrahedral interstitial sites in the FCC packing of oxygen anions as shown in Fig.1. The Fe^{2+} cation vacancies ($\otimes$) are located in the octahedral sites and their arrangement in the maghemite structure plays a preponderant role in magnetic response of maghemite. When the vacancies are randomly distributed its space group is Fd3m and its formula unit may be written as $(Fe^{3+})_8^{tetr}\,[Fe^{3+}_{5/3}\otimes_{1/3}]_8^{oct}\,O_{32}$. The described crystal arrangement is known as normal spinel. Since the spins in the octrahedral and tetrahedral sites are oriented anti-parallel, maghemite is ferrimagnetic.

The magnetic response of an ensemble of maghemite/magnetite NPs is a combination of surface effects, finite size effects (i.e.truncation of the magnetic correlation length), and collective behaviors due to interparticle dipolar and/or exchange interactions. The primary exchange mechanism in ferrite compounds is an antiferromagnetic super-exchange interaction between metal cations mediated by an intervening oxygen ion. Because of the indirect nature of the coupling, the super-exchange interaction is sensitive to modified bond lengths and angles at a surface, and variation in coordination of surface cations will produce a distribution of net exchange fields.

II.ii Magnetite/Maghemite nanoparticles

In nanostructures, where the FM/FiM material size is reduced below a critical value, a magnetic single-domain state is energetically favored with respect to a multidomain one. As first calculated by Frenkel and Dorfman, there is a minimum domain size below which a FM material is expected to consist of a single magnetic domain [36] A more rigorous estimate of the critical radius r_c below which a magnetic nanoparticle with uniaxial anisotropy will be a single domain, is given by [37]:

$$r_c \approx \frac{9(AK_a)^{1/2}}{\mu_0 M_s^2}$$

(6)

where K is the anisotropy constant, M_s is the saturation magnetization, A is the exchange stiffness and μ_0 is the vacuum permeability. r_c depends on the material and is normally in the range of 5–1000 nm. For example, the critical radius for Fe is around 6 nm and for Fe_3O_4 it is around 60 nm. A magnetic monodomain particles (i.e. a particle that is in a state of uniform magnetization at any field) can be considered as a large magnetic unit (superspin for short) with a magnetic moment (μ) proportional to the volume $\mu \quad = M_sV$ expected in the range 10^3–10^5 Bohr magnetons (μ_B). However, such nanoparticle is also characterized by the instability of magnetization due to thermal agitation. For an isolated spherical particle with a uniaxial anisotropy, this results in the flip of magnetization between two antiparallel easy directions, separated by an energy barrier ΔE_a, that is proportional to the anisotropy constant $K_a$and to the volume V. Then, according to the Néel–Brown theory [38,39], above a certain temperature (i.e. blocking temperature, T_B) and on a certain time scale, the particle moment can make a thermally activated transition. This phenomenon is analogous to paramagnetism but, involving superspins, it is characterized by different time and magnetization scales, and for this reason it is called superparamagnetism (SPM). The energy of a magnetic particle is dependent on the magnetization direction, and for a uniaxial anisotropy nanoparticle with the external magnetic field (H) aligned along the easy direction, can be written as [39,40,41]:

(7)

$$E_a = K_aV(\sin\theta)^2 - M_sVH\sin\theta$$

where θ is the angle between the magnetization vector and the field direction and the other parameters have the same meanings previously defined. Below T_B, the particle's moment is blocked and unable to overcome the barrier in the time of a measurement; the system preserves the FiM behaviour and an open hysteresis is observed. From eq. (7) the height of the energy barrier can be written as:

$$\Delta E_a = K_aV\left(1 \pm \frac{H}{H_K}\right)^2, \quad \text{where} \quad H_K = \frac{2K_a}{M_s}$$

(8)

From equations (7) and (8) it emerges that the energy barrier ΔE_a, strictly dependent on the volume and on the anisotropy, is a key parameter in order to understand and to tune magnetic properties of nanoparticle-based magnetic systems.

II.iii Effect of the interparticle interactions

When interparticle interactions are non-negligible the behaviour of the system is substantially more complicated and the problem becomes non-trivial, even if the spins of the particle are assumed to be coupled to yield a super-spin moment. The main type of interactions that can be found in a fine-particle assemblies are:

(a) Dipole-dipole interparticle interactions (DDI), which always exist;

(b) Exchange interparticle interactions (EXI) through the surface of the particles which are in close contact (this contribution to the interparticle interactions will not be discussed in the following as it is out of the aims of this thesis);

(c) Interface intra-particle interaction (II) (i.e. interactions between two different magnetic phases which are both present in the NP);

In bulk magnetic materials, the order of magnitude of DDI for two magnetic atoms, with magnetic moments of few μ_B, in a crystal lattice separated by a distance between 0.1 and 1 nm, is around 10^{-23} J (~1 K). It is clear that the dipolar interaction is too weak to account for the FM or AFM ordering in condensed matter, since most of the magnetic materials have ordering temperatures that are much higher. On the other hand, in an assembly of superspins where each nanoparticle has a moment of about 10^3–10^5 μ_B, and the interparticle distance is in the nm range, DDI energy is of the order of hundredths of Kelvin, thus playing a key role in the magnetic ordering of nanoparticle-based materials.

The interfacial exchange anisotropy is an additional source of anisotropy and can be exploited to modify and improve the magnetic properties of a material. For example the exchange anisotropy between an FM and an AFM material, is manifested by the shift of the hysteresis loop along the magnetic field axis directions (exchange bias, EB). EB was first observed by Meiklejohn and Bean in oxidized Co nanoparticles exhibiting hysteresis loop displaced along the field axis after cooling the sample from room temperature under an applied magnetic field [42-45]. They attributed this phenomenon to the exchange interaction at the interface between the FM Co core and the AFM CoO shell. This interpretation was generally accepted as a phenomenological explanation of EB but many models have been proposed to explain it from a microscopic point of view and many controversial results have been presented in the literature [46,47].

In a simple and intuitive picture, the EB phenomenon can be described in terms of an alignment of the AFM spins at the FM–AFM interface parallel to the FM spins occurring during the field cooling procedure. The coupling between the AFM and FM spins at the interface exerts an additional torque on the FM spins, which the external field has to overcome. If a magnetic field is applied at a temperature T so that $T_N<T<T_C$ and the field is large enough, all the spins in the FM align parallel to H, that is, the FM is saturated. Meanwhile, the spins in the AFM remain randomly oriented (paramagnetic state), since $T>T_N$. When the FM–AFM couple is cooled through T_N, the magnetic order in the AFM is set up. During the cooling the spins at the FM–AFM interface interact with each other by exchange coupling; the first layer of spins in the AFM tend to align parallel to the spins in the FM (assuming a FM interaction at the interface), while the adjacent layers in the AFM orient antiparallel to each other, so as to give a zero net magnetization in the AFM. The intuitive spin configuration, for a FM– AFM couple, is shown schematically in figure 6 for different regions of a hysteresis loop. After the field cooling process, the spins in both the FM and the AFM lie parallel to each other at the interface (Figure 6, step 2). When the magnetic field is reversed, the spins in the FM start to rotate. However, if the AFM anisotropy, K_{AFM}, is large enough, as it is often the case, the spins in the AFM will remain fixed. Consequently, due to the interface coupling, they will exert a microscopic torque on the spins in the FM, trying to keep them in their original position (Figure 6, step 3). Thus, the magnetic field required to completely reverse the magnetization in the FM is higher than the uncoupled case, that is, a higher magnetic field is required to overcome the microscopic torque exerted by the spins in the AFM. As a result, the coercive field in the negative field branch increases (figure 6, step 4). Conversely, when the magnetic field is reversed back to positive values, the rotation of spins in the FM is easier than in the uncoupled FM, since the interaction with the spins in the AFM now favours the magnetization reversal, that is, the microscopic torque exerted by the AFM is in the same direction as the applied magnetic field (figure 6, step 5). Therefore, the coercive field in the positive field branch is reduced. The net effect is a shift of the hysteresis loop alongthe magnetic field axis, usually measured by the so-called EB field $H_{EB} = -(H_{c-right} + H_{c-left})$. In other words, the spins in the coupled FM have only one stable configuration (i.e. unidirectional anisotropy).

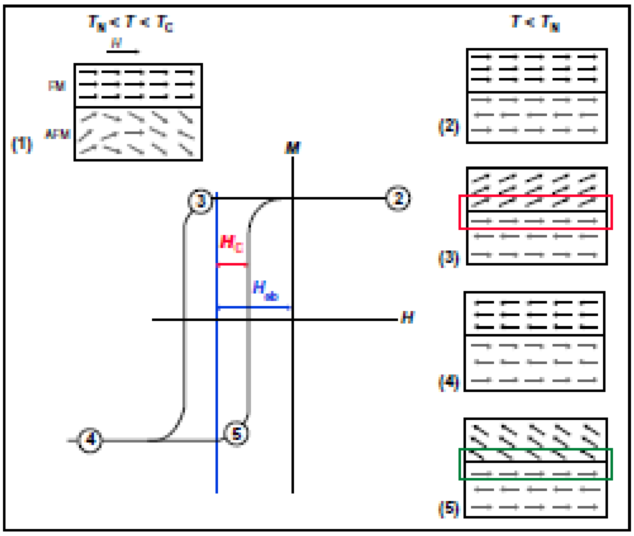

Figure 6 An intuitive picture of the spin configuration of an FM–AFM couple (AFM having a large anisotropy) at different stages of an exchange biased hysteresis loop.

Magnetic interactions in general modify the energy barrier coming from the anisotropy contributions of each particle and, in the limit of strong interactions, their effects become dominant and individual energy barriers can no longer be considered, only the total energy of the assembly being a relevant quantity. In this limit, the relaxation is governed by the evolution of the system through an energy landscape with a complex hierachy of local minima.

The first attempt to introduce interactions in the Néel-Brown model was made by Shtrikmann and Wohlfarth [40] that, by means of a mean field approximation, predicted a Vogel-Fulcher law for the relaxation time in the weak interaction limit, of the form:

$$\tau = \tau_0 \exp\left(\frac{\Delta E_a}{k_B(T_B - T_0)}\right)$$

(9)

Where T_B is the blocking temperature and T_0 is an effective temperature which accounts for the interaction effects.

A more general approach was developed by Dormann *et al.* [48]. This model correctly reproduces the variation of T_B deduced from ac susceptibility and Mossbauer spectroscopy as a function of the observation time window of the experiment τ_m, at least in a range of time covering eight decades. The increase of T_B with the strength of dipolar interactions has been predicted by this model and also experimentally confirmed [49-52]

In a third model proposed by Morup and Tronc [53] for the weak interaction limit, the opposite dependence of T_B with the strength of the interaction is predicted. This behaviour was experimentally confirmed in γ-Fe_2O_3 particles [53]. In order to un-entangle the apparent contraddiction, Morup [54] suggested that two magnetic regimes, governed by opposite dependence of T_B occur in interacting particles. At high temperature and/or for weak interactions, T_B signals one set of blocked state and decrease as the interactions increase. In contrast, at high temperature and/or for strong interactions, a transition occurs from SPM state to a collective state which shows most of the features of typical glassy behaviour. In this case T_B is associated with a freezing process and it increases with the interactions.

II.iv Surface effects

Surface effects dominate the magnetic properties of the smallest particles since decreasing of the particle size, the ratio of the surface spins to the total number of spins increases, e.g. in a particle of diameter ~3nm, about 70% of atoms lie on the surface, which is structurally and magnetically disordered. Consequently, the picture of a single domain nanoparticle where all the spins are pointing into the same direction leading to coherent relaxation process, is no longer valid. Defects, missing bonds and the decrease of the average coordination number determine a weakening of the exchange interaction between surface atoms. Moreover, the symmetry breaking at the surface results in a surface anisotropy (SA) which can represent the dominant contribution to the total anisotropy for small enough particles. In most cases SA is strong enough to compete with the exchange energy that favors full alignment of particle spins. Actually it is expected that the magnetization vector will point along the bulk axis in the core of the particle, and it will then gradually turn into a different direction when it approaches the surface. The magnetic disorder at the surface would induce a reduction of the saturation magnetization and facilitates the thermal demagnetization of the particle in zero field. Morover, interactions between the surface and the core spin structure (it can be seen as a kind of interface exchange anisotropy) should also be taken into account. The two previously named contributions to the surface interaction can be in competition making it difficult to model the particle magnetic behaviour and experimentally separate their contribution.

III. Hollow maghemite nanoparticle

Even though the dynamics in iron oxide MNPs have been investigated over the past 20 years [54-61], its complete knowledge is still unreached, in particular when surface effects are included. The effect of the spin disorder near the surface in full iron oxide MNPs is indeed not easy to observe experimentally, due to the low number of surface spins compared to the core ones.

Moreover, even if an excellent control of the crystallinity and the size distribution has recently been achieved [62], different synthesis procedures strongly affect the properties and the thickness of the surface spins corona [63]. In order to enhance the chance to observe the dynamics of surface spins the idea of increasing the surface to volume ratio by the synthesis of “hollow” MNPs was recently proposed [64,65]. Despite the growing interest on this kind of geometry, which could lead to great advantages in biomedical and magnetic memories application [67], only few works are focused on their local magnetic dynamics [68-72].

Recent progress has shown that hollow iron oxide nanoparticles can be readily synthesized by using the nanoscale Kirkendall effect [67,67]. This effect was initially proposed to describe the formation of voids at the interface of two bulk material due to their different interfusion rate [64,65]. In a nanoparticle system, the Kirkendall effect refers to preferred outward elemental diffusion led into a net material flux across the spherical interface and a consequent formation of a single void at the center. Figure 7 is a sketch of the synthesis of the core-shell-void Fe-Fe_3O_4 and hollow Fe_3O_4 nanoparticles from Fe-Fe_3O_4 nanoparticle seeds.

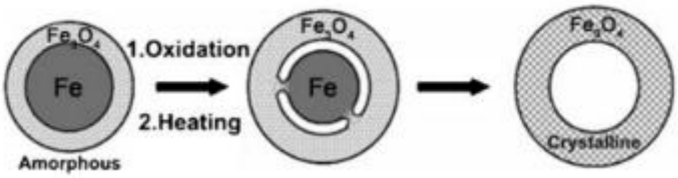

Figure 7 Sketch of the synthesis of core-shell-void Fe-Fe_3O_4 and hollow Fe_3O_4 nanoparticles from Fe- Fe_3O_4 nanoparticles seed [67].

High resolution TEM images (HTREM) of previously sinthesized hollow samples [64,69,69,72] show that the shell is no longer a single crystal but consists of polycrystalline maghemite/magnetite (see figure 8).

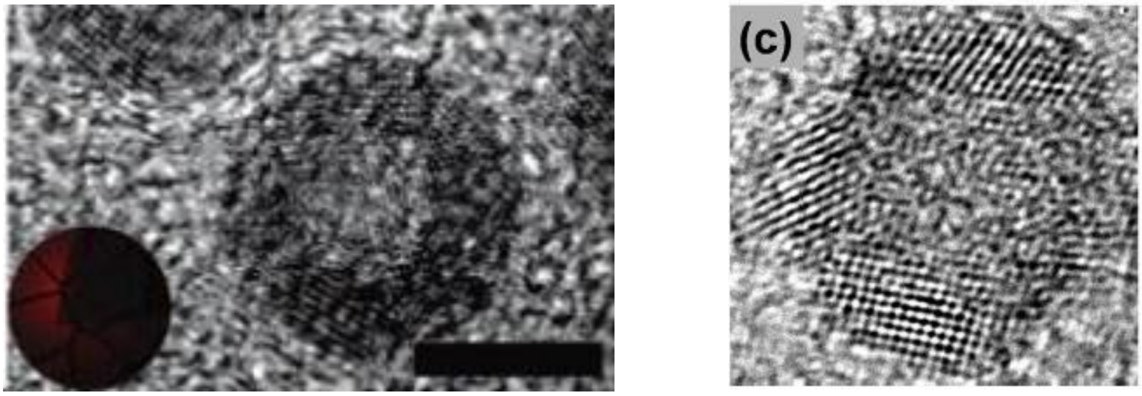

Figure 8 High resolution transmission electron microscopy micrographs of previously synthesized [64] hollow maghemite nanoparticles. Scale bar correspond to 4nm.

A theoretical approach to the hollow geometry and its influence on the spin topology (i.e. number of magnetic domain) was first proposed by D. Goll *et al.* in 2007 [70]. They showed that the hollow geometry incorporates additional parameters for the tuning of the magnetic properties of the nanoparticles. In particular they theoretically determined the phase diagram (see figure 9) of the lowest-energy domain configurations in hollow ferromagnetic nanoparticles as a function of the material, particle size and shell thickness. However while this initial model did not include interface or surface effects, actual hollow nanoparticles are characterized by large surface to bulk ratio. Nevertheless the theory of Goll predicted a critical size which states the upper threshold for a single domain configuration in hollow nanoparticles. As discussed above, hollow nanoparticles are usually polycrystalline structures due to the multiplicity of shell nucleation site. Thus they have multiple crystallographic domains which are randomly orientated and so have differentiated local anisotropy axes. Goll demonstrated that, in contrast to bulk spheres, no homogeneous nucleation process exists in hollow spheres for the magnetization reversal of the single-domain state. Instead, the nucleation takes pla1ce inhomogeneously and starts at the internal poles of the single-domain particle where the demagnetizing field has its largest value. In this sense the inner surface of a hollow particle could play a crucial role in the magnetic behaviour of the whole particle.

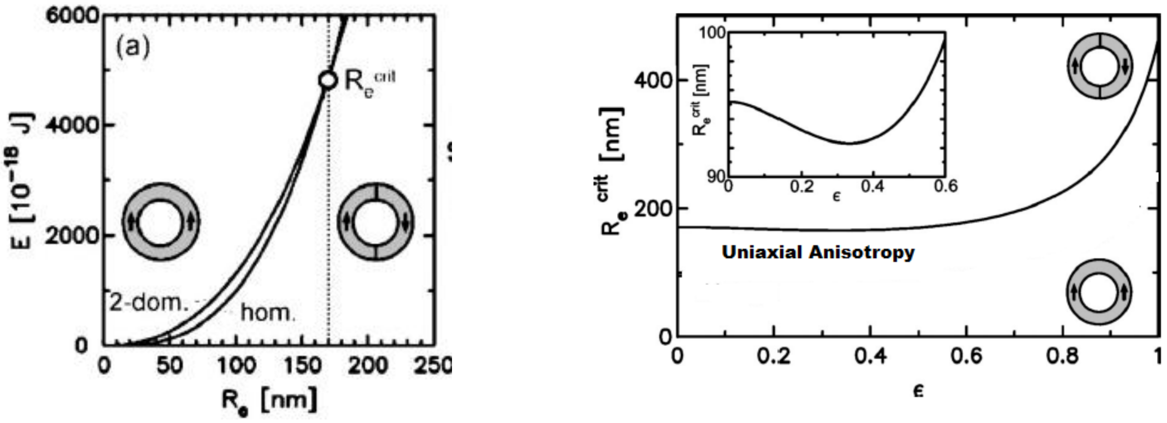

(a) (b)

Figure 9 (a) Comparison of the total energies of different magnetization states as a function of the external particle size R_e for ferromagnetic hollow nanoparticle with uniaxial anisotropy. (b) Phase diagram of the lowest-energy magnetization configuration as a function of the parameter $\epsilon = R_i/R_e$. The inset is a magnification of ${R_e}^{crit}$ from $\epsilon = 0$ to $\epsilon = 0.6$ [Goll].

Short time after Goll's calculation, Cabot *et al.* in 2007 succeded in the synthesis of hollow iron oxide nanoparticle [64] and in 2009 [71] they performed the first Monte Carlo simulations of an individual maghemite nanoshell model. In their model the maghemite ions are represented by classical Heisenberg spins placed on the nodes of the real maghemite structure sublattices, having tetrahedral and octahedral coordinations and interacting accordingly to the hamiltonian:

$$H/k_B = -\sum_{\langle i,j\rangle} J_{ij}\left(\vec{S_i}\cdot\vec{S_j}\right) - \sum_{i} \vec{h}\cdot\vec{S_i} + E_a$$

(10)

The first term is the nearest-neighbor (nn) exchange interaction, the second term is the Zeeman energy with $h = \mu H/k_B$ (H is the magnetic field an μ is the magnetic moment of the magnetic ion) and the third term corresponds to the magnetocrystalline anisotropy energy. In this last term they distinguished surface spins (with anisotropy constant k_S), having reduced coordination with respect to the bulk from core spins having full coordination and an anisotropy constant k_C.

Moreover they considered a Néel tipe of anisotropy for the surface spins and a uniaxial anisotropy along the direction $\hat{n_i}$ for the core spins. The corresponding energy can be expressed as

$$E_a = k_S \sum_{i\in S}\sum_{j\in nn}\left(\vec{S_i}\cdot\hat{r_{ij}}\right)^2 - k_S \sum_{i\in C}\left(\vec{S_i}\cdot\hat{n_i}\right)^2$$

Where r_{ij} is a unit vector joining spin *i* with its nearest neighbors j and n_i are the anisotropy axes of each crystallite. It is worth to notice that k_S and k_C represent the anisotropy constant normalized to the number of spins (i.e. $k = K/N$, where N is the number of spins associated to the anisotropy constant K).

The value of K_C was taken as the value of bulk maghemite (4.7 x 10^4 erg/cm^3) and they evaluate K_S=0.1-1 erg/cm^3 by considering the effective anisotropy obtained from the magnetization measurements as: $K_{eff} = K_C + \frac{S}{V}K_S$ (S and V being the particle surface and volume respectively). When expressed in unit of K/spin, as used in the simulations, these value corresponds to

$$k_C \geq 0.01\, K/spin$$

$$k_S \geq 1 - 5\, K/spin$$

It is important to notice that the simulation of Cabot were able to reproduce the peculiar behaviour that was found for the experimental hysteresis curves of hollow samples. In paticular their hysteresis present a left shift toward negative values of field (i.e exchange bias effect) and a vertical shift toward the positive axis of magnetization [68,69,71].

Figure 10 displays a snapshot of the low temperature magnetic configuration for $k_S = 30K$ attained after cooling the sample from a disordered high-temperature phase in zero applied field.

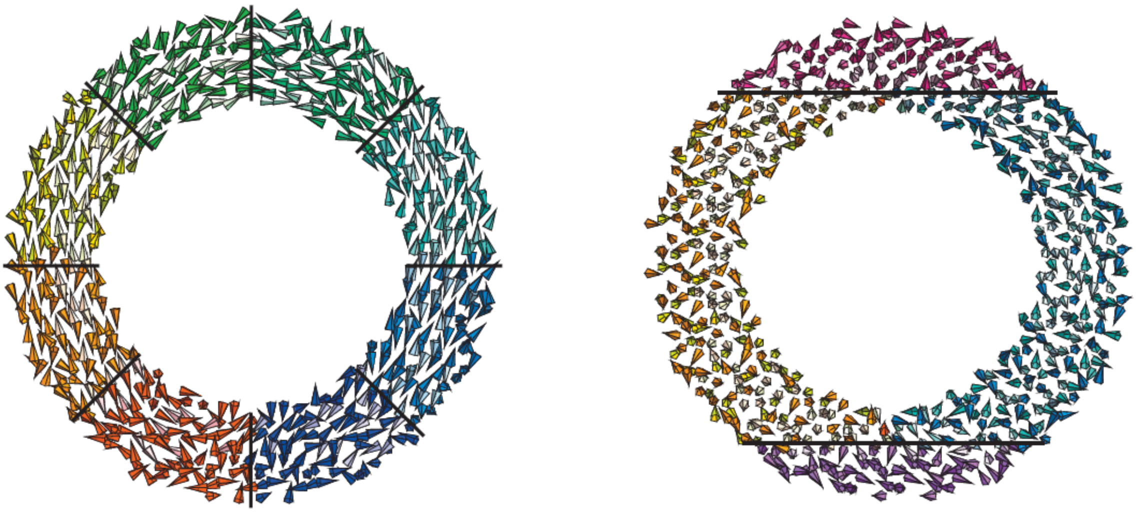

Figure 10 Low temperature snapshots of the magnetic configuration of a hollow particle with external radius R=4.88 a (where a is the cell parameter of maghemite), shell thickness S_T=1.92 a and k_S=30K, obtained from the Monte Carlo simulation of Cabot *et al.* [71]. Left (right) panel shows a cut through a diametric plane parallel to Z (XY) axis. The spin belonging to different crystallites have been distinguished with different colors, with the core spins (those with bulk coordination) colored lighter.

Inspection of the displayed configuration of figure 10 shows that core spins tend to order ferrimagnetically along the local easy axis of each crystallite, while most of the surface spins remain in a quasidisordered state induced by the competition between the surface anisotropy and the antiferromagnetic (AFM) exchange interactions. The exchange interaction among the individual crystallites forming the shell is not sufficient to align all the magnetic moments of each crystallite in the same direction for the entire shell. That is, the magnetic behaviour of hollow maghemite nanoparticles at low temperature is dominated by the crystallographic anisotropy of the individual domains forming the shell.

At high enough temperature, thermal agitation permits spins of the different crystallite cores to detach from the crystallographic anisotropy axis and to follow the applied magnetic field and the weaker intercrystal interactions. In this way, in the superparamegnetic regime, the spins of the crystallites core within the shell tend to align coherently throughout the entire particle.

In a more recent study performed by Kurshid *et al.* in 2014 [73], it was found that for $d < 10$ nm magnetic relaxation in a hollow particle ensemble is best described by a non-interacting particle model, as the dominant role of disordered surface spins and the severely reduced particle magnetization render the influence of dipolar interactions negligible in determining the low-temperature magnetic behavior. They also demonstrated that when the external size of the hollow particles is increased to 15 nm, the portion of spins having bulk coordination is sufficient (and thus bulk-like magnetic moment) to give rise to collective processes via dipole-dipole interactions, and relaxation could be described by the Vogel-Fulcher model for interacting particles.

In the same work, the role of surface spins in the static and dynamic magnetic responses of an ensemble of γ -Fe_2O_3 hollow particles were explored. The results of experimental observations and Monte Carlo simulations demonstrate that the freezing of disordered spins at the inner and outer surfaces leads to the development of spin-glass-like behaviors including memory, remanence, and aging effects, as well as an exchange bias phenomenon in which surface spins play the role of an irreversible magnetic phase.

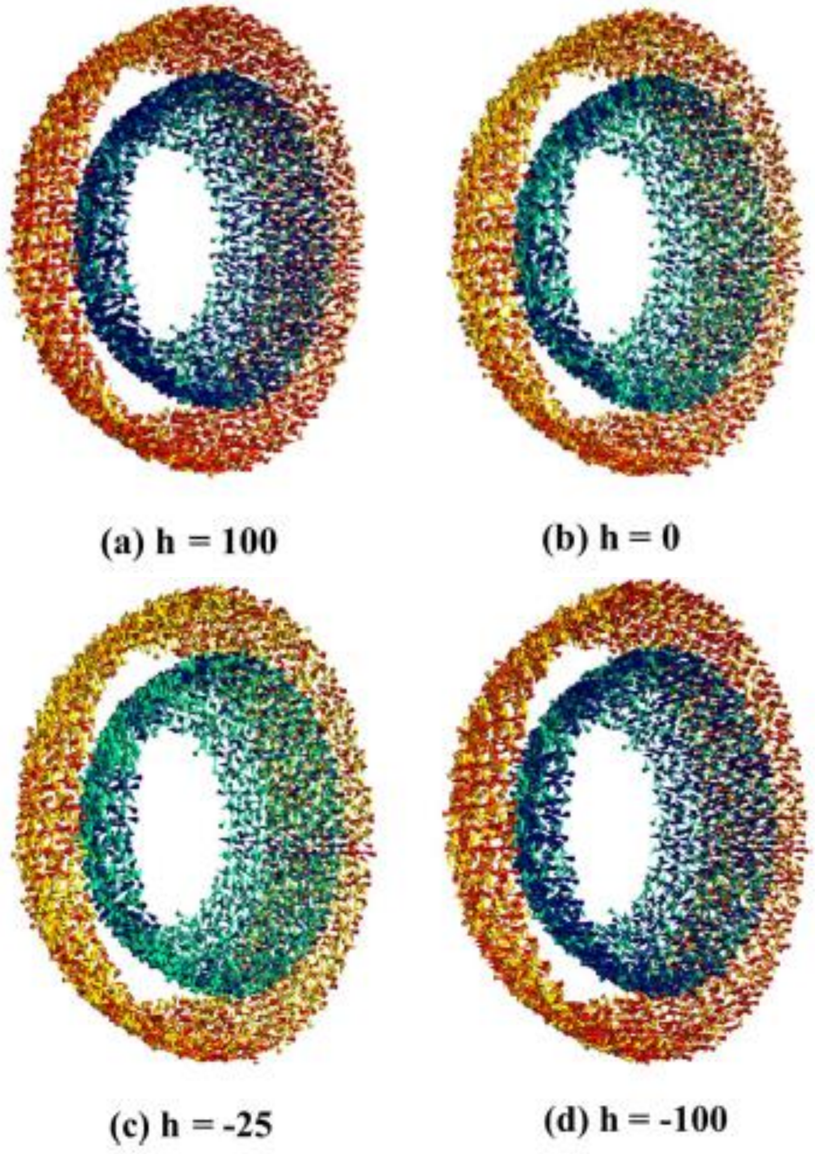

Figure 11 Snapshot of the outer and inner surface spin configurations subject to varying magnetic fields h (see equation 10) simulated by Kurshid et al. [73] (a) h=100 (the maximum positive applied field), (b) h=0 (remanence at the upper brunch), (c) h=-25 (near the negative cohercive field), (d) h=-100 (the maximum negative applied field). Spins have been colored with a gradient from dark-red/dark-blue (outer/inner surface) for spin along the field direction to yellow/green (outer/inner surface) for spins transverse to the field direction. Only a slice of the spin configurations of a hollow nanoparticle close to the central plane and perpendicular to the field direction is shown.

Montecarlo simulations were performed and confirms strongly disordered surface layers (see figure11) in the hollow particle morphology with complex energy landscapes. The so simulated hysteresis loops show that inner surface spins are more easly magnetized than those located at the outer surface and produce an hysteresis loop with a small vertical shift indicating that dynamic behaviours are not equivalent at the two surfaces. This last evidence could be linked to the theoretical Goll’s calculation which predicts that the nucleation in hollow nanoparticles starts at the internal poles of the single-domain particle where the demagnetizing field has its largest value.

CHAPTER 2:

STATIC MAGNETIC PROPERTIES

Overview

In this chapter the morphological and the static magnetic properties of hollow NPs are investigated, moreover a brief discussion of the synthesis procedure is proposed. The morphological parameter such as the eternal diameter, the internal diameter, the volume occupied by the disordered surface spins were related to previousy reported Mossbauer data on the same samples. The static magnetization of the hollow samples as a function of the external magnetic field and as a function of temperature were compared to the data on the full samples and analysed according to the presence of an extra contribution. Finally, the informations extracted from the analysis of the magnetic characterization such as the saturation magnetization (M_s) and the blocking temperature (T_b) were compared to the morphological parameter and confirmed that the percentage of surface spins in hollow nanoparticles is in direct correspondence with the mean canting angle in the whole particle.

I. Investigated Samples

In this paragraph we present five hollow investigated samples and two full samples which will be considered as reference of the full topology.
Full Iron oxide MNPs were prepared and characterized in the framework of a collaboration with dott. M. Casula (see acknowledgments) according to surfactant-mediated colloidal routes in high boiling organic solvents under nitrogen atmosphere [74-77], using Schlenk line procedures. The preparation route, which was adapted from [75] relies on two steps including i) the synthesis of the iron oxide precursor and ii) its thermal decomposition in a hot solution containing surfactants [76,77]. For all synthesis, as iron oxide precursor, an iron (III) oleate complex was used.
Hollow maghemite nanopartcles were obtained following a previously reported procedure based on the Kirkendall effect [64]. The samples were prepared and characterized in the framework of a collaboration with dott. D. Peddis (see acknowledgments). Briefly, $Fe(Co)_5$ was decomposed in air free conditions at around 220°C in organic solvents. The resulting iron based nanoparticles were oxidized in solution by means of a dry synthetic air flow. Owing to the faster self-diffusion of iron than oxygen ions within iron oxide, the oxidation of 5-15 nm nanoparticles resulted in 7-18 nm hollow iron oxide nanostructures.
The so prepared full and hollow sample are presented in figure 1 which contains the TEM images together with the histograms related to the diameter's distributions. The dimentions of the nanoparticles were calculated from the analysis of more than 300 nanoparticles with the hypothesis of a lognormal distribution for both the external and internal diameters. The presence of an inorganic coating capping the nanoparticles doesn't give any contrast in the TEM images so that the diameters distributions are referred to the inorganic magnetic core.

Even if it is not magnetic, the coating can affect the nanoparticle magnetic behavior. In particular the interaction between molecules and surface atoms leads to a modification of the surface anisotropy. Moreover the coating tunes the interparticle distance which affects the strength of the dipolar interactions between particles, this last having a demagnetizing effect. For these reasons and to favor the sistematicity of the study, all the NPs have been capped with oleic acid.

Since the oleic acid has a thickness around 2nm for all the investigated nanoparticles, the hollow (H) samples were named as H_D_i/D_e where D_i and D_e are respectively the internal and the external diameter of the inorganic part. For the same reason the full (F) particles were named as F_D where D is the inorganic core's diameter.

According to the dimensions extracted from the TEM images, the following samples have been investigated:

- ***HOLLOW:*** H_2.8/7.3, H_6/11, H_5.3/13, H_8/15, H_10/16
- ***FULL:*** F_5, F_8.5
-

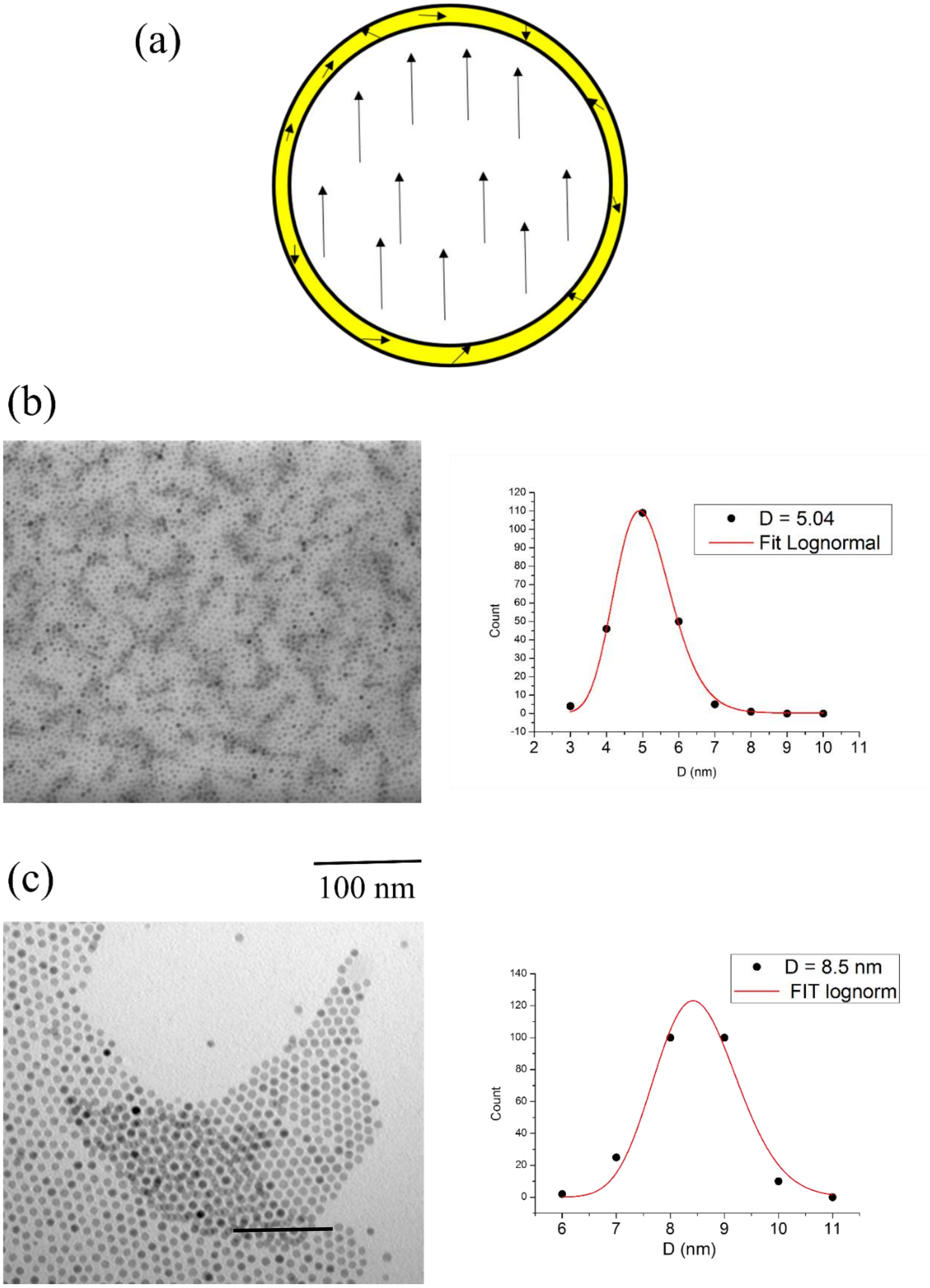

Figure 1 TEM images and size distribution of the full nanoparticle samples: (a) Sketch of the full spin topology. The thin surface spin layer is depicted in yellow, (b) F_5 sample, (c) F_8.5 sample. The scale length corresponds to 100nm.

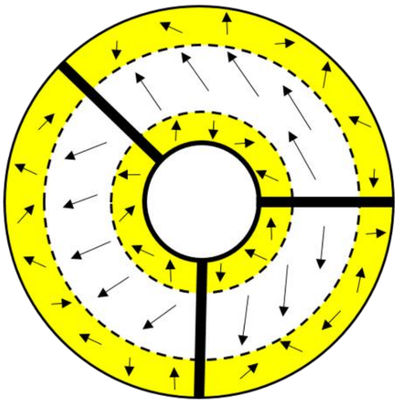

(a)

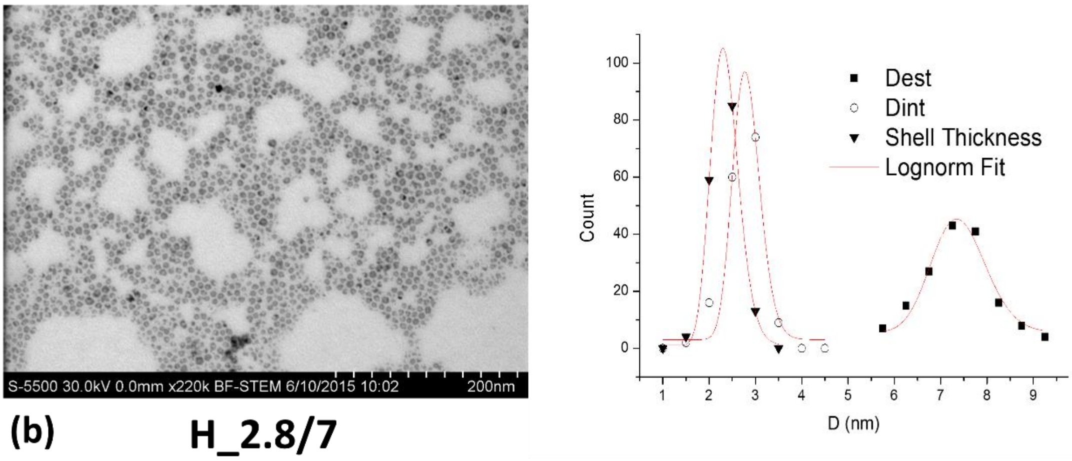

(b) H_2.8/7

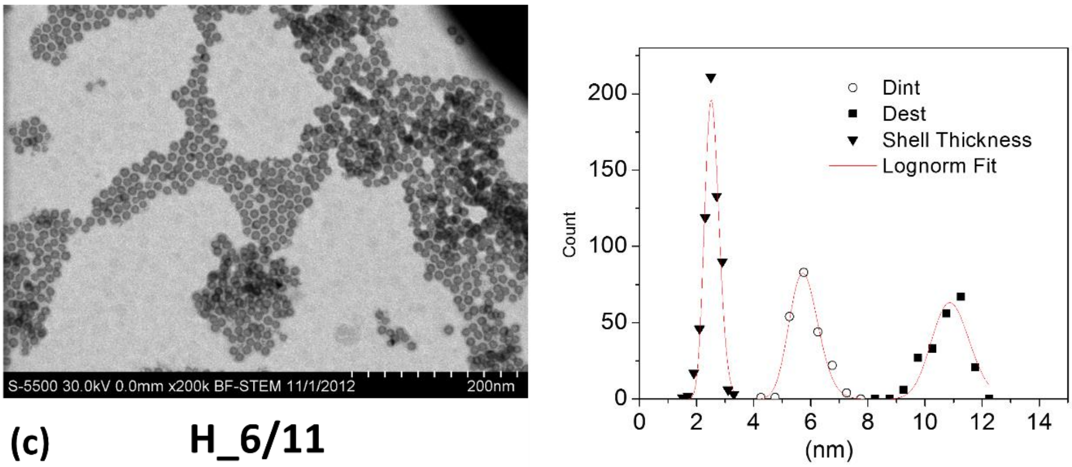

(c) H_6/11

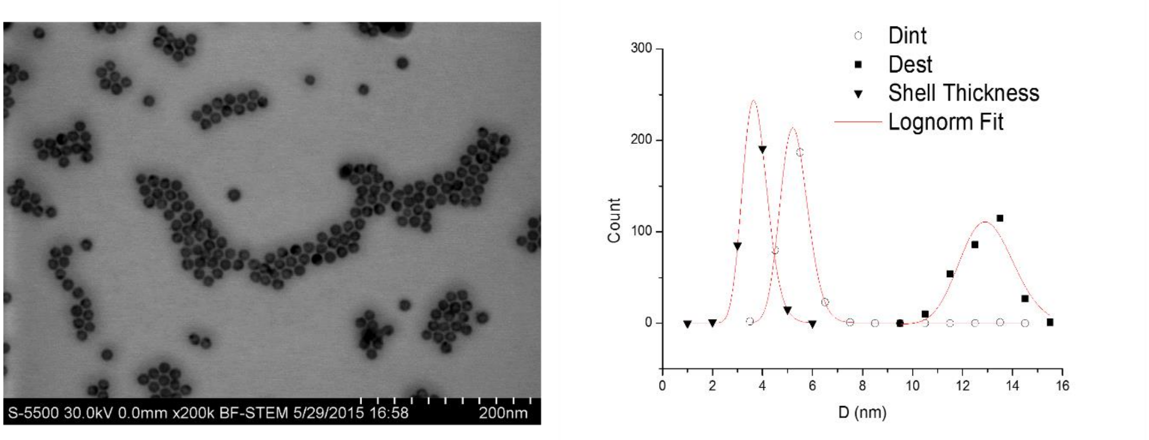

(d) **H_5.4/13**

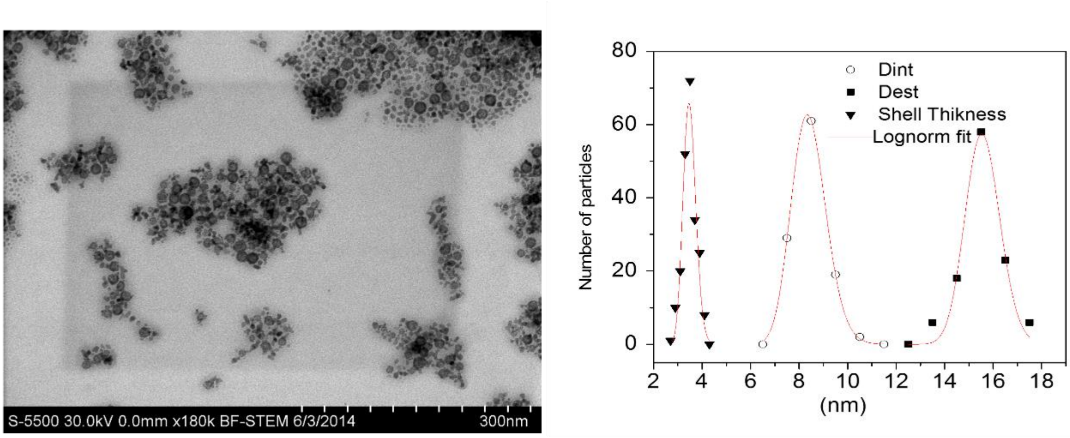

(e) **H_8/15**

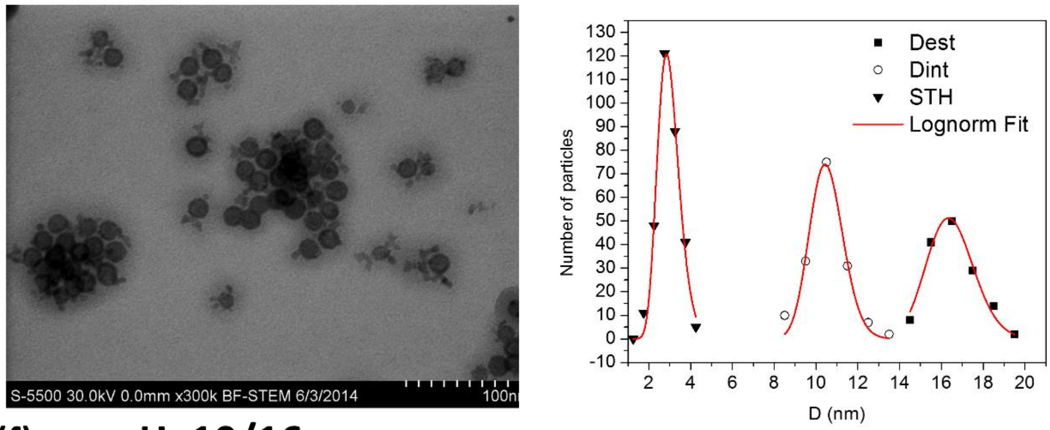

(f) **H_10/16**

Figure 2 TEM images and size distributions of the hollow nanoparticle samples: (a) Sketch of the hollow spin topology: the inner and outer disordered surface layers are depicted in yellow. The surface is much thicker with respect to the one of the full nanoparticles. The crystallites with different directions of anisotropy axes are identify by bold lines. Different sample: (b) H_2.8/7.4, (c) H_6/11, (d) H_5.3/13, (e) H_8/15 (f) H_10/16. The inset shows the frequency of the counted particles.

In table 1 the morphological parameters of the H samples extracted from the TEM image, such as the internal and external diameter, the inner and outer geometric surface and the shell thickness (i.e. D_i, D_o, S_i, S_o and ST) are listed. In the same table the mean spin canting angles (the canting is considered with respect to the anisotropy axes) given from a previous Mössbauer analysis on the same samples are also listed (PhD thesis of Fatima Sayed). From the values of the canting angles it was possible to estimate the inner and outer surface thickness (TH_i and TH_o respectively) and thus the volume of the "surfaces" (V_{si} , V_{so} and $V_s=V_{si}+V_{so}$).

Due to the complexity of the hollow topology (see chapter 1) the choice of a meaningful comparison parameter (i.e. the magnetic volume that is commonly used to compare full particles) is not trivial. To access this difficult task we listed in table 2 five categories (trend 1 to 5) in which is possible to gather the morphological parameters: in each of the 5 trend-categories, are listed parameters having the same qualitative behaviour of the color-highligthed experimental raw quantity (from top to the bottom: D_i, V, D_i/D_o, canting angle, shell thickness)

The need to complement the TEM morphological data with the Mossbauer analysis, even if this last it is not part of this thesis, is due to low knowledge we have of these system also in the current literature. In particular we remark the lack of existing models able to describe the complex spin dynamics in the hollow samples.

	Moss	*TEM*	*Moss*		*TEM*	*Moss*															
sample	**Cant_Ang (°)**	**Di (nm)**	**THi (nm)**	**Vsi (nm^3)**	**Do (nm)**	**Tho (nm)**	**Vso (nm^3)**	**ST (nm)**	**Di/Do**	**Sin (nm^2)**	**Sout (nm^2)**	**Sin/Sout**	**THi/THo**	**Vsi/Vso**	**Vs (nm^3)**	**S (nm^2)**	**V (nm^3)**	**S/V (nm^{-1})**	**Vs/V**	**Vc (nm^3)**	**Vs/Vc**
F_5	6	0	0	0	5	0,01	0,8	5	0	0	79	0	0	0	0,8	79	65	1,20	0,012	64	0,013
F_8.5	n.a.	0	0	0	8,5	n.a.	n.a.	8,5	0	0	227	0	n.a.	n.a.	n.a.	227	321	0,71	n.a.	n.a.	n.a.
H_2.8/7.4	36	2,8	0,24	7	7,39	0,64	92	2,29	0,38	25	171	0,14	0,37	0,08	98,8	196	200	0,98	0,49	101	0,98
H_6/11	45	5,9	0,8	116	11,1	1,4	419	2,57	0,54	112	389	0,29	0,57	0,28	534,6	501	610	0,82	0,88	76	7,06
H_5.3/13	30	5,3	0,33	32	12,9	0,8	368	3,82	0,41	87	523	0,17	0,41	0,09	400,7	609	1048	0,58	0,38	647	0,62
H_8/15	42	8,1	0,9	230	15,1	1,7	964	3,5	0,54	206	716	0,29	0,53	0,24	1193,3	922	1524	0,6	0,78	331	3,61
H_10/16	53	10,1	1,6	692	15,82	2,5	1409	2,86	0,64	320	786	0,41	0,64	0,49	2101	1106	1534	0,72	1,37	-568	-3,7

Table 1 List of the morphological parameters extracted from TEM (internal and external diameter D_i and D_o) analysis and from Mossbauer analysis (canting angles, inner and outer surface thikness TH_i and TH_o). The last columns contains papameters calculated from the previous ones. From leftt: V_{si} and V_{so} are the inner and outer volume occupied from the canted disordered spins we ascribed to the surface contribution; ST is the shell thickness; S_{in} and S_{out} are the inner and outer geometrical surface; V_s is the total volume associated ti the surface; V_c is the volume associated to the core ordered spins; S and V are the nanoparticles geometrical total surface and volume.

TREND 1	D_i (nm)	TH_i (nm)	V_{si} (nm^3)	TH_o (nm)	V_{so} (nm^3)	S_i (nm)	V_s (nm^3)
H_2.8/7.3	2,8	0,2	7,0	0,6	91,8	25,0	98,8
H_5.3/13	5,3	0,3	32,4	0,8	368,3	87,0	400,7
H_6/11	5,9	0,8	116,0	1,4	418,6	112,0	534,6
H_8/15	8,1	0,9	229,7	1,7	963,6	206,0	1193,3
H_10/16	10,1	1,6	692,0	2,5	1409,0	320,0	2101,0

TREND 2	D_o (nm)	S_o (nm^2)	S (nm^2)	V (nm^3)
H_2.8/7.3	7,4	171,5	196,1	200,1
H_6/11	11,1	388,6	500,5	610,0
H_5.3/13	12,9	522,5	609,4	1047,8
H_8/15	15,1	716,0	922,0	1524,0
H_10/16	15,8	785,9	1106,2	1533,6

TREND 3	D_i/D_o	S_i/S_o	TH_i/TH_o	V_{Si}/V_{So}
H_2.8/7.3	0,38	0,14	0,38	0,08
H_5.3/13	0,41	0,17	0,41	0,09
H_8/15	0,54	0,29	0,53	0,24
H_6/11	0,54	0,29	0,57	0,28
H_10/16	0,64	0,41	0,64	0,49

TREND 4	V_S/V	V_S/V_{core}	Cant Ang (°)
H_5.3/13	0,38	0,62	30
H_2.8/7.3	0,49	0,98	36
H_8/15	0,78	3,61	42
H_6/11	0,88	7,06	45
H_10/16	1,37	-3,70	53

TREND 5	SHELL TH (nm)	S/V (nm^{-1})
H_2.8/7.3	2,29	0,98
H_6/11	2,57	0,82
H_10/16	2,86	0,72
H_8/15	3,5	0,6
H_5.3/13	3,82	0,58

Table 2 The 5 different trend followed by the 5 sub-groups of main morphological parameters associated to the investigated nanoparticles.

A linear dependence of the mean canting angle with the ratio between the volume of the surface and the total magnetic volume was found. Having a lower coordination number, surface spins are in a disordered configuration with respect to the ordered ferrimagnetic core spins and, in this sense, the more the surface extends in the particle, the higher would be the associated spin disorder (i.e. canting spin angle with respect to the anisotropy axes).

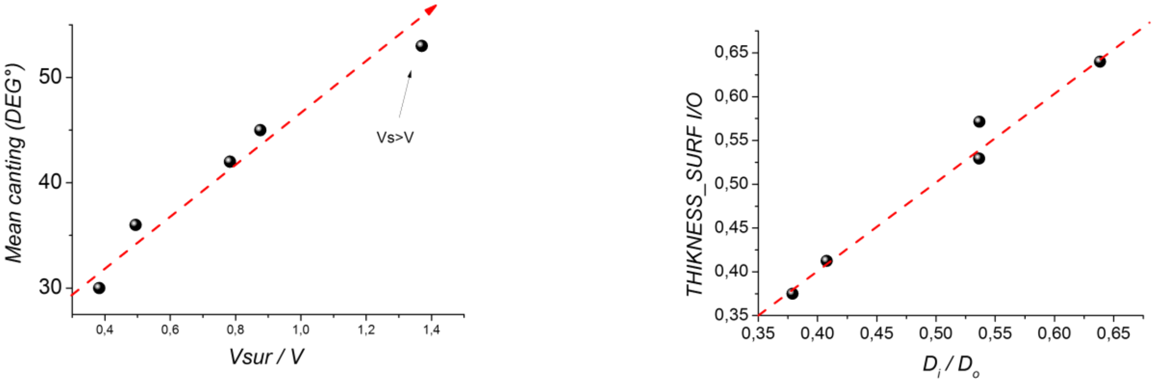

Figure 3 (a) Mean canting angle vs the ratio between the volume of the surface and the total magnetic volume. (b) Inner to outer surface thickness ratio calculated from Mossbauer vs inner to outer diameter ratio calculated from TEM.

It is interesting to notice that the outer diameter D_o and the outer surface S_o are not proportional to the outer thikness TH_o, they rather follow the trend of the total surface S and volume V. Moreover the linear dependence (Figure 3) of the inner to outer surface thickness ratio (TH_i/TH_o) from the inner to outer diameter ratio (D_i/D_o) is a non trivial evidence of the link between the number of disordered spins and the geometrical dimensions on the nanoparticle.

Having in mind the table 2, from now on we will present the experimental data as a function of the representative parameters for each trend; in this sense all the quantities belonging to the same trend are expected to follow the same behaviour.

II. Experimental Data

A static magnetic characterization was performed by means of a superconducting quantum interference device (SQUID) with a superconducting magnet (H_{max} = 5.5 T) in the temperature range 2-300K. To avoid any displacement of the nanoparticles during the measurements, the samples, in the form of powders, were immobilized in an epoxy resin. We studied the dependence of the total magnetization from the static applied magnetic field and from the temperature of the system. The experimental data are presented for full and hollow NPs separately.

In figure 4 and 5 the magnetization of full and hollow samples as a function of the external static field are reported. The measurements were performed at two different temperatures where the spins are expected to be blocked (T=5K) or unblocked (T=300K). A coercive field is observed at T=5K for all samples which implies that the available thermal energy is not enough to overcome the anisotropy barrier and the system is in a blocked ferrimagnetic state. On the other hand no coercivity is observed at T=300K, so that it can be assumed that all samples are in an unblocked superparamagnetic state.

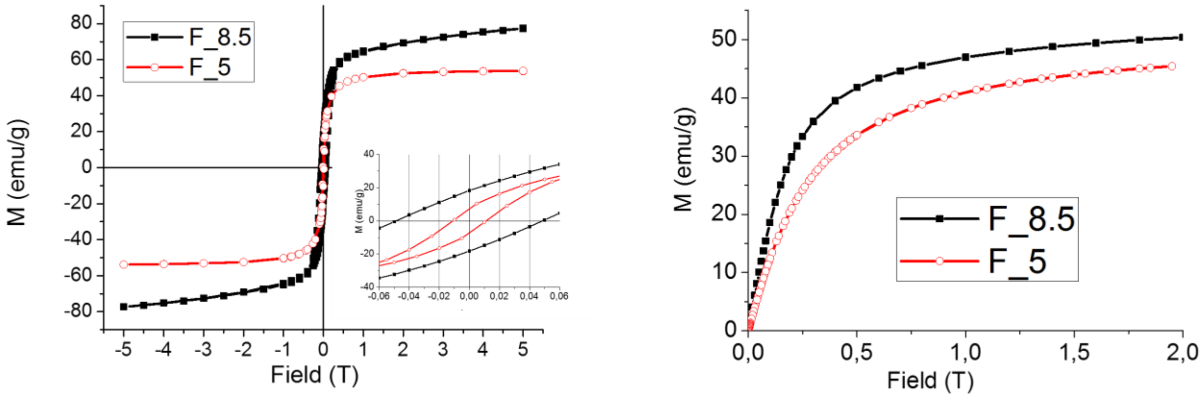

Figure 4 Magnetization as a function of magnetic field for the full samples at (a) T=5K and (b) T=300K. The inset of figure (a) shows a zoom on the coercive field at low temperature.

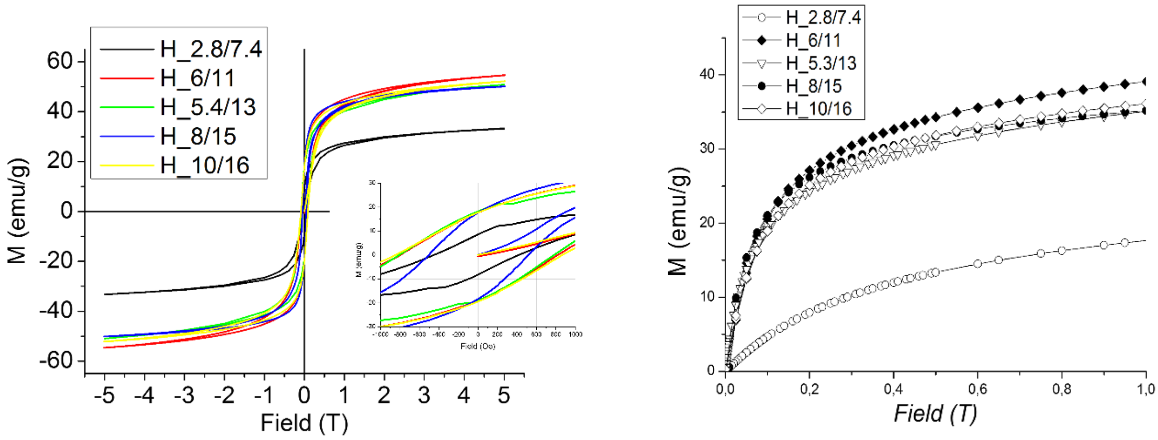

Figure 5 Magnetization as a function of magnetic field for the hollow samples at (a) T=5K and (b) T=300K. The inset of figure (a) show a zoom on the cohercive field at low temperature.

The magnetization as a function of temperature was measured in the presence of a static magnetic field H=25Oe. Figure 6 shows measurements of the zero field cooled (ZFC) and field cooled (FC) magnetization, and the thermoremanent (TRM) and isothermal (IRM) remanence for sample H_8/15. The ZFC magnetization and the IRM were measured as follows: the sample was cooled in zero field down to a temperature T=2K; a magnetizing field H=25Oe was then applied for 100s and the ZFC magnetization was measured; the IRM was measured 100s after resetting the applied field to zero. The FC magnetization M_{FC} and TRM were measured as follows: the sample was cooled in the presence of a field H_{cool}=25Oe to a temperature T=2K and the FC magnetization M_{FC} was measured; the TRM was measured 100s after resetting the cooling field to zero.

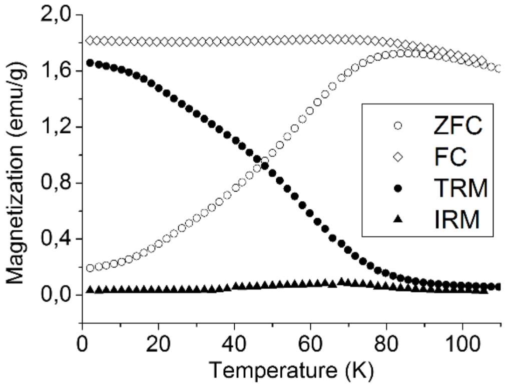

Figure 6 Temperature variation or the ZFC, FC, TRM and IRM magnetization components.

Since IRM~0 for all sample and the TRM~(FC-ZFC) (see figure 6 and paragraph 2.III for the theoretical explanation) for all the measured samples, only FC and ZFC magnetization curves are reported in figure 7. In order to allow a comparison, all the curves are normalized with respect to the maximum of the FC.

Even if the next paragraph will be devoted to the data analysis, some preliminary observations can be done in this section:

(i) the temperature T_{max} of the maximum in the ZFC curve (i.e. the temperature at which the number of spins alligned to the external field is maximum) for full NPs increases as expected [79] with the volume of the full nanoparticle; this last evidence is not verified in the ZFC curves of hollow samples .

(ii) all samples except F_5 display an irrevesible temperature T_{irr} (i.e. the temperature at which the FC separates from the ZFC) very different from T_{max} .

(iii) the FC of all samples except H_2.8/7.4 flattens at low temperature so that a non negligible interparticle interactions is suggested [79].

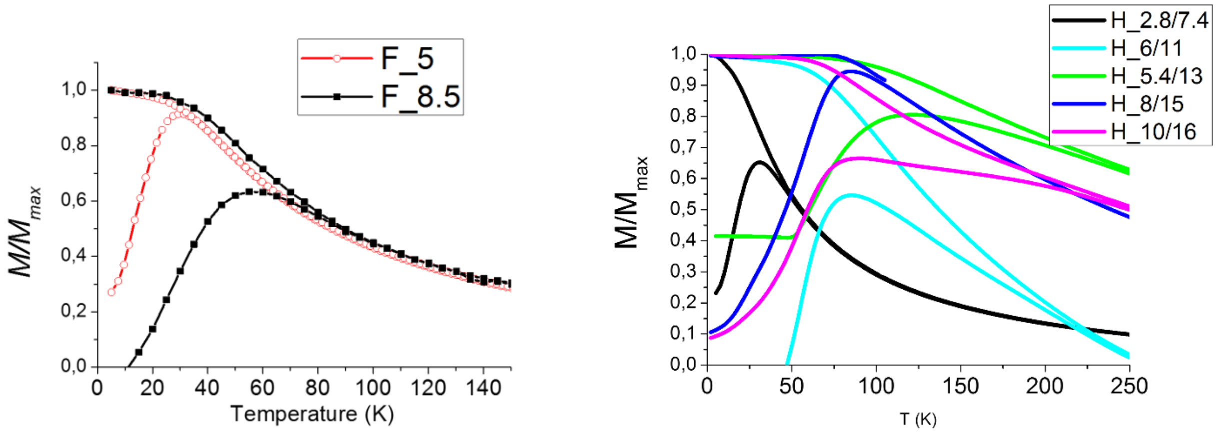

Figure 7 ZFC/FC magnetization curves in a static magnetic field of 5mT for the (a) full samples and (b) hollow samples. The curves have been normalized to the maximum of the FC.

III. Data analysis and Discussion

In this section we present the analysis of the experimental data reported in section 2.II. The theoretical framework and validity of most of the models we used will be briefly discussed before the analysis even if a full description can be found in the cited references.

As the properties of the full topology samples are widely investigated we will use our data on F_5 and F_8.5 to validate the existing state of art. Moreover since the main goal of this thesis is to study the effect of the hollow topology on the spin system behaviour in magnetic nanoparticles, from now on we will consider the full topology as reference and we will focus on the analysis of the hollow samples.

M vs H at low T

As discussed in chapter 1 at low temperature and high field the spins are locked along the easy axes, this last being parallel to the external magnetic field. Figure 4 and 5 show that only sample F_5 is able to reach the saturation (i.e. the magnetization curve flattens) at field lower than 6 T. Indeed the magnezation of all the other samples is still growing indicating that the saturation condition have not been reached by the systems. In these cases the saturation magnetization (M_s) at T=5K was estimated from a fit over the high field data to the empirical formula [81]:

$$M(H) = M_s + \frac{a}{H} + \frac{b}{H^2}$$

(1)

The values of the calculated M_s are reported in table 3 and a plot of the saturation magnetisations of the hollow samples as a function of the morphological parameters such as the shell thickness, volume and inner to outer diameter ratio is shown in figure 8.

First we notice that except for sample H_2.8/7.4 (which is the smallest one) M_s of the hollows is not increasing with the magnetic volume as expected and verified for the full samples (see Table 3 and [79]).

A second hint is given by the lower global magnetization displayed by the hollows with respect to the full ones. In particular, even if F_5 have less than half magnetic volume with respect to H_2.8/7.4, the saturation magnetization is doubled ($M_s^{F\_5}$ = 72 emu/g and $M_s^{H\_2.8/7.4}$ = 36 emu/g). The lowering of M_s (i.e. the order parameter) displayed by the hollows is due to the thick disordered spin layer located in the outer and inner surfaces other than the interface between the different cristallites which are present in the hollow's shells. In particular, having a lower coordination, the surface spins present lower exchange interaction and a lower value of the order parameter. The number of disordered spins is further increased if one considers that the disordered surface layer is much thicker (see TH_o and TH_i of table 1) in the hollows than in the full.

The presence of the surface was found to increase the coercive field H_c and the irreversibility field (the field at which the decreasing and the increasing field loop branches join) of the hollow samples at low temperature. Moreover a left shift of the hysteresis at T=5K (i.e.the exchange bias, H_{EB}) was observed only in the hollow sample thus suggesting the presence of frustrated magnetism as it happens in random anisotropy systems.

The values of H_{EB} are reported in table 3 and are found to decrease with the particle volume. We attribute this behaviour to the polycristalline nature of the maghemite shells and the large number of spin pinned by surface anisotropy effects. At low temperature the spins tend to align parallel to the cristalline anisotropy axes existing in each individual crystallite. Such a tendency leads to the formation of multiple domains within each shell, instead of a single domain with all the spins alligned along a unique axis as predicted by Goll *et al*. [ref] for single crystal nanoshell of diameter below 10-20 nm. It is worth to notice that similar experimental evidence are present in previous works [69,71,78].

Interestingly, except for the smallest sample, the remanent magnetization M_r assumes the same value for all the hollow samples.

Additionally it can be noticed from table 3 that for all the measured samples, the value of M_r/M_s ratio at low T is lower than the value 0.5 predicted for a single particle with uniaxial anisotropy; since the measured samples are in powders both the interactions and the anisotropy topology can in principle contribute to the the low observed value for M_r/M_s.

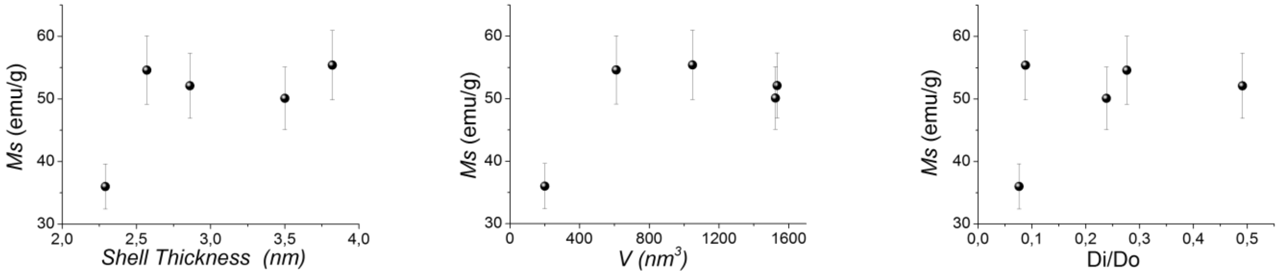

Figure 8 Saturation magnetization per g of sample as a function of the most significative experimental parameters such as the shell thickness (a), magnetic volume (V) and inner to outer diameter (D_i/D_o).

Sample	*V* *(nm³)*	M_s^{5K} *(emu/g)*	M_r^{5K} *(emu/g)*	$\frac{M_r^{5K}}{M_s^{5K}}$	H_C^{5K} *(10⁻⁴T)*	H_{EB}^{5K} *(10⁻⁴T)*
F_5	68	72 ±3	12 ±1	0.2	110 ±2	0 ±2
F_8.5	321	84 ±3	20 ±1	0.2	485 ±2	0 ±2
H_2.8/7.4	200	36 ±2	11 ±1	0.3	453 ±2	20 ±2
H_6/11	610	55 ±3	19 ±1	0.4	806 ±2	12 ±2
H_5.3/13	1047	55 ±6	19 ±1	0.3	803 ±2	18 ±2
H_8/15	1524	50 ±5	19 ±1	0.4	510 ±2	9 ±2
H_10/16	1533	52 ±5	19 ±1	0.3	855 ±2	5 ±2

Table 3 List of the main informations extracted from the hysteresis curves at T=5K. From left: the volume V, the saturation magnetization M_s^{5K}, the remanent magnetization M_r^{5K}, the cohercive field H_C^{5K} and the exhange bias H_{EB}^{5K}.

M vs H at high T

At room temperature (RT) both the surface and core spins have enough thermal energy to move between the minima of the anisotropy energy. In the case of the hollow nanoparticles which present two spin populations (core spins and surface spins), the unblocked state can be seen as the result of a superparamagnetic component due to the core spins and of a paramagnetic component associated to the surface spins, these last having a lower exchange interaction scale length. Instead, the paramagnetic component is not expected to be relevant in the full particles where the percentage of surface spins is negligible. The proof of the previous considerations is found in the experimental M(H) curves which are shown in figure 9 and 10. In particular hollow samples present a linear contribution to the magnetization curves which is less visible in the curves of the full samples. To quantify the linear (paramagnetic) contribution, the M(H) curves at room temperature were fitted by adding a PM contribution to the Langevin function :

$$M(H) = M_s\, L(x) + \chi^{PM}\, H$$

(2)

The results of the fit are listed in table 4, in particular a PM contribution close to zero was found for the full sample while a non null susceptibility was found for the hollow spheres.

The so obtained low values of M_s and large values of χ^{PM} are in line with previous results [71] and can be explained by the large disorder on the hollow nanoparticles surface and on the crystallographic interfaces, which leads to a reduction in the number of spins aligning with the external field. Values of M_s are found to be constant in the experimental error except for the smallest sample H_2.8/7 thus reproducing the behaviour at low temperature (see table 2). The percentage of magnetic volume participating to the Langevin function (V_{SPM}/V in table 4) is much smaller in the hollow samples than in the full ones indicating a lower fraction of spins in the SPM states.

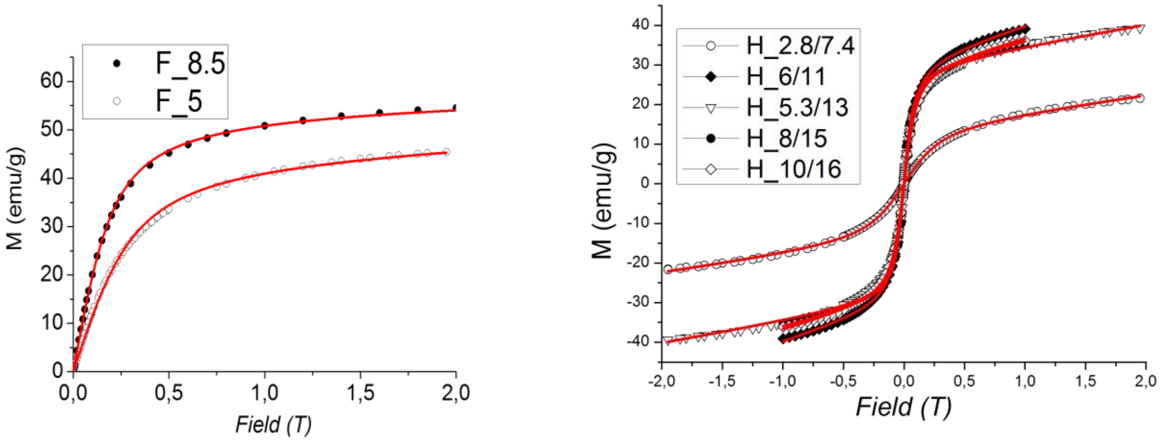

Figure 9 Fitting of the experimental M(H) curves (red lines) at room temperature with equation (2) for (a) H_5.3/13 and 2.8/7.4 taken as reference for the hollow geometry and for (b) F_5. Only for the two hollow samples a non negligible linear contribution was found.

Sample	V_{SPM} (nm^3)	M_s^{300K} (emu/g)	χ^{300K} emu/(gT)	SPM	PM
F_5	64±5	65 ±2	0.2 ±0.2	91%	8%
F_8.5	310±15	78 ±2	0.0 ±0.3	97%	3%
H_2.8/7.4	128 ±50	14 ±2	1.4 ±0.2	79%	21%
H_6/11	400 ±80	34±4	6.1 ±0.2	65%	35%
H_5.3/13	743 ±20	30 ±3	5.2 ±0.3	45%	55%
H_8/15	972 ±30	29 ±2	7.5 ±0.3	63%	37%
H_10/16	675 ±2	30 ±3	8.0 ±0.4	44%	56%

Tabel 4 List of the fit parameter of the M(H) curves recorded at room temperature by means of equation (2). From left: V_{SPM} is the magnetic volume included in the Langevin function which describes the order parameter of the superparamagnetic (SPM) spins; M_s is the saturation magnetization of the SPM contribution, χ is the magnetic susceptibility ascribed to the paramagnetic contribution; SPM and PM are the relative weight of the two contribution evaluated from V_{SPM}/V.

M vs H at intermediate T

Measurements of the magnetization as a function of field at different temperature were performed on sample F_5 and H_2.8/7.4 at temperature down to 30K, the curves are plotted as a function of H/T in figure 10. An H/T scaling of the magnetization is not expected (figure 10a) in superparamagnetic nanoparticles with a large uniaxial anisotropy [82] so that the poor scaling agreement found for H_2.8/7.4 possibly suggests different direction of the anisotropy axes of the cristallites which compose the hollow samples.

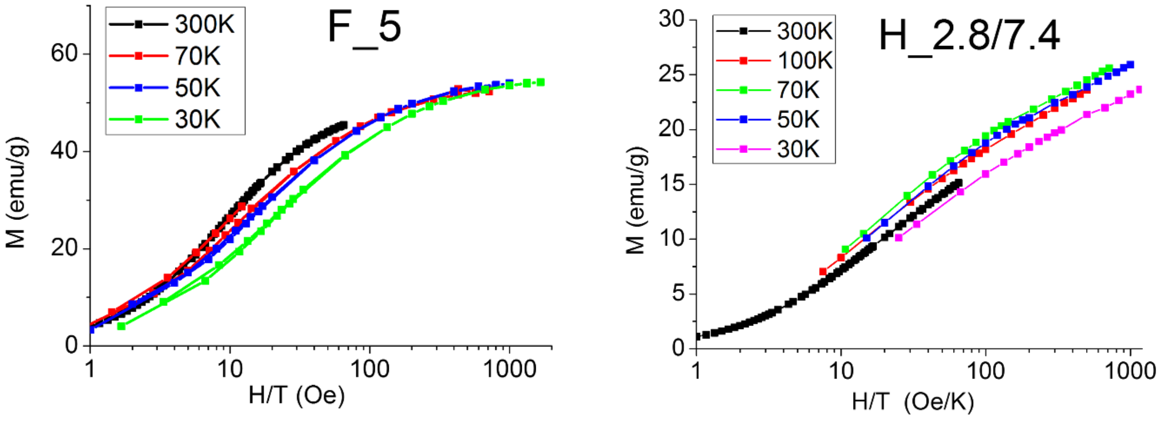

Figure 10 Magnetization (*M*) versus applied field normalized to temperature (*H/T*) data of the F_5 and H_2.8/7 above T_B when the nanoparticles are superparamagnetic.

M vs T data

The magnetization curves as a function of temperature (figure 11) contain information about the energy barrier distributions. Under the ideal condition of non-interacting, monodisperse particles, the peak in the ZFC curve (T^{MAX}_{ZFC}) is often referred as to the mean blocking temperature (T_B). This is associated with the maximum number of nanoparticles unblocking as temperature increases and is found to occur when the thermal energy (k_BT) is comparable to the activation energy (E_A). However, for hollow nanoparticles with strong inter- and intra-particle interactions and finite size distribution, T^{MAX}_{ZFC} may be broadened and shifts to higher values due to enhanced interactions. As a result, the peak (T^{MAX}_{ZFC}) may not accurately represent T_B of the system. For these reason the evaluation of the blocking temperature distributions were performed according to the following description.

For any system the magnetic response can be represented by two components: a reversible one (M_{rev}), which is time indipendent, and an irreversible one (M_{irr}), which is time dependent. Thus the total magnetization is given by:

$$M_{tot}(H,T,t) = M_{rev}(H,T) + M_{irr}(H,T,t)$$

(3)

Where H is the measuring field, T is the temperature at which the measurement is made and t is the measuring time. According to (2) the ZFC and FC magnetization component can be written as:

$$M_{ZFC}(H,T,t) = M_{rev}(H,T) + IRM(H,T,t)$$

$$M_{FC}(H,T,t) = M_{rev}(H,T) + TRM(H,T,t)$$

(4)

Where M_{rev} represents the contribution of the superparamagnetic particles and IRM and TRM represent the irreversible part of magnetization. These are the remanences due to the contribution respectively of the blocked particles whose moments can rotate over the energy barrier due to the presence of the field (almost negligible in our samples), and of the particles that have been blocked in the direction of the cooling field.

From (4) one can relate the magnetization components as follow:

$$M_{FC}(H,T,t) - M_{ZFC}(H,T,t) = TRM(H,T,t) - IRM(H,T,t) \sim TRM(H,T,t)$$

The last approximation is valid for all the samples discussed in this thesis, being $IRM(H,T,t) \sim 0$; in this sense the difference between the FC and ZFC magnetization curves is equal to the thermoremanence and can be used to extract information on the energy barrier distribution. It was indeed demostrated [Spin glass] that the remanence can be fitted by :

$$\frac{M_r}{M_s} = 0.5 \int_{T_B/\langle T_B \rangle}^{\infty} f(T_R)dT_R$$

(5).

Where $\frac{M_r}{M_s}$ is the remanence normalized to the saturation, $T_R = T/\langle T_B \rangle$ is the reduced blocking temperature , $\langle T_B \rangle = KV \log(\tau_m f_0)$ (K is the mean anisotropy constant, τ_m is the measuring time and $f_0 = 10^9 s^{-1}$) and $f(T_R)$ is the distribution of the reduced blocking temperature. Equation (5) shows that, as the temperature $T \to 0$, $\frac{M_r}{M_s} \to 0.5$, i.e. the Stoner-Wohlfarth [83] value for a randomly orientated system.

To analize the temperature dependence of ZFC/FC magnetization of the measured samples, equation (5) can be inverted to express the blocking temperature distribution as a function of the thermoremanence as follow:

$$f(T_B) \propto -\frac{d(TRM)}{dT} \sim -\frac{d(FC-ZFC)}{dT}$$

(6)

It is worth to notice that since $T_B \propto KV = E_A$ the distribution $f(T_B)$ represents also the distriution of the energy barriers. Using this strategy we plotted the $f(T_B)$ in figure 11 as the derivative of the TRM. As can be noticed some hollow samples present a double maximum feature that reflects the presence of two spin population with different thermal behaviour. Assuming that these two population pertain to two indipendent sets of spins like e.g. the bulk and the surface spins, each one with its own energy barrier, a fitting procedure can be set in. For both spin sets, a lognormal distribution of T_B is assumed.

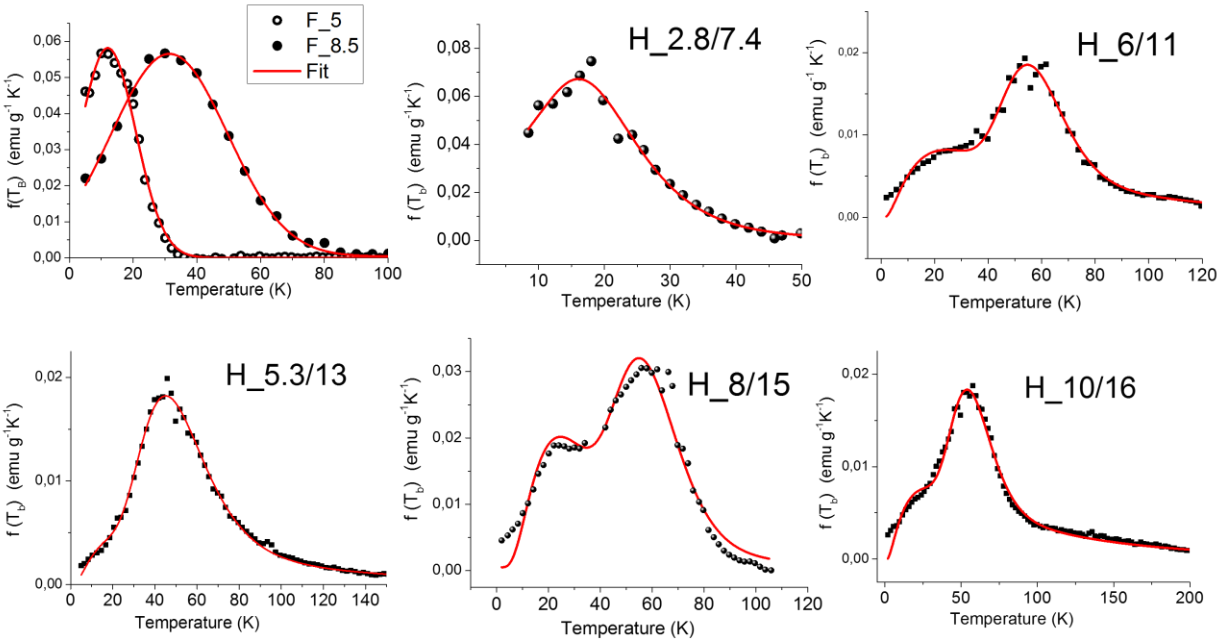

Figure 11 Blocking temperature distribution extracted from ZFC/FC analysis. The distribution of hollow samples is the results of a sum of two lognormal distributions. The full samples presents a single distribution which is almost gaussian.

Table 4 lists the modes of the fitted lognormal distributions (T_B) showing that none of the full samples present a second T_B value while all the hollows can be fitted by means of two blocking temperature.

The associated energy barriers normalized to the Boltzman constant were calculated from:

$$E_A/k_B = T_B \, ln\left(\frac{\tau_m}{\tau_0}\right)$$

where τ_m is the measuring time (10s) and τ_0 is an attempt time of the order of 10^{-9} s.

In full nanoparticles both T_B and E_A increase with the magnetic volume as expected from the existing theories and from previous experimental data [98] . The same can not be said for the hollow samples as can be seen from figure 12 where T_{B1} and T_{B2} are plotted as a function of the magnetic volume and as a function of the shell thickness and the inner to outer diameter ratio.

Sample	*T_{B1} (K)*	*T_{B2} (K)*	*E_{A1}/k_B (K)*	*E_{A2}/k_B (K)*	*A (m^2)*	*B (m^2)*	*A/Area$_{TOT}$*
F_5	0	14 ±2	0	312 ±8	0	0.95	0%
F_8.5	0	31 ±2	0	692 ±8	0	0.91	0%
H_2.8/7.4	7 ±1	16 ±2	165 ±7	348 ± 8	0.84	0.62	58%
H_6/11	26 ±3	56 ±2	576 ±13	1245 ±12	0.73	0.36	67%
H_5.3/13	30 ±3	49 ±2	670 ±14	1302 ±9	0.50	0.54	48%
H_8/15	24 ±4	57 ±2	545 ±16	1266 ±9	0.86	0.70	55%
H_10/16	29 ±5	56 ±2	641 ±19	1245 ±9	0.90	0.40	69%

Table 5 In the first four columns are listed the modes of the lognormal distributions which fit the f(T_B) curves (and the corresponding energy barriers). A and B are the areas under each distribution; the last column indicates the normalized weight in percentage of the distribution related to the lower T_B which can tentatively be ascribed to the surface spins.

The blocking temperatures are found to be constant within the experimental error range. Only sample H_2.8/7.4, the smallest hollow sample, slows at lower T_B. A tentative explanation can be given taking into account the small size of the sample corresponding to a lower magnetic volume and a lower number of crystallites composing the magnetic structure in the hollow topology: lower magnetic anisotropy and blocking temperature are expected with respect to the other samples. The fact that T_B and E_A have similar valus for all the other samples, is not easy to justify but is in agreement with the trend of M_S. Possible origin of this behaviour are the high number of morphological parameters (S/V, shell thickness, number of crystallites, etc..) which influence the magnetic behaviour leading to similar spin blocking temperature even if the magnetic volume of the investigated systems is not the same.

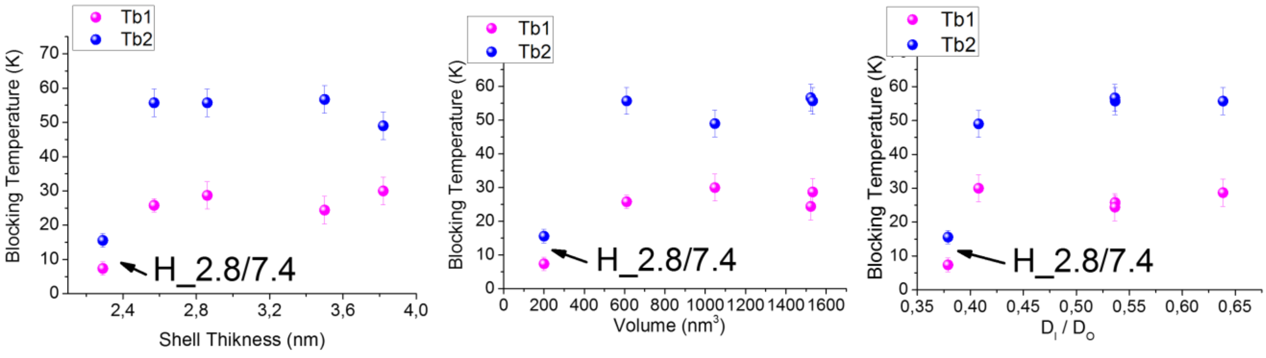

Figure 12 Blocking temperatures extrected from the distributions of figure 11 as a function of the most significative experimental parameter such as the shell thickness (a), magnetic volume (V) and inner to outer diameter (D_i/D_o).

To check if the second spin population found in the hollow system can be related to the surface spins, the normalized area under $f(T_{B1})$ was calculated and plotted versus the mean canting angle (obtained from Mössbauer) and shell thickness. Figure 13a shows that the percentage weight (A%) of the spin population 1 monotonically increases with the spins' mean canting angle indicating (see figure 13) a direct dipendence of A% to the normalized volume of the surface (i.e. volume of the shell composed by the canted spins of the inner and outer surface V_S normalized on the total volume V).

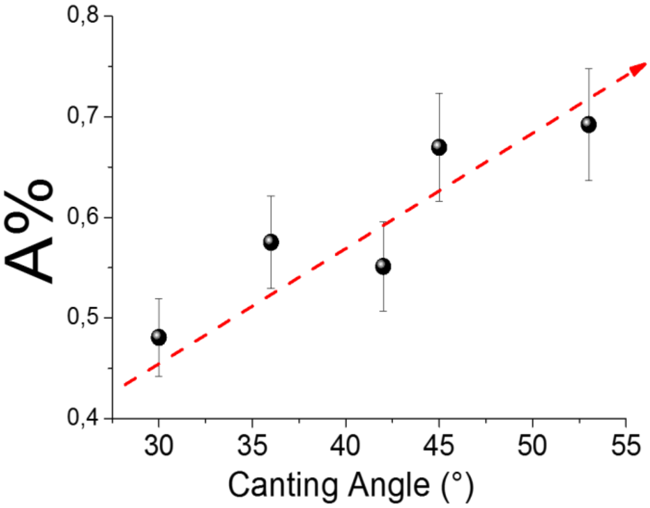

Figure 13 Percentage weight of the surface component extracted from the blocking temperature distribution as a function of (a) the average spins' canting angle

IV. Conclusions

The static magnetic properties of two full samples and five hollow samples of iron oxide nanoparticles were investigated and compared.

At low temperature all samples show a ferrimagnetic behaviour, but in the hollows the spins more hardly follow the external magnetic field, which results in lower magnetic moments, higher coercive and irreversibility fields, and no magnetic saturation. This observation is associated to the particular arrangment of the crystallographic domains in the hollow geometry and to a high effective anisotropy which arises from the extended amount of paramagnetic spins at the surface and at the interface of such polycrystalline nanostructures. In particular at low temperature, the exchange interactions between spins with different crystallographic easy axis inside the shell have a noticeable but not dominant influence on the hysteresis loop. The crystallographic anisotropy acts like a glue fixing the spin orientation, following the anisotropy axis of the randomly orientated crystallographic domains. In this scenario, the exchange interaction between different crystallographic domains inside thin polycrystalline shells is not sufficient to align the magnetic moment of each crystallite into a unique direction. The proof of the previous consideration is in line with other results found in literature [63,64] which show that intercrystallites intaraction in a hollow nanoparticle it is not as high as the the intrarcrystallites interaction (i.e. the blocking temperature – here rapresented by the max of the ZFC- of a hollow nanoparticle is lower than the one of a single particle having the same volume of the whole hollow particle). On the other hand the intercrystallite interaction is not negligible (i.e. the blocking temperature – here rapresented by the max of the ZFC- of a hollow nanoparticle is higher than the one of a single particle having the same volume of one of crystallite composing the hollow particle). See figure 14 for a pictorial explanation.

$$T_B^V \quad < \quad T_B^{V^{Hollow}} < T_B^{V^{Full}}$$

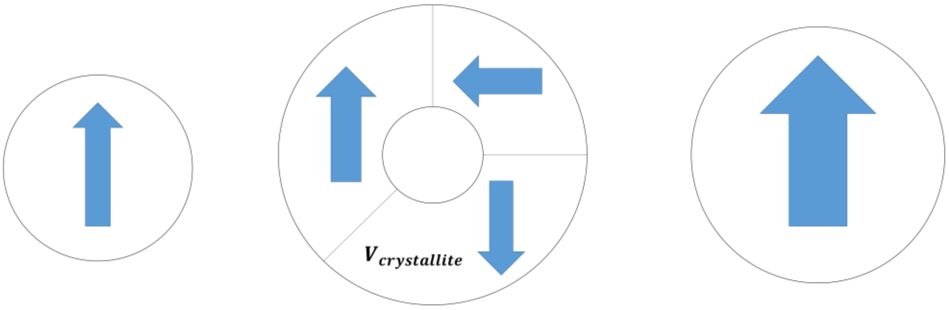

$$V = V_{crystallite} \qquad V^{HOLLOW} = \sum_I V^i_{crystallite} \qquad V^{FULL} = V^{HOLLOW}$$

Figure 14 Pictorial rapresentation of three comparable nanoparticles (a) full particle having the same magnetic volume as one crystallite composing (b), an hollow nanoparticle, with the same total magnetic volume of (c), a full nanoparticle.

As a result, the hysteresis loops resemble those of frustrated and disordered magnets such as random anisotrpy systems.

At high enough temperatures, the thermal agitation permits spins of different crystallites cores to detach from crystallographic anisotropy axis and to follow the applied magnetic field and the weaker intercrystal interactions. In this way, in the superparamagnetic regime, the spins of the crystallites core within the shells tend to align coherently throughout the entire particle. A linear contribution was found in the magnetization curves of the hollows: it was quantified by means of a paramagnetic susceptibility and associated to the number of paramagnetic surface spins.

DC magnetic measurements as a function of temperature in ZFC and FC configurations confirm the presence of two spin populations in the hollow samples, which reduce to one spin population in the full samples. We ascribed the two blocking temperature distributions to the core and surface spins population, this last having not enough relevance to be seen in the full samples. The calculated energy barrier is higher in the hollows with respect to the full system, thus confirming the previous considerations about the complex anisotropy of these systems which is expected to arise from the surface and from the multiple easy axis contributions. The weight of the surface spin population was linked to the morphological parameters such as the canting angles and the shell thickness. In particular an higher surface contribution was found for particle H_6/11 which is the sample presenting higher canting angle and higher D_i/D_o ratio. The shell thickness was found to play a role in the cristallinity of the samples. Larger shell thicknesses would provide larger crystal domain sizes but also a lower number of crystallites (i.e. more crystallites are expected in thinner shells). In this sense the surface contribution can be tuned by the shell thickness, in particular we found a threshold value around 2.8nm for which the surface contribution is maximized.

CHAPTER 3:

SPIN DYNAMICS INVESTIGATION

I. Overview

In this chapter we present a study of the local spin dynamics in full and hollow nanoparticles.

The spin dynamics has been investigated using the wide (different) frequency windows (10kHz<f<400MHz and more) of ^{1}H nuclei and polarized positive muons μ^+. Both these systems are local probes, whose spins precess around a local field in the sample with a Larmor precession frequency driven by the gyromagnetic ratio of 42.576 MHz/T and 135.539 MHz/T of ^{1}H nucleus and muon respectively.

NMR (nuclear magnetic resonance) relaxometry, in addition to the superparamagnetic (SPM) relaxation, revealed a paramagnetic (PM) contribution in the longitudinal relaxation of the protons which we ascribed to the surface disordered spins. The PM contribution is not visible in the full sample data used as reference. The experimental curves were succesfully fitted by a novel model which accounts for the PM and SPM nuclear relaxation, due to the surface and core spins respectively.

MuSR (muon spin resonance) mesurements as a function of temperature in a longitudial external applied field of 150G revealed the presence of a uniform local field in hollow and full samples, below the so-called blocking temperature (different for different samples) which assumes a lower value in the former case. The evidence of a lower local field in the hollow sample was associated to the lower order parameter presented by the hollow topology which is due to the thicker disordered surface layer in these samples. Three different muon implantation sites were identified in the relaxation of the muon asymmetry. The slower relaxation rates (i.e. far from magnetic centers) was analyzed as a function of T by a BPP-like fitting function and revealed the different dynamics which are present in F_5 and H_2.8/7. In particular at low temperatures the system is in a blocked spin state and the relaxation is driven from the slowing of the Ne'el reversal of the magnetization while at high temperatures the dynamics becomes faster and faster reflecting a typical thermally activated superparamagnetic state.

II.i ^{1}H-NMR relaxometry

In NMR spectroscopy in presence of unpared electrons like in paramagnets and other magnetic systems, generally the dominant perturbations are the hyperfine (either dipolar or contact) nucleus-electron interaction, and the like and/or unlike nuclear-nuclear (dipolar) interaction. This is the case of MNPs investigated in the present thesis. To follow the effects of such interactions, the time evolution of the nuclear magnetization is studied, as direct probe of the nucleus-nucleus interaction and indirect probe of the hyperfine coupling, possibly mediated by the electron spin coupling with the surroundings.

The general treatment of NMR starts from the observation that in order to build up an observable, non-zero magnetization one has to apply a magnetic field $\boldsymbol{H}_0$ (for example in the z direction). Accordingly, the equilibrium nuclear magnetization $M_0 = \gamma^2\hbar^2 I(I+1)H_0/k_B T$ (γ is the gyromagnetic ratio) precesses around $\boldsymbol{H}_0$ at the Larmor frequency $\boldsymbol{\omega}_0 = \gamma\boldsymbol{H}_0$. It is important to note that $\boldsymbol{H}_0$ is applied just to generate a nuclear magnetization as quantity that produces the NMR signal, but we are interested in the time evolution of $\boldsymbol{M}$ due to the interactions with other degrees of freedom of the system (e.g. electron spins, other nuclear spins, etc..). To study the evolution of **M**, it’s more useful and simple to consider as reference system the rotating frame of the magnetization $\mathbf{M}_0$ at a certain frequency $\boldsymbol{\omega}_0$; and so all the motions with different angular frequecies can more easily be associated to an external perturbation.

Once the static field $\boldsymbol{H}_0$ is applied, the nuclei has to be perturbed to let them reaching an out-of-equilibrium situation, and then left free to relax to the equilibrium. To perturb the nuclei a small RF field $\boldsymbol{H}_1$ rotating at frequency $\boldsymbol{\omega}$ is applied perpendicular to $\boldsymbol{H}_0$. As a result, the magnetization (static in the rotating frame) precesses around $\boldsymbol{H}_1$ at the frequency $\boldsymbol{\omega}_1 = \gamma \boldsymbol{H}_1$. In particular, for $\omega = \omega_0$ the RF field (RF pulse) will drive M away from the z-axes by an angle given by: $\cos(\vartheta(t)) = 1 - 2sin^2(\frac{\omega_1 t}{2})$.

From a quantum mechanical point of view we induce a perturbation $H_1(t) = -\gamma\hbar \boldsymbol{H}_1(t)$ on a Zeeman hamiltonian $H_0 = -\gamma\hbar \boldsymbol{H_0}$. The perturbation gives enough energy to the system such that it can change the spin orientation for example from $|+\rangle$ (spin un) to $\langle -|$ (spin down),corresponding to a transition among energy levels through a resonant process. The process is equivalent to the rotation of **M** from the z axes by an angle e.g. $\vartheta(t) = \frac{\pi}{2}$ (i.e. null longitudinal component with respect to z). In this sense the longitudinal component M_z (sum of magnetic moments associated to the nuclear spins, renormalized by the volume) is in direct correspondence with the quantum mechanical operator $\langle \boldsymbol{M} \rangle$ whose statistical value is given by the usual Boltzmann formula (calculated over the two Zeeman energy levels in the case of ^{1}H nuclei, spin I=1/2)

It is worth to notice that no correspondence between quantum mechanical and classical approach exists to picture the transverse part of the magnetization with respect to the z direction (M_{xy}).

The above described situation is the starting point of an NMR relaxation experiment: the capability of the system to “relax” back to equilibrium after an external perturbation occurred, can be measured through the time evolution of $\boldsymbol{M}$.

II.i ^{1}H nuclei as local probe

The key point of the NMR spectroscopy is that we observe nuclei (better to say the time evolution of the nuclear magnetization) to extract information on the system in which they are “living”. Due to their high natural abundance of 99.9% the Hydrogen nuclei (called protons, i.e. ^{1}H) are very good candidates as local probe. The protons possess spin $I = 1/2$ so that a Zeeman interaction with a static field H_0 produces a split of the energy level in two different values separated by the transition energy $\Delta E = \hbar\omega_0$. The two levels are differently populated according to the Boltzmann statistics (in particular $N\uparrow > N\downarrow$) so that a net nuclear magnetization builds up. A perturbation H_1 at frequency $\omega = \omega_0$ induces a transition between the two Zeeman levels thus changing the net value of the nuclear magnetization.

After a RF pulse has been applied (RF field switched off after few ms or less), one can detect, with the same coil used to apply the RF, the voltage induced by the time evolution of the nuclear magnetization which relax to its equilibrium. According to Faraday-Maxwell’s law this voltage is proportional to the precessional frequency in the laboratory frame of reference and to the nuclear in-plane magnetization $<M_{xy}(t)>$. The signal detected by the coil in the laboratory can be transformed in the rotating frame by mixing it with a reference oscillating at ω_0. The low frequency signal at the output of the mixer is the so-called FID (Free Induction Decay) signal.

Again, the key point is that the nuclear magnetization will relax in a time which is inversely proportional to the capability of the nuclei of exchange energy with the surroundings. The probability to find an oscillation of the investigated system (for example vibrational, rotational motions, or electronic field oscillations) which matches the nuclear Larmor frequency ω_0 is proportional to the spectral density function of the electron evaluated in $\omega = \omega_0$. In this sense by measuring the relaxation time of the nuclei as local probe in a wide frequency range of ω_0 (i.e. by appling several different H_0) it is possible to access *directly* , through the hyperfine interaction, the correlation function of the electrons.

It is important to note that the ^{1}H gyromagnetic ratio is $\gamma = 42.576\ MHz/T$ and the available static fields in laboratory are in the range $2\text{x}10^{-4} \div 9$ T so that the frequency range accessible in the ^{1}H NMR dispersion curves (^{1}H NMR-D) is in the range $0.01 \div 400$ MHz.

We want now to introduce the most relevant information on the studied compound that we can get from a pulsed NMR experiment, particularly from the spectra and the longitudinal and transversal relaxation times (T_1 and T_2 respectively).

Nuclear relaxation: T_1 and T_2

The relaxation time (i.e. the time between the end of the perturbation and the end of its memory in the system) is not unique. After the perturbation that "rotates" the total magnetization in the xy (transverse) plane, after a certain time the magnetization rebuilds in the z (longitudinal) direction identified by H_0. The relaxation process experienced by the nuclear magnetization is associated to a non-conservation of the total magnetic moment. A consequence of the non conservation law in a non rigid motion of the magnetization vector so that the time required to the magnetization to reduce to zero in the xy plane (T_2) is generally less or much less than the time T_1 required to rebuild in the z direction (we'll see later that in our systems this is not always the case, the very low frequency region being an exception). In order to understand this evidence one has to deal with the different processes and interactions causing the relaxation in the longitudinal direction and in the transverse plane.

In the NMR experiment the sample contains a statistical ensemble of nuclear spins and hence one has to consider how the statistical average of the spin components (i.e. the component of nuclear magnetization) evolves in time. The statistical average can be written as

$$\langle\overline{I_{x,y,z}}\rangle = \sum \langle m|I_{x,y,z}|m\rangle \frac{e^{-E_m/k_BT}}{Z}$$

with |m> eigenstates of $H = -\gamma\hbar I_z H_0$.and Z partition function of the system. In the case of ^{1}H nuclei ($I = 1/2$) the mean value of I along the z direction is:

$$\langle\overline{I_z}\rangle = \frac{1}{2}\frac{e^{-\gamma\hbar H_0/2k_BT} - e^{\gamma\hbar H_0/2k_BT}}{e^{-\gamma\hbar H_0/2k_BT} + e^{\gamma\hbar H_0/2k_BT}}$$

and the mean value of I in the xy plane is

$$\langle\overline{I_{xy}}\rangle = 0$$

Consider now the experimental configuration introduced before, where $H_0 \parallel$ z and the RF field H_1 is perpendicular to it. Then $\mathcal{H} = \mathcal{H}_0 + \mathcal{H}_1(t)$, where $\mathcal{H}_1 = -\gamma\hbar I_x H_1$ can be treated as a perturbation of $\mathcal{H}_0 = -\gamma\hbar I_z H_0$. The quantum mechanical description of the time evolution of $\langle\overline{M_{xy}(t)}\rangle$ based on the perturbation theory can become a hard task if the hyperfine interactions are involved. Therefore it is convenient to consider the phenomenological equations derived by Bloch [84] which describe the time evolution of the components of the nuclear magnetization in the lattice (from now we will indicate the component of nuclear magnetization with $M_{x,y,z} = \langle\overline{M_{x,y,z}}\rangle$):

$$\frac{dM_z}{dt} = \gamma(M \times H_0)_z + \frac{M_0 - M_z}{T_1}$$

(1)

$$\frac{dM_{xy}}{dt} = \gamma(M \times H_0)_{xy} - \frac{M_{xy}}{T_2}$$

(2)

The two characteristic decay times have been introduced in eq.(1) and eq.(2) : T_1 the spin-lattice relaxation time and T_2 the spin-spin relaxation time. T_1 describes the time evolution of M_z and it is therefore directly related to the modifications in the population of the Zeeman levels which can occur after the exchange of energy with the lattice excitations. The decay of M_{xy} occurs in a time T_2, which is affected not only by the process involved in the spin lattice relaxation but also by other processes such as the nuclear dipole-dipole interaction which acts as a dephasing process for each spins in the xy plane (and a consequent decrease of M_{xy}), and doesn't imply exchange of energy with the lattice.

The real and imaginary part of the nuclear susceptibility can be estimated by driving the in-plane component of the magnetization (x and y) which oscillates in phase and out of phase by $\frac{\pi}{2}$ with the RF field. In particular it can be demonstrated that:

$$\chi'(\omega) = \frac{M_0}{H_0}\frac{\omega_0(\omega_0 - \omega)T_2^2}{1 + (\omega_0 - \omega)^2 T_2^2}$$

(3)

$$\chi''(\omega) = \frac{M_0}{H_0}\frac{\omega_0 T_2}{1 + (\omega_0 - \omega)^2 T_2^2}$$

(4)

The dissipative part of the nuclear spin susceptibility is a Lorentzian of width $1/T_2$ centered around ω_0. The resonance is so defined as a peak in the absorption of the RF field at the Larmor frequency which is spread over a width determined by the nuclear spin-spin relaxation.

NMR Spectra

When the sample under investigation is placed into the coil of the experimental set-up of a NMR experiment one observes a change in the inductancewritten as $L = L_0[1 + 4\pi\chi(\omega)]$ and a corresponding variation of the resistance of $\Delta R = L_0\omega 4\pi\chi''$. Then one can estimate the average power adsorbed by the nuclei

$$\mathrm{P}(\omega) = \frac{1}{2}\omega H_1^2 \chi''(\omega) V$$

(5)

where V is the sample volume. For $= \omega_0$, by recalling the expression (4) in the weak field limit one has $\mathrm{P}(\omega_0) = \frac{1}{2}\omega_0^2 H_1^2 \chi_0 V T_2$. As the spacing between adjacent hyperfine levels is not the same for all nuclei it is convenient to introduce a distribution function $f(\omega)d\omega$ giving the fraction of nuclei with a resonance frequency between ω and $\omega + d\omega$. In this case the energy adsorbed per unit time by the nuclei is

$$\mathrm{P}(\omega) = \frac{1}{2}\omega\omega_0\, H_1^2 \chi_0 f(\omega) 2\pi$$

By comparing this expression with the one (eq. (5)) previously derived for $\mathrm{P}(\omega)$ χ'' can be expressed as $\chi''(\omega) = \chi_0\omega_0\, f(\omega)2\pi$. Since the variation of resistence due to the NMR signal is $\Delta R = L_0\omega 4\pi\chi''$ we can conclude that the signal detected in a NMR experiment is directly proportional to $\mathrm{P}(\omega)$, proportional to $\chi''(\omega)$ and gives the number of nuclei which are resonating with a frequency between ω and $\omega + d\omega$.

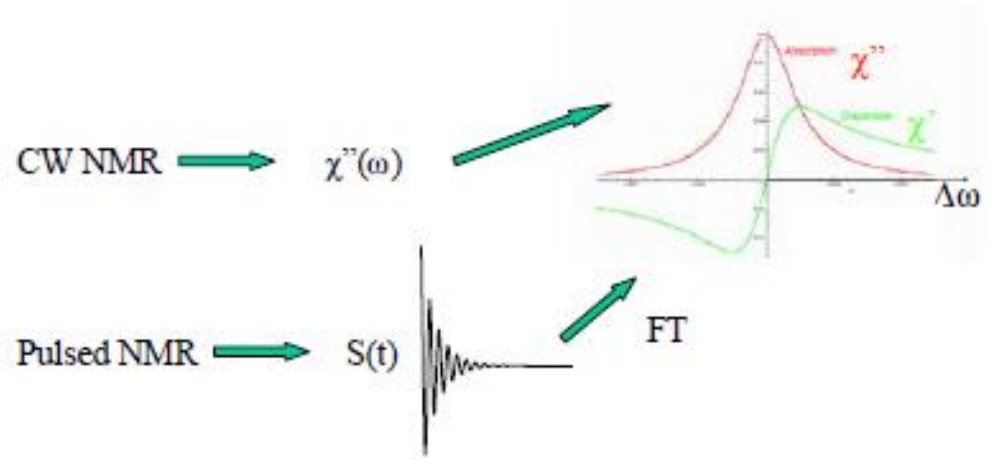

Figure 1: Schematic illustration of the equivalence of the NMR spectra derived fron CW NMR and from pulsed NMR spectroscopy.

This last is called NMR spectrum and actually correspond to the Fourier transform at frequency ω of the correlation function for the transverse components of the nuclear magnetization and proportional to the signal measured in the pulsed NMR experiment (see figure 1).

In order to understand the link between the correlation function and the NMR spectra it is necessary to have in mind the fluctuation-dissipation theorem:

$$f(\omega) \propto \chi''(\omega) = \frac{\omega}{k_B T}\int_0^\infty e^{i\omega t} \langle \overline{M_x(t) M_x(0)} \rangle\, dt$$

II.ii Theories on nuclear relaxation induced by magnetic nanoparticles: SPM and PM contribution

As discussed before, the nuclear relaxation times T_1 and T_2 can give direct information on the electronic system. In this thesis we are interested in the electronic spins dynamics in magnetic nanoparticles, in particular when they assume a hollow topology. The curve which describe the evolution of the T_i (i=1,2) with the external applied field (i.e. the precession frequency of the nuclear spins) is called NMR dispersion curve (NMR-D) and contains information on the spectral density function of the electrons composing the nanoparticles. In other words one can access the probability to find an electronic fluctuation at a certain frequency by modelling the evolution of the nuclear relaxation as a function of their initial polarization.

Here below the existing models of proton (^{1}H) relaxation induced by superparamagnetic nanoparticle (SPM models) are summarized with particular attention to the information that can be extracted. Actually, we expect that the relaxation induced by the full particles under investigation would follow the SPM model. On the other hand the hollow particles display a linear (paramagnetic) contribution to the magnetization (see chapter 2) so that we expect to have a paramagnetic contribution to the nuclear relaxation as well. For these reasons below is given also a description of the relaxation induced by a dilute paramagnetic compound (PM relaxation)

Nuclear relaxation mechanisms

The paramagnetic center influences usually the relaxation of water molecules which interacts directly with it and its coordinates molecules. The paramagnetic relaxation is caracterized by two contributions: the inner sphere and the outer sphere (see figure 2).

Inner sphere

The principal contribution to the inner sphere relaxation comes from the chemical exchange of the water molecules of the first coordination sphere with bulk water molecules, that in this way enter in closer "contact" with the electronic spin (mainly via dipole-dipole hyperfine interaction); after leaving the first sphere coordination they are replaced by other bulk molecules. This event is characterized by a correlation exchange time τ_M.

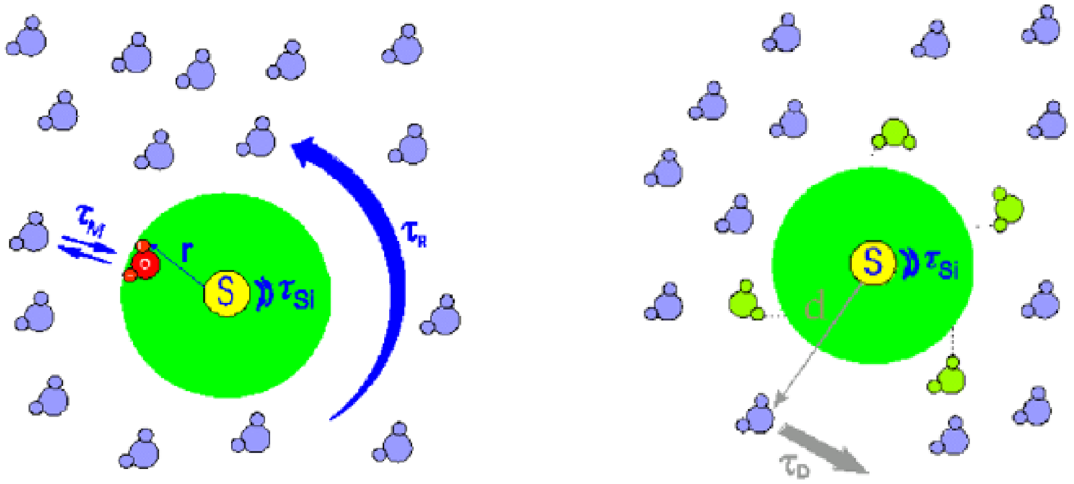

Figure 2: Schematic illustration of the (a) inner sphere and (b) outer sphere contribution to the relaxation of the nuclei of solvent molecules (in the picture the solvent is rEpresented by water molecules)

This mechanism allows the propagation of the paramagnetic effect to the totality of the solvent.

The other two correlation times contributing to the mechanism of nuclear relaxation are the Brownian rotational time τ_R and the electronic correlation times of the magnetic center τ_{s1} and τ_{s2} (respectively longitudinal and transversal).

Taking into account all these correlation times, the inner sphere model has been described by the Solomon Bloembergen-Morgan theory (SBM) [88-89]. The inner sphere contribution is given by:

$$\frac{1}{T_1{}^{IS}} = fq\frac{1}{T_{1M} + \tau_M}$$

Where

$$\frac{1}{T_{1M}} = \frac{2}{15}\left(\frac{\mu_0}{4\pi}\right)^2 \gamma_H^2\gamma_S^2\hbar^2 S(S+1)\frac{1}{r^6}\left[\frac{7\tau_{c2}}{1+(\omega_S\tau_{c2})^2} + \frac{7\tau_{c1}}{1+(\omega_H\tau_{c1})^2}\right]$$

and

$$\frac{1}{\tau_{ci}} = \frac{1}{\tau_R} + \frac{1}{\tau_M} + \frac{1}{\tau_{si}}$$

(5)

where $\frac{1}{\tau_{s1}} = \frac{1}{5\tau_{SO}}\left[\frac{1}{1+(\omega_S\tau_V)^2} + \frac{4}{1+(\omega_S\tau_V)^2}\right]$ (6) and $\frac{1}{\tau_{s2}} = \frac{1}{10\tau_{SO}}\left[3 + \frac{5}{1+(\omega_S\tau_V)^2} + \frac{2}{1+(\omega_S\tau_V)^2}\right]$ (7)

there *f* is the relative concentration of the paramagnetic complex and of the water molecules; q is the number of water molecules in the first coordination sphere; τ_M is the water residence time; T_{1M} is the nuclear longitudinal relaxation time of the water proton nuclei of the first coordination sphere; γ_S and γ_H are the gyromagnetic ratios of the electron (S) and of the proton (H), respectively; $\omega_{S,H}$ are the angular frequencies of the electron and of the proton; r is the distance between coordinated water protons and the unpaired electron spin; $\tau_{c1,2}$, the correlation times modulating the interaction, are defined by eq. 5 – where τ_R is the rotational correlation time of the hydrated complex and, as said above, $\tau_{s1,2}$ are the longitudinal and transverse relaxation times of the electron. These latter parameters are field-dependent (Eqs. 6 and 7). τ_{SO} is the value of $\tau_{S1,2}$ at zero field and τ_v is the correlation time characteristic of the electronic relaxation times.

Outer sphere

The outer sphere relaxation is explained by the dipolar interaction at long distance between the spin of the paramagnetic substance and the nuclear spin. The mechanism is modulated by the translational diffusion time ($\tau_D = d^2/D$) that takes into account the relative molecular diffusion constant (D) as well as the distance of minimum approach of the paramagnetic compund and the solvent molecules (d).

The samples of nanoparticles investigated in this thesis are different from the small paramagnetic molecules for which the inner sphere contribution is important; in particular we don't expect any exchange site around the nanoparticles. For this reason even if the surface spins of the hollow nanoparticles act like paramagnets we expect only an outer sphere contribution to the nuclear relaxation, this last being described below.

A simple expression to describe the modified outer sphere superparamagnetic relaxation which could be suitable for the investigated system takes into account:

1) *The contribution from the surface spins.* The surface spins are characterized by a correlation time which is the result of the diffusion time τ_D and the magnetization reversal correlation time τ_S of the surface electron spins, i.e. : $\frac{1}{\tau_c} = \frac{1}{\tau_S} + \frac{1}{\tau_D}$. These spins, having a lower coordination with respect to the bulk ones, are more “free” to move so that they can be cosidered as belonging to a paramagnet. In particular, for the surface spin system the longitudinal paramagnetic relaxation contribution can be tentatively assumed as:

$$\frac{1}{{T_1}^{PM}} = \chi T \tilde{A} \frac{\omega \tau_c}{1 + \omega^2 \tau_c^2}$$

(6)

Where $\tilde{A}$ is the hyperfine constant.

2) *The contribution of SPM bulk NPs,* through the usual Roch expression [85].

In the case of SPM NPs core, as said before (contribution 2 to the modified outer sphere relaxation mechanism), the Roch heuristic model is the most used. In general all the theoretical models postulate that relaxation arises from the magnetic inhomogeneities produced by the dipolar magnetic field of the particles which depends itself on the magnetic moment of the nanoparticles. In this context there exists al least three source of fluctuation for the protons: (i) the proton diffusion in the field inhomogeneity, (ii) the Neél relaxation of the electronic spins and (iii) the brownian relaxation of the SPM magnetization. In the following expression ω_I is the anisotropy frequency of the nanoparticles is assumed to be uniaxial, the SPM magnetic moment is supposed to follow a Boltzmann distribution and the NPs are supposed uniformly distribuited in the solution.

Roch et al. proposed [85,86] the first theoretical model which fitted the experimental data. The key point is that when the anisotropy is high enough, one can consider the electronic spin locked to the anisotropy axes while when the anisotropy decreases the electronic spin can precess around the external field. More recently a new model was presented by Levy et al. [87], more suited for high anisotropy SPM nanoparticles. In this thesis we used the Roch model to describe the longitudinal relaxation, briefly presented below.

The hypotesis at the basis of the model are: (*a*) the rotational correlation time is assumed to be much larger than the magnetization reorientation time ($\tau_R \gg \tau_N$), (*b*) the Neèl time τ_N is assumed to be the same for all nanoparticles and (*c*) the exchange interaction is the most important contribution to the total energy within a particles (i.e. all the magnetic moments are alligned). The last hypotesis is the less appropriate for our hollow systems which present a double thick layer of disordered spins.

The equations describing the SPM relaxation induced by the fluctuating dipolar interaction between the particles’ superspin and the magnetic moment of the hydrogen nuclei are [85,86]:

$$
\begin{aligned}
\frac{1}{T_1{}^{SPM}} = \frac{32\pi}{35000}\hbar^2\gamma_S^2\gamma_I^2\left(\frac{N_A C}{r_d D}\right)\Big\langle\sum_{ij}\frac{\exp(-\beta E_i)}{Z}\Big\{\frac{S_{-,ij}S_{+,ij}+S_{+,ij}S_{-,ij}}{2}\Big[\frac{1}{2}J^F(\omega_I-\omega_{ij},\tau_D,\tau_N)\\
+3J^F(\omega_I+\omega_{ij},\tau_D,\tau_N)\Big]+\frac{3}{2}\left|S_{z,ij}\right|^2\left[J^F(\omega_I-\omega_{ij},\tau_D,\tau_N)+J^F(\omega_I+\omega_{ij},\tau_D,\tau_N)\right]\Big\}\\
-3\langle S_z\rangle^2\left[J^F(,\tau_D,\tau_N)-J^A\left(\sqrt{2\omega_I\tau_D}\right)\right]\Big\rangle
\end{aligned}
$$

(7)

$$
\begin{aligned}
\frac{1}{T_2{}^{SPM}} = \frac{32\pi}{35000}\hbar^2\gamma_S^2\gamma_I^2\left(\frac{N_A C}{r_d D}\right)\Big\langle\sum_{ij}\frac{\exp(-\beta E_i)}{Z}\Big\{\frac{S_{-,ij}S_{+,ij}+S_{+,ij}S_{-,ij}}{2}\Big[\frac{1}{4}J^F(\omega_I-\omega_{ij},\tau_D,\tau_N)\\
+\frac{3}{2}J^F(\omega_{ij},\tau_D,\tau_N)+\frac{3}{2}J^F(\omega_I+\omega_{ij},\tau_D,\tau_N)\Big]\\
+\left|S_{z,ij}\right|^2\left[\frac{3}{4}J^F(\omega_I-\omega_{ij},\tau_D,\tau_N)+2J^F(\omega_{ij},\tau_D,\tau_N)+J^F(\omega_I+\omega_{ij},\tau_D,\tau_N)\right]\Big\}\\
-2\langle S_z\rangle^2\left\{\left[J^F(0,\tau_D,\tau_N)+\frac{3}{4}J^F(\omega_I,\tau_D,\tau_N)\right]-\left[J^A(0)+\frac{3}{4}J^A\left(\sqrt{2\omega_I\tau_D}\right)\right]\right\}\Big\rangle
\end{aligned}
$$

(8)

Please note that the spin operator S_{ij} contains the angle θ between the anisotropy axes and the external magnetic field so that an average over the possible orientations has to be done. Here below is presented a legend for Eqs. (7) and (8).

- γ_S , γ_I are the gyromagnetic ratio of electron and proton respectively
- N_A is the Avogadro number
- C is the iron concentration
- D is the self diffusion coefficient
- r_d is the minimum approach distance of the protons to the nanoparticle, usually bigger than the magnetic radius due to the presence of the coating.
- S is the spin operator
- τ_D is the diffusion correlation time
- ω_I and $\omega_{i,j}$ are the proton and the electron Larmor frequency respectively.

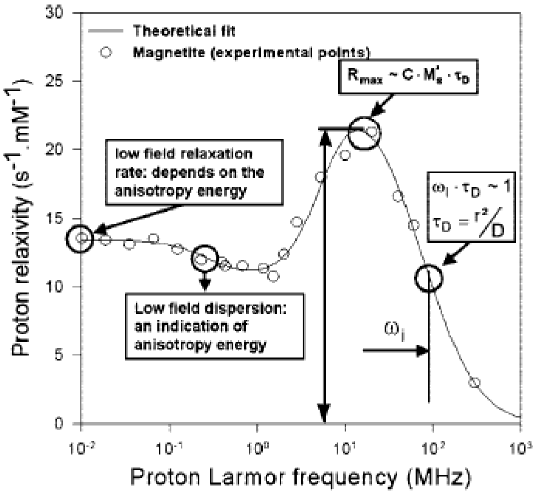

Figure 3 Longitudinal relaxation simulated at room temperature for a particle of r=4nm and M_S = 53 Am^2/Kg in colloidal solution [97]

At high field the magnetic vector is locked along the external field **H**0 and the Curie relaxation dominates. The corrisponding relaxation rates are given by the high anisotropy model with infinite value of τ_N . The spectral density function which dominates in this case is the Ayant function

$$J^A(z) = \frac{1 + 5z/8 + z^2/8}{1 + z + z^2/2 + z^3/6 + 4z^4/81 + z^5/81 + z^6/648}$$

with $z = \sqrt{2\omega_I \tau_D}$ which depends only on the proton Larmor frequency. The dispersion of this function occurs at $\omega_I \tau_D \sim 1$(see figure 4) .

At intermediate field the relaxation rates are a combination of the high and low field contribution weighted by factors depending on the Langevin function, which gives the average magnetization of the sample.

At low field the assumption of infinite anisotropy become less and less valid and this results in a low field dispersion not predicted by the high anisotropy model. To evaluate the low field component a finite anisotropy and the Neél time has to be taken into account, thus obtaining the Freed spectral density function

$$J^F(\omega, \tau_D, \tau_N) = \frac{1 + \Omega^{1/2}/4}{1 + \Omega^{1/2} + 4\Omega/9 + \Omega^{3/2}/9}$$

where $\Omega = (i\omega + 1/\tau_D)\tau_N$.

Please note that the Ayant function is the limit of the Freed function when $\omega\tau_N \gg 1$.

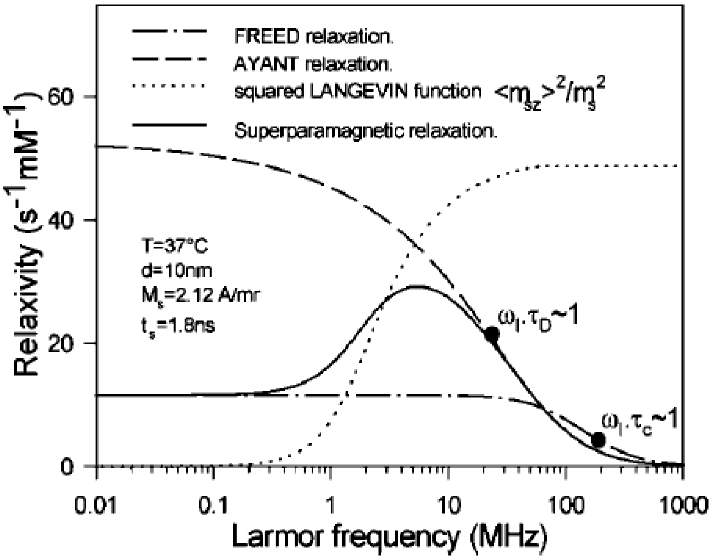

Figure 4 Spectral density functions which compose the superparamagnetic relaxation model

Even though equations (7) and (8) are suitable for exact simulation profiles, the time required for the experimental data fitting is somehow prohibitive expecially if the number of spins in the particle (i.e. the magnetic volume) becomes more than 1000. For this reason we performed the fitting of the experimental data by an heuristic model proposed by the same autors [85], where the nuclear relaxation times are expressed as

$$\frac{1}{T_1^{SPM,heu}} = \frac{32\pi}{35000}\mu_{SPM}^2\gamma_I^2\left(\frac{N_A C}{r_d D}\right)\left\{7P\frac{L(x)}{x}J^F(\omega_S,\tau_D,\tau_N) + \left[7(1-P)\frac{L(x)}{x} + 3\left(1-L^2(x)-\frac{2L(x)}{x}\right)\right]\cdot J^F(\omega_I,\tau_D,\tau_N) + 3L^2(x)J^A\left(\sqrt{2\omega_I\tau_D}\right)\right\}$$

(9)

$$\frac{1}{T_2^{SPM,heu}} = \frac{16\pi}{35000}\mu_{SPM}^2\gamma_I^2\left(\frac{N_A C}{r_d D}\right)\left\{13P\frac{L(x)}{x}J^F(\omega_S,\tau_D,\tau_N) + 7(1-P)\frac{L(x)}{x}J^F(\omega_I,\tau_D,\tau_N) + 6(1-P)\frac{L(x)}{x}J^F(0,\tau_D,\tau_N) + \left[1-L^2(x)-\frac{2L(x)}{x}\right]\cdot\left[3J^F(\omega_I,\tau_D,\tau_N)+4J^F(0,\tau_D,\tau_N)\right] + L^2(x)\left[3J^A\left(\sqrt{2\omega_I\tau_D}\right)+4J^A(0)\right]\right\}$$

(10)

where P is a parameter indicating the magnetic anisotropy degree of the sample, such that the equations (9) and (10) can be seen as a linear combination of the relaxation rate in the limit of high (P=0) and low (P=1) anisotropy degree.

The fitting analysis of the proton NMR-D profiles with (9) and (10) can give us :

(i) The average *magnetic volume V_{NMR}* partecipating to the superparamagnetic relaxation

(ii)The average *distance of minimum approach* of the proton to the center of the nanoparticles (i.e. *d*)

(iii) The *Neèl magnetization reversal time* of the superparamagnetic electron spins (i.e. τ_N)

II.iii Experimental section:

In this section the experimental NMR-D curves and the corresponding data analysis are presented.

Experimental data

The complete NMR-D has been measured over the frequency range 0.01-60 MHz for all samples. Two instruments were used in order to perform the measurements over a such wide frequency range: (i) a Stelar Spinmaster for the range 7.2-60 MHz, (ii) a Stelar Smatracer for the range 0.01-7.2Mz. This last was equipped with the fast field cycling (FFC) sequences based on a pre-polarized initial condition which was helpful to collect the very low frequency data (0.01-3.7 MHz). The technical details of the instrumentation are reported in appendix C.

All the sample were dispersed in organic solvent, i.e. octadecene, whose self diffusion coefficient (D) is not present in the literature nor in the solvent specifications. In order to fix the D value during the fit procedure the coefficient was measured ($D=2.5\times10^{-10}$ m^2/s) by an NMR spectrometer working at 400MHz, the experiment is resumed in Appendix A.

Figure 5 and 6 show the experimental data of hollow and full samples respectively.

In order to favor the comparison on the relaxation efficiency of different samples, the experimental data were normalized on the iron concentration, taking into account also the solvent relaxation time. In particular, the y-axes of figure 5 and 6 refer to a quantity called relaxivity which is defined as the effective nuclear relaxation efficiency of the protons of the solvent containing the nanoparticles by the formula:

$$r_i = \frac{\frac{1}{T_{i,sol+NP}} - \frac{1}{T_{i,sol}}}{[Fe]}$$

where i=1,2 .

The iron concentration of the sample was evaluated by an external industry's laboratory (i.e. S.P.S. Ecologia, Italy); the results are listed in Appendix B.

It is important to note that the longitudinal (i=1) and transverse (i=2) relaxivities contain different informations on the spin dynamics being associated to different interactions (see 2.II.i). Moreover it has to remarked that the transversal relaxivity r_2 is directy proportional to the contrast efficiency of the nanoparticles when used as negative contrast agents in magnetic resonance imaging (MRI). In this sense the value of r_2 at the frequency used in MRI clinical apparatuses (0.2, 1, 1.5 and 3T, mostly) is an important parameter for the possible biomedical application of the hollow systems.

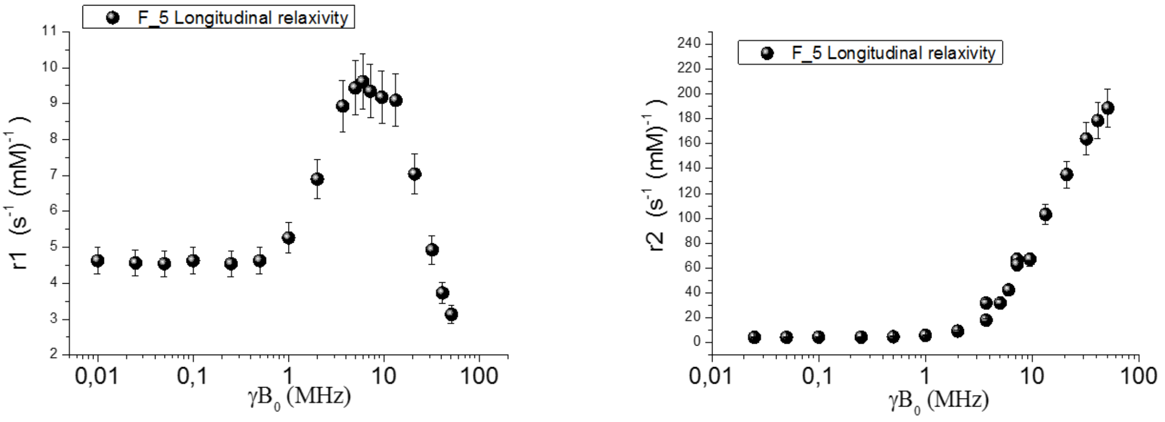

(a) (b)

Figure 5 Longitudinal (a) and transversal (b) relaxivity experimental data of the full nanoparticles used as reference (since it has been synthesized with the same synthesis procedure of the hollows, only F_5 was chosen as reference)

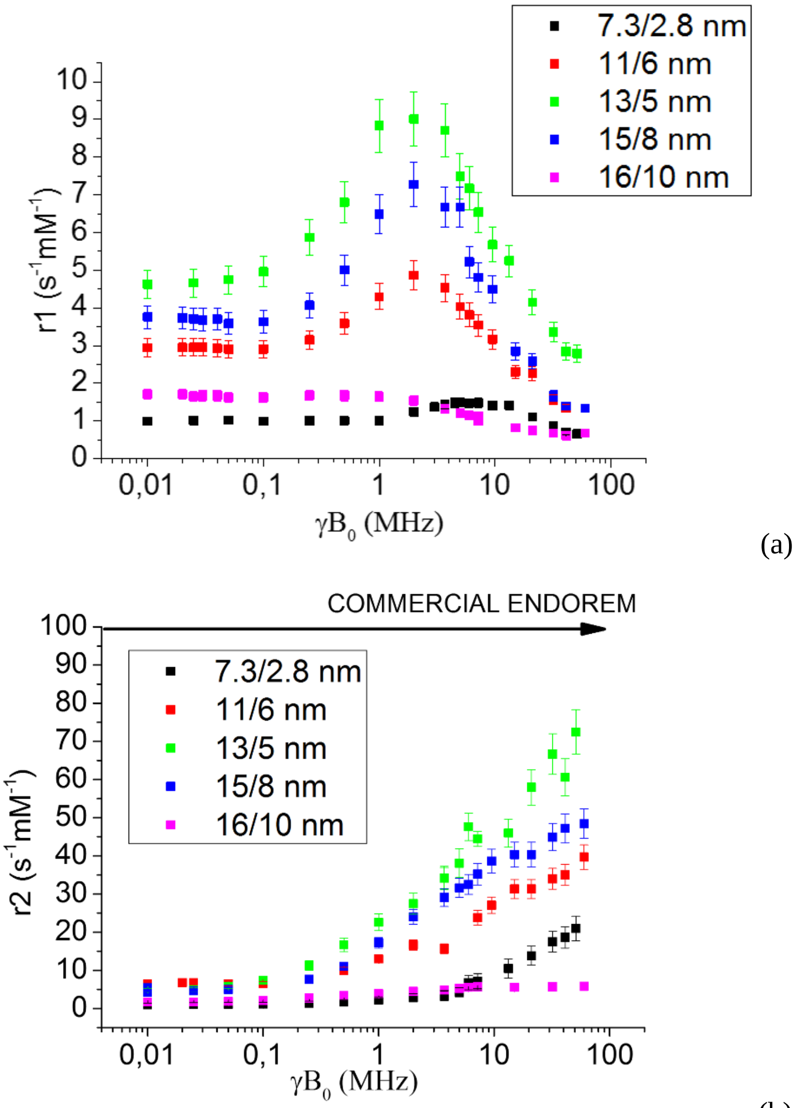

Figure 6 Longitudinal (a) and transversal (b) relaxivity experimental data of the hollow investigated samples

A preliminary analysis of the experimental data of both full and hollow samples leads to the following considerations:

- The relaxation efficiency of the hollow nanoparticles is not proportional to the magnetic volume (refer to the sample's name in the legend which are ordered by increasing volume) as expected by the theory which was validated for the full samples by several literature data [79].
- The maximum of the longitudinal relaxation (r_1) of the hollows seems to shift towards lower frequency when the hydrodynamic external radius (d) increases even if the shift is smaller than the one predicted by Roch et al. and previously measured on full samples [79].
- By comparing the relaxivity data of figure 5(a) and figure 6(a) one can notice a high field contribution to r_1 of the hollows which is not present in the full samples.
- The value of the transversal relaxivity (r_2) of the hollows at high field almost reaches the commercial ENDOREM commonly used in hospital as MRI contrast agents.
- Both full and hollow samples present a r_1 comparable to r_2 at low field, as predicted by Roch's theory of superparamagnetic relaxation.

Data analysis

In figure 8 the fitting curves of the longitudinal relaxation of the full samples experimental data, are represented in red color. As can be noticed the Roch heuristic model of r_1 succeeds in reproducing the dispersion curves of the full (F) nanoparticles. On the other hand figure 9 shows the experimental data of the hollow (H) samples that noticeably disagree from the red fit curves in particular in the high field range.

The above considerations induce us to consider an additional contribution to the relaxation present in the H samples. Following the path lightened by the DC magnetic measurements we propose here a novel approach which would be able to fit the longitudinal NMR-D profiles of hollow nanoparticle samples. The proposed phenomenological model is basically the linear combination of a PM relaxation (see equation 6) and a SPM relaxation (Roch's heuristic model), the first ascribed to the surface disordered spin layer much more important in the H sanples with respect to the F ones. The weight of the PM component has been fixed to the weight of the lower blocking temperature distribution function as calculated from the DC ZFC/FC measurements (i.e. A_{surf}^{DC}, see chapter 2) and ascribed to the surface spins. This is actually a rough estimation, as DC magnetometry is indeed a bulk technique, sensitive to an average answer of the sample, while NMR is a local probe sensitive to the closest spin dynamics to the local probe (^{1}H). In this sense we expect that the outer surface of the H particle would contribute more to the PM relaxation with respect to the inner surface.

The fitting function we used is therefore:

$$\frac{1}{{T_1}^{SPM+PM}} = (1 - A_{surf}^{DC})\frac{1}{{T_1}^{SPM,heu}} + A_{surf}^{DC}\chi T\tilde{A}\frac{\tau_c}{1+\omega^2\tau_c^2}$$

(11)

The paramagnetic contribution to the correlation time τ_c was estimated assuming a non interacting Arrhenius model for the paramagnetic Neél reversal $\tau_S = \tau_0 e^{\frac{\Delta}{k_B T}}$ with $\tau_0 = 10^{-11}s$, which is the typical attempt time for PMs [90-93] and $\Delta = E_{B,SURF}^{DC}$ is the anisotropy barrier that we fixed as the value calculated from the DC analysis in Chapter 2 (see table 4 Chapter 2).

The analysis of the proton NMR-D profiles with (11) gives us :

(i) The average *magnetic volume V_{NMR}* partecipating to the superparamagnetic relaxation seen from NMR relaxometry.

(ii)The average distance of minimum approach of the proton to the center of the nanoparticles (i.e. *d*)

(iii) The *Neèl magnetization reversal* time of the superparamagnetic electron spins (i.e. ${\tau_N}^{SPM}$)

(iv) The *hyperfine coupling* between the nuclei and the PM surface spins $\chi T\tilde{A}$.

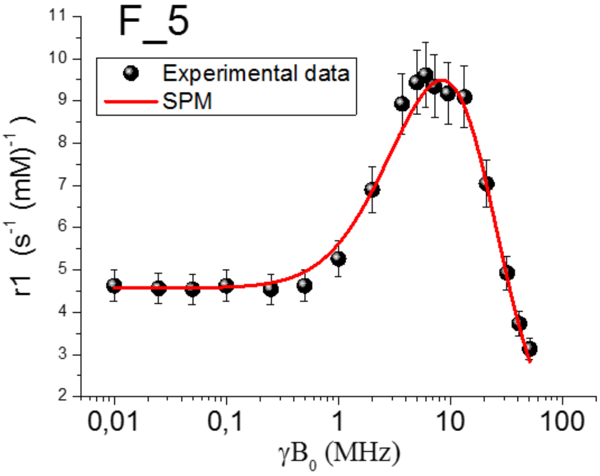

Figure 7 Fitting curve of the longitudinal NMR-D of full nanoparticles. The red lines represent the best fit result with Roch's euristic model

The blue lines of figure 8 represent the fit lines which include the PM contribution tentatively ascribed to a paramagnetic component corresponding to disordered surface spins. The agreement with the experimental data significantly increases, not only in the high field region but also in the dispersion at low field and at the maximum position. As the saturation magnetization is a fixed parameter in equation (11), we can assume that the maximum position is mainly related to the distance of minimum approach of the proton of the solvent to the center of the nanoparticles (see figure 5). On the other hand the better agreement at high field is ascribed to the PM component.

To interpret the fitting results one has to refer to table 1 which contains the informations extracted from the NMR analysis.

Column 1 and 2 of the table list the parameters related to the SPM contribution such as the volume of the superparamagnetic material (i.e. V_{NMR}) and the Neél reversal time (i.e. $\tau_N{}^{SPM}$) as seen by NMR. It is worth to notice that (a) V_{NMR} is less than the actual V corrisponding to the total magnetic volume thus indicating that only a percentage of the totality of the spins are in a SPM state and (b) the Neél time is in the typical range of superparamagnetic materials.

Column 3 of the table list a parameter related to the PM contribution, i.e. the hyperfine coupling $HF = \chi T\tilde{A}$ which is in the range of paramagnetic substances previously studied in literature [90-93]. It is worth to notice that the value of HF is directly proportional to the volume of the outer thick disordered layer as shown in figure 10. This is not surprising if one considers that the HF constant is proportional to the inverse of the third power of the distance between the interacting components (i.e the ^{1}H and the PM spins). In particular since $0.35 < r_{out}/r_{in} < 0.65$ we expect the hyperfine coupling with the outer surface spins to be 4 times higher than the hyperfine coupling with the inner surface spins ($4 < HF_{out}/HF_{in} < 23$).

Column 4 of table 1 represent the average minimum approach distance of the water molecules with respect to the center of the nanoparticle d. Assuming 2nm for the dimension of the oleic acid molecules which compose the coating, all the d values are in the expected range and indicate that the coating is not penetrated by the solvent. It is important to note that even if $\tau_D = {d^2}/{D}$ is present in both PM and SPM relaxation function, its contribution to the paramagnetic correlation time τ_C is almost negligible, because the frequency $\frac{1}{\tau_D}$ is three orders of magnitude lower than $\frac{1}{\tau_S}$. The same cannot be assumed for the contribution of the diffusion to the SPM correlation time being $\frac{1}{\tau_D}$ almost comparable to $\frac{1}{\tau_N{}^{SPM}}$. For these reason we can conclude that the value of d principally refers to the "core spins".

Column 5 of table 4 represents the volume fraction of spins in the SPM state as seen from NMR: the values are in close agreement with the SPM% calculated from the M(H) at room temperature in table 4, Chapter 2.

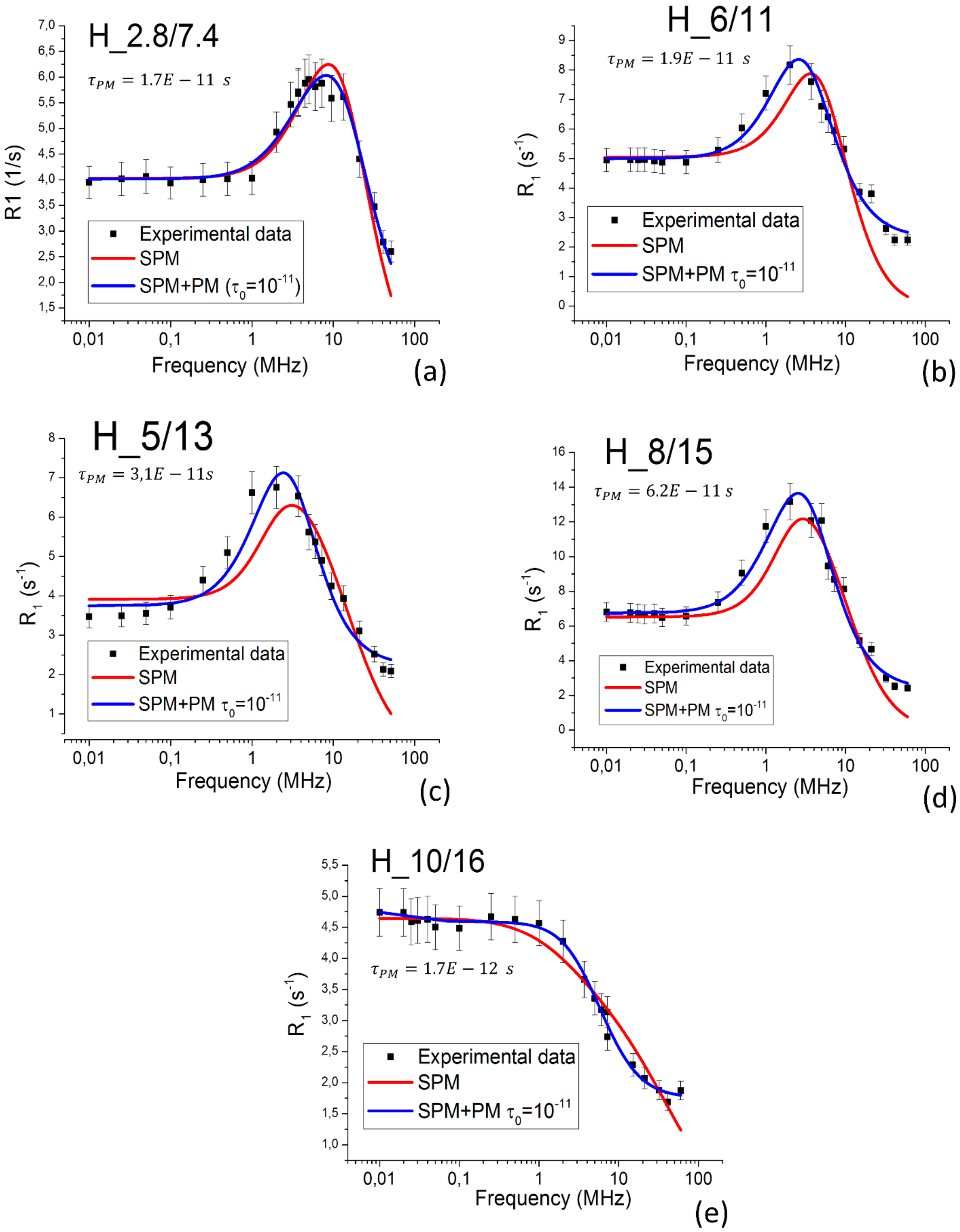

Figure 8 Fitting curves of the longitudinal NMR-D data of hollow nanoparticles. The red lines represent the best fit result with Roch's heuristic model and the blue lines represent the best fit results with eq (11).

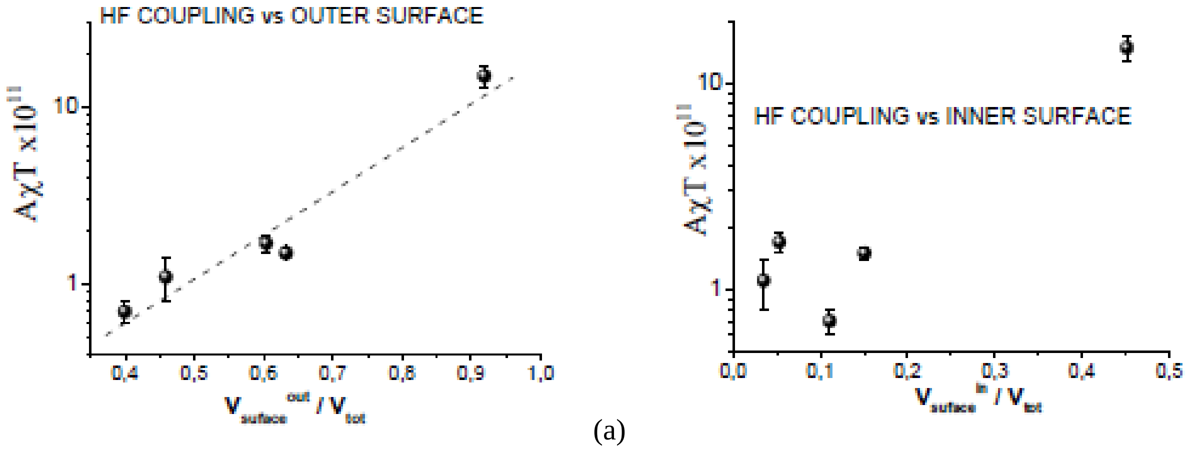

(a) (b)

Figure 9 Dependence of the HF coupling from the volume of the (a) outer and (b) inner disordered layer in the hollow samples.

SAMPLE	***V_{NMR} (nm^3)***	$\tau_N{}^{SPM}(s)$	**HF^{PM} (1/s^2)**	***d (nm)***	***SPM***
F_5	65± 2	(3.7 ±0.6) 10^{-10}	-	8 ± 2	95%
H_2.8/7.4	165 ± 4	(8.5 ±0.7) 10^{-10}	(1.1±0,3) 10^{11}	7.7 ± 0.3	82%
H_6/11	268 ± 7	(4.6 ±2.0) 10^{-9}	(1.7±0.2) 10^{11}	8 ± 6	40%
H_5/13	860 ± 9	(2.4 ±3.0) 10^{-9}	(0.7±0.1) 10^{11}	11 ± 4	66%
H_8/15	697 ± 7	(2.3 ±1.5) 10^{-9}	(1.5±0.1) 10^{11}	12 ± 5	78%
H_10/16	45 ± 10	(5.2 ±3.0) 10^{-8}	(1.5±0.2) 10^{12}	7 ± 4	4%

Table 1 List of the parameters calculated from the fitting of the longitudinal NMRD curves by Roch's model (Full sample) and by eq. (11) (hollow samples).

Some of our previous works [74,94] revealed that the r_2 Roch's model fails to describe the transversal relaxivity, even on full nanoparticles samples. In particular the experimental data show some discrepancies with the theoretical ones obtained by using the same fit parameters values extracted from the r_1 fitting: it should be noted that the r_2 theoretical curves do not reproduce the experimental data in the high field region, being lower than experimental ones. We suggest that one or more unknown physical mechanisms (i.e. interaction between MNPs, chemical exchange with the water molecule of the bulk, dipole-dipole nuclear interaction, etc), not included in the Roch's model, contribute to r_2 in the high field regime.

To further test the validity of the model we proposed in equation 11, we simulated the r_2 curves of hollows nanoparticles by using the same parameters found in the r_1 analysis as discussed above.

In particular the SPM+PM model presented in equation 11 can be extended to the transversal relaxation if one consider that $1/T_1 \propto J(\omega_L)$ and $1/T_2 \propto J(\omega_L = 0)$ where J is the electronic spectral density and ω_L is the nuclear Larmor precession. Thus, one can tentatively model the transversal relaxation (i.e. $1/T_2$) by setting $\omega_L = 0$ in the $1/T_1$ expression (equation 11), obtaining

$$\frac{1}{{T_2}^{SPM+PM}} = (1 - A^{DC}_{surf})\frac{1}{{T_2}^{SPM,heu}} + A^{DC}_{surf}\chi T\tilde{A}\tau_c$$

(12)

Figure 11 shows in blue the simulated r_2 curves of H_5/14 and H_6/11 which are in quite strong disagreement with the experimental data, especially in the high field region. Moreover the simulation fails also to describe the low-intermediate part of the dispersion curve which surprisingly presents a “concave dispersion” never observed before in the full samples.

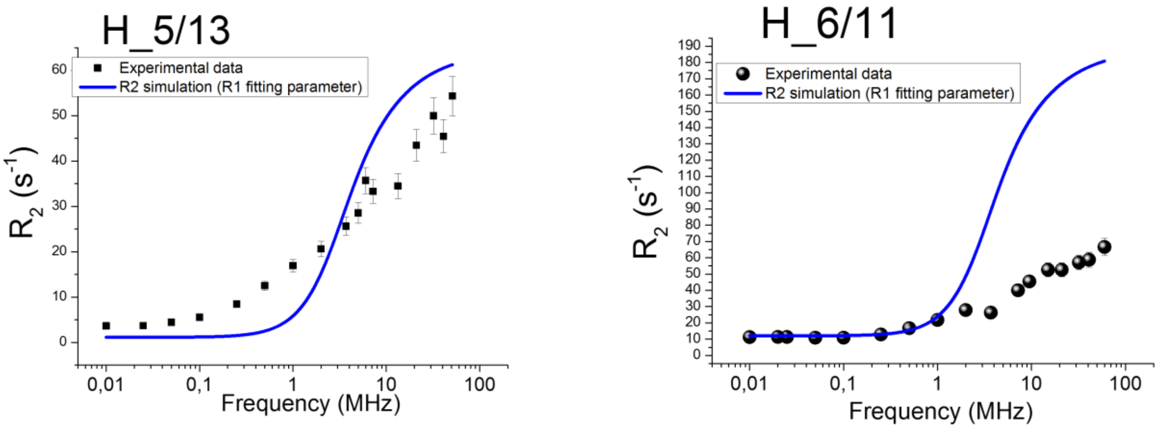

Figure 10 The violet lines are the r_2 calculation performed using Eq. (12) and the fit parameters listed in table 1(the same obtained for r_1).

In figure 11 we want to underline the previous observation regarding the evidence of a bump in r_2 at middle-low fields, by showing the r_2/r_1 ratio of the hollows with respect to the full F_5 sample.

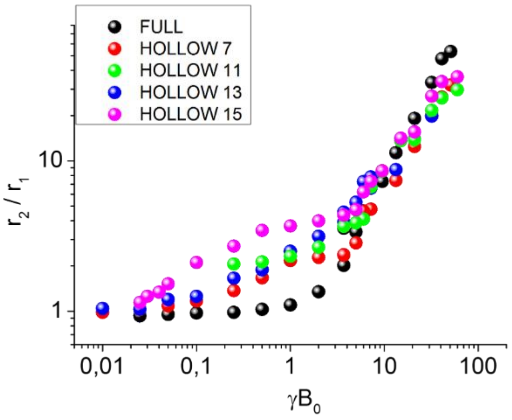

Figure 11 Transversal to longitudinal relaxivity ratio. The hollows present a contribution in the middle field region which is not visible in the full particles we used as a reference.

II.iv Conclusion

We presented the first NMR-D experimental curves on the magnetic nanoparticles with a hollow topology. The existing models fail to describe both the longitudinal and the transverse nuclear relaxation induced by these systems.

We proposed a phenomenological model through which we were able to fit the NMR-D r_1 curves of hollow nanoparticles while Roch’s heuristc model fails. The proposed model takes into account a PM contribution to the relaxation. It is important to note that the presence of a PM contribution first observed in DC magnetometry (see chapter 2) is here confirmed. The weight of the PM function was indeed fixed from DC magnetometry which is a bulk technique that return the average suface contribution to the magnetization. NMR instead, being a local technique, is expected to return a different weight of the closest set of PM spin population (i.e. the outer surface one). As perspective the proposed model has to be further improved, in particular the contribution of inner and outer surface has to be evaluated and decoupled.

Nevertheless the HF PM coupling and the SPM Neél time were evaluated and found in the expected range [90-93] , [74-96] thus confirming the physical mechanisms beyond the nuclear relaxation.

The transversal relaxation experimental data are still not reproducible by any of the existing models, nor by ours. In particular the origin of a high field contribution and an intermediate field bump have to be clarified.

III. MuSR spectroscopy

MuSR (Muon Spin Resonance) spectroscopy has a familiarity with other local resonance spectroscopies such as NMR and EPR which take nuclei and electron as local probes. As ^{1}H nuclei and unpaired electrons, also the muons own spin ½ but act as local probe with a complementary window frequency (10^5-10^8 Hz) with respect to the one of the nuclei (10^6-10^9 Hz, although with FFC-NMR it is possible to arrive to 10^4 Hz, as seen) and the electrons (10^9-10^{11} Hz). In figure 13 the dependence of the Larmor precession frequency accessed by the three techniques as a fucntion of the applied magnetic field, is shown.

Actually one has to consider the advantage of the MuSR technique being the muons completely polarized when they reach the sample so that there is no need to apply a static field as in NMR and EPR.

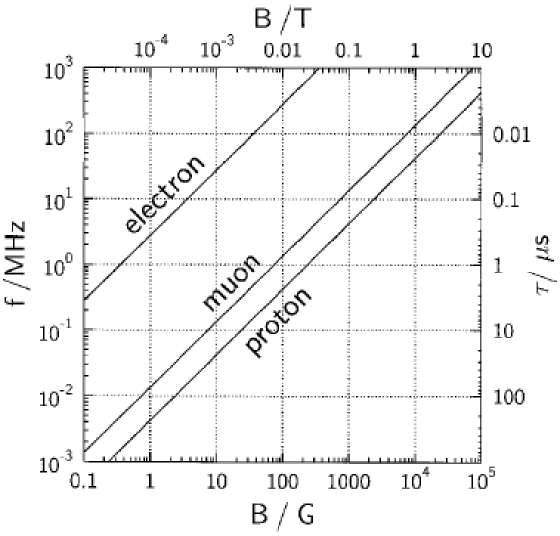

Figure 12 The Larmor precession frequency f in MHz (and the corrisponding period $\tau = 1/f$) for the electron, muon and proton as a function of applied magnetic field B.

III.i Muons as local probe

The muon is a lepton and its properties are listed in Table 2 in comparison with other leptons such as the electron and the proton. In particular it has spin ½ , gyromagnetic ratio 135.54 MHz/T, it is lighter than the proton and has a lifetime of 2.2 μs.

The muon decay limits the observation time at about 10 lifetime, a long time scale compared with that of the thermalization of the implanted muons in the sample which may vary from *ns* in gas to *ps* in condensed phase. For these reasons it can be said that the muons reach their ground state promptly on implantation. By state is meant the chemical environment and it has not to be confused with the *spin state*, whose evolution provides the primary source of information in μSR experiments. The 2.2μs timescale is quite adequate to follow this evolution and to determine the precession frequency or the *relaxation rate* over a wide range. In fact it sets a “window” on the time scale of dynamical phenomena bridging the gaps between those accessible to other techniques.

The detection of individual particles gives to the μSR a remarkable selectivity and sensitivity. The attention is focused on the muon alone, and its spin transitions (a Larmor frequency of 1MHz correspond to an energy quantum of the order of 10^{-8} eV) are, in effect, detected at the energy of the muon decay (up to 50 MeV) and spectra are obtained with a statistics of millions recorded muon decays, depending on the strength of the signal.

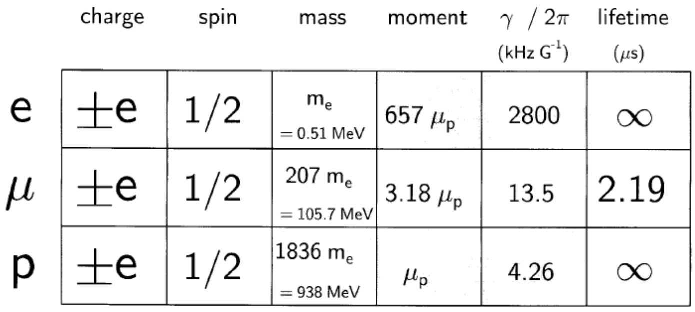

	charge	spin	mass	moment	γ / 2π (kHz G^{-1})	lifetime (μs)
e	$\pm$e	1/2	m_e = 0.51 MeV	657 μ_p	2800	∞
μ	$\pm$e	1/2	207 m_e = 105.7 MeV	3.18 μ_p	13.5	2.19
p	$\pm$e	1/2	1836 m_e = 938 MeV	μ_p	4.26	∞

Table [2] List of the main physical properties of electrons, muons and protons [95].

In order to produce intense muon beams suitable for implantation, the decay of charged pions is exploited. Since negative muons in matter are strongly attracted by nuclei their fate often tells more about the nuclear interactions in the sample than about its solid state properties. For this reason is better to use positive muons. In the rest frame of the pion, which decays according to:

$$\pi^+ \rightarrow \bar{\mu}^+ + \nu$$

the outgoing muon and neutrino have opposite linear momentum equal to 29.79 MeV/c.

Muon spin polarization

The role of violation of parity in yielding spin polarized muon beams can be directly identified in the rest frame of the pion. The pion π^+ is a spinless particle; instead the neutrino has spin one half, like muon, and the angular momenta of the two particles must come out opposite one each other, due to angular momenta conservation. Futhermore, since the neutrino is highly relativistic, its spin would be aligned with its linear momentum. The violation of parity in this event is equivalent to state that only neutrinos of negative helicity (spin antiparallel to linear momentum) exist. This is often simplified by saying that, although in the macroscopic world the mirror image of any possible events is also a possible event, this symmetry is broken in the microscopic realm of elementary particles. The conservation of angular momentum imposes that also the muon from the decay must have negative helicity (see figure 13). Therefore if we select by transport a very small solid angle of directions diverging from the primary target, and a momentum of exactly 29.79 MeV, the beam will be predominantly of muons from the decays of pions at rest on the surface of the target, nearly 100% spin-polarized backwards with respect to linear momentum.

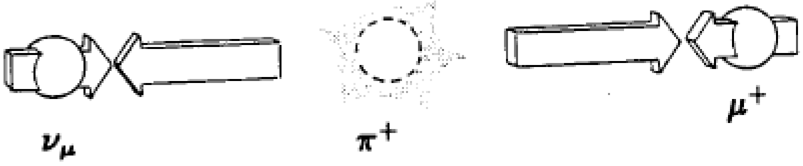

Figura 13 Pion decays in a muon and a muon neutrino.

Muon sites of implantation

Muons implant in the minima of the electric potential and quite often the muon's fate is not unique. A number of distinct final states may be obtained, with different probabilities. Different sites can correspond to (i) distinct intersitial sites due to alternative chemical bonds or (ii) different electronic configurations. Note that muon locations may be further differentiated in a magnetic material if the direction of the ordered electrons magnetic moments produces different dipolar fields at otherwise equivalent sites. The multiple sites are effectively accounted for by considering that the total asymmetry A of the full implanted muon ensemble is divided into the partial asimmetries of the *n* distinct muon sites according to

$$A(t) = \sum_{j=1}^{N} A_j(t)$$

where the initial partial asimmetry $A_j(0) = Ap_j$ may be written in terms of the stopping probability p_j at the j-th site (with $\sum_j p_j = 1$).

Muon interactions

Muon comes to rest inside the sample and, in most cases, this happens without loss of spin polarization. The initial energy of the muon, of the order of 4 MeV, is huge compared to the typical energy of electrons (from few eV for valence shells, to hundredths keV for inner shells and heavy elements). Therefore the initial collisions lead to ionization (Coulomb scattering) and in this process the muons leave behind a wake of ions and electrons.

When below the ionization threshold, the muon travels quite a long way away from this region and the final thermalization depends on solid state or chemical details of the environment . The positive muon can be regarded as a ^{1}H: in organic compounds (full of cation vacancies) it can replace an atom of the host compound , a Mu-H exchange could take place or, more often, in crystals the muon ends up at intertistial sites which correspond to the minima of the electric potential (see previous paragraph). At each interstitial site the muon spin I=1/2 is subjected to interactions with the other spins, those of neighbouring electrons and nuclei. A classification of these interactions similar to that of NMR may be performed, with the simplifying condition that the muon itself, being spin 1/2, does not possess any electric field quadrupole moment. Hence the muon spin does not couple to the electric field gradient, although it may produce one.

Assuming that an uniform external magnetic field B will be applied along z, we may write:

$$\frac{H}{h} = \frac{1}{2\pi}\left\{\left[-\gamma_\mu I_z + \gamma_e \sum_{i=1}^{n_e} s_{iz} - \sum_{k=1}^{n_n} \gamma_k I_{kz}\right] B + \gamma_\mu \boldsymbol{I} \cdot \sum_{i=1}^{n_e} \hbar\gamma_e \left[\frac{\boldsymbol{l}_i}{r_i^3} + \frac{-\boldsymbol{s}_i + 3\widehat{r_i}(\boldsymbol{s}_i \cdot \widehat{r_i})}{r_i^3} + \frac{8\pi}{3}\boldsymbol{s}_i \delta(\boldsymbol{r}_i)\right] \right.$$
$$\left. + \gamma_\mu \boldsymbol{I} \cdot \sum_{k=1}^{n_n} \hbar\gamma_k \frac{-\boldsymbol{I}_k + 3\widehat{r_k}(\boldsymbol{I}_k \cdot \widehat{r_k})}{r_k^3}\right\}$$

(13)

where: *(i)* the first term contains the Zeeman interactions of all the involved spins ($\boldsymbol{s}_i$ for the i-th electron and $\boldsymbol{I}_k$for the k-th nuclei); *(ii)* the second term contains the magnetic interaction between the muon and the electrons : it contains an orbital momentum $\boldsymbol{l}_i$ term often neglected in crystals, a dipolar field typically created by distant magnetic ions (dipolar hyperfine tensorial coupling) and a contribution $\boldsymbol{s}_i\delta(\boldsymbol{r}_i)$ due to the overlap of the muon and i-th electron's wavefunction (Fermi contact hyperfine scalar coupling); *(iii)* The third term of equation (13) contains the magnetic interaction between the muon and the nuclei (due to the nuclear dipolar field created by nuclear point dipoles).

The main subject of this thesis drives the attention to the second term, since it can describe the interaction between muons and electrons in magnetic materials.

Parity violation in the muon decay

Parity violation is also the key to the detection of the muon spin evolution in time. As discussed in the previous paragraph, when the muon stops into matter it quickly interacts, thermalizes and after short time (2.2μs) it decays into a positron and two neutrinos:

$$\bar{\mu}^{+} \rightarrow e^{+} + \nu_e + \bar{\nu_e}$$

(14)

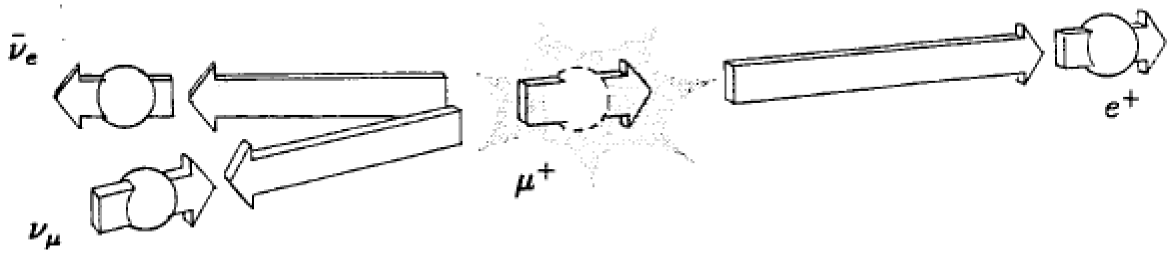

Figure 14 Muon decay in a positron and a muon neutrino and a muon antineutrino

Since equation (14) represents a three body decay, there is a continuum of possible geometries, and correspondingly, a range of energy of the emitted positron ($E \leq 52.83\, MeV$). The correlation imposed on the directions of the muon spin and of the positron momentum allows the experimental determination of the muon spin direction from the identification of the positron momentum direction. The correlation is simple at maximum positron energy (which corresponds to the two neutrinos being both emitted opposite to the positron) but is reduced for lower energies. More precisely, the probability distribution function for the positron emission is correlated to the instantaneous direction of the muon spin by the formula:

$$P(\theta) \propto 1 + A(E)cos\theta$$

where $A(E)$ is the asymmetry factor that depends on the energy of the emitted positro, equal to 1 if $E = E_{max}$.

The distribution vs. both angle and energy is given in terms of $x = \frac{E}{E_{max}}$

$$W(x,\theta) = \frac{E(x)}{4\pi}[1 + A(x)cos\theta]$$

with $E(x) = 2x^2(3 - 2x)$ and $A(x) = (2x - 1)/(3 - 2x)$. The polar plot in figure 15 shows the probability distribution lobe for the maximum asimmetry A=1 (a), and for the average asimmetry A=1/3 (b) : the probability in each direction is proportional to the length of the segment along the same direction.

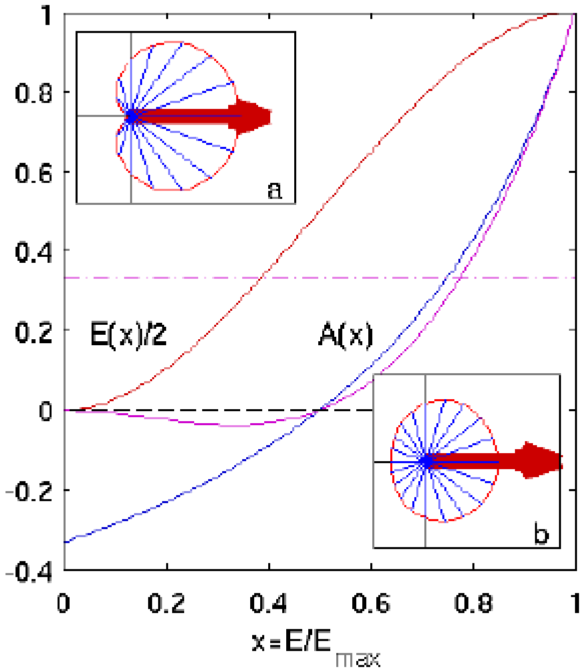

Figura 15 Energy spectrum E and asymmetry spectrum A vs reduced energy x = E/Emax. The top inset (a) shows the polar plot of the emission probability at the maximum asymmetry A=1. The bottom inset (b) shows the polar plot of the emission probability at average asymmetry A=1/3 that is ideally observed if all positron are detected.

Muons in magnetic ordered materials

Since the muon spin preceeds around any local magnetic field which it feels in matter, the spin dynamics of the thermalized muon depends dramatically on whether it ends up in a coherent (i.e. paramagnetic, diamagnetic or magnetic ordered environment) or in an incoherent (i.e. disordered state above the magnetic ordering temperature of a magnetic material) spin states. When the muon is localized interstitially in a magnetic ordered material it experiences hyperfine (mainly dipolar) coupling to the ordered magnetic moments of the electron. For this reason muons are ideally suited to study problems in magnetism. As discussed before, implanted muons spins in magnetically ordered materials precess in the internal magnetic field and directly yield signals proportional to that magnetic field. In this respect the muon spin behaves as a microscopic magnetometer. The very large magnetic moment of the muon makes it very sensitive to extremely small magnetic field (down to~ 10^{5} T) and thus is very useful in studying small moment magnetism. It is also valuable in studying materials where the magnetic order is random or of very short range. Since muons stop uniformly throughout a sample, each signal appears in the experimental spectrum with a strength proportional to its volume fraction, and thus the technique is helpful in cases where samples may be multiphase or incompletely ordered.

Let us assume that the ordered moments $\hbar\gamma_e\boldsymbol{S}$ are directed along a single crystallographic direction. This can be the case of a unixial ferromagnet/antiferromagnet in zero applied field. The local field at the muon site is due to a spin Hamiltonian of the type described in equation (13) as

$$\frac{H}{h} = \frac{\gamma_\mu}{2\pi}\boldsymbol{I}\cdot\left[\frac{\mu_0}{4\pi}\hbar\gamma_e\sum_i\frac{3\hat{r_i}(\boldsymbol{S}_i\cdot\hat{r_i})-\boldsymbol{S}_i}{r_i^3}+(\delta\tilde{A}+A_0)\cdot\boldsymbol{S}\right]$$

(15)

Where the electronic term in square brackets acts as an effective magnetic field $\mathbf{B}_\mu$ on the muon. It is important to note that $\mathbf{B}_\mu$ in not necessary parallel to **S,** due to the tensorial character of the dipolar and pseudo-dipolar interaction which justifies that crystallographically equivalent sites in the unit cell might experience different local fields. This has important consequences both for the amplitude of muon precessions in an oriented single crystal and for the vector composition of the local field with externally applied magnetic field (see the experimental section).

Muon longitudinal and transverse relaxation : T_1 and T_2

Muon polarization is the observable in all MuSR experiments, monitored by the asymmetry in the muon decay. A magnetic field does not need to be applied for the muons to precess if the sample has its own magnetic field. Nevertheless, experiments with an external applied field applied parallel to the initial polarization can also be performed such that all the muons will be all in the spin-up or in the spin-down state. This is far from equilibrium in which the population of the two states are related by a Boltzman factor which led to a low net polarization except that in high field or low temperature condition. The muon polarization should therefore decay relaxing essentially to zero. This is known as spin-lattice (or longitudinal) relaxation. In a static longitudinal field each muon is in a stationary state and can face a transition only if it experiences some time-dependent perturbation which contains frequency components at its Larmor frequency . This can be caused for example by fluctuation of the local fields. The dacay of the polarization is described by a relaxation function G(t) such that:

$$P(T) = P_0G(t)$$

If the local magnetic field at the muon site is at an angle θ with respect to the initial muon-spin direction, the muon spin will subsequently precess around the end of a cone of semi-angle θ about the magnetic field.The normalized decay positron asymmetry will be given by

$$G(t) = cos^2\vartheta + sin^2\vartheta\ cos\left(\gamma_\mu Bt\right)$$

(16)

If the direction of the local magnetic field is entirely random, then averaging over all directions would yield

$$G(t) = \frac{1}{3} + \frac{2}{3}cos\left(\gamma_\mu Bt\right)$$

(17)

If the strength of the local magnetic field follows from a Gaussian distribution, then a straightforward averaging over this distribution gives

$$G(t) = \frac{1}{3} + \frac{2}{3}exp(-\Delta^2t^2/2)(1-\Delta^2t^2)$$

(18)

a result which was first obtained by Kubo and Toyabe in (1967) as an entirely theoretical exercise. This relaxation function is illustrated in figure 16. Its field-dependence is indicated schematically in figure16(b) which shows a number of curves of equation (18) for different values of the internal field *B* . Initially all curves do roughly the same thing (i.e. fall from 1 to a minimum value and then increase) but after a short time they dephase with respect to each other. Hence their average, the Kubo and Toyabe relaxation function, would be expected to fall from unity to a minimum and then recover to an average value, one-third (in zero-field).

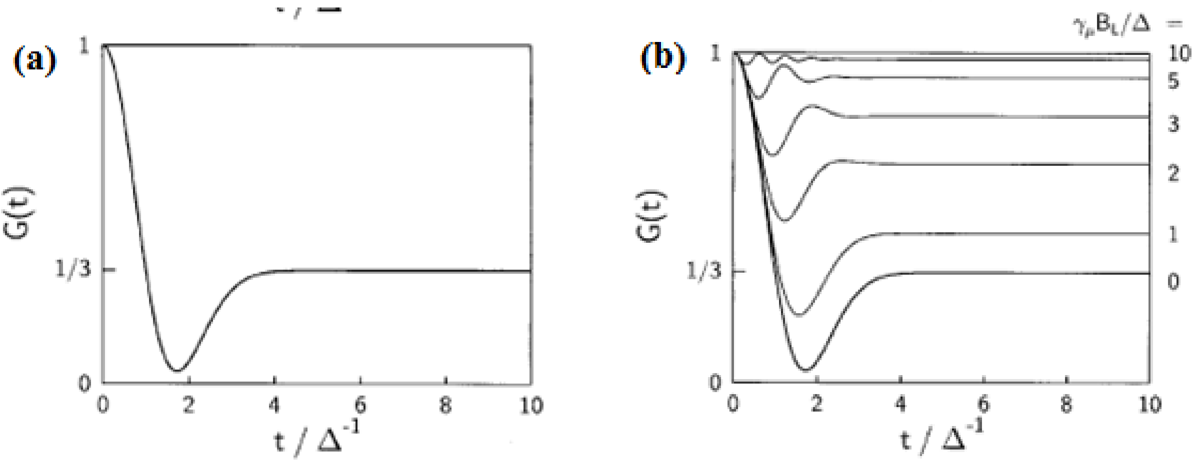

Figure 16 The Kubo-Toyabe relaxation function rapresented by equation (18) (a), and its shape dependency to an esternal applied field (b).

If the implanted muons experience an almost uniform static internal field in the sample, but there is a slight variation from site to site, different muons will precess at slightly different frequencies and become progressively dephased so that the oscillations in the data will be damped (see the transversal relaxation in NMR experiments). If the field is much higher than the local field didtribution the damping could be so large that no oscillations can be observed. However this effect could also be caused either by rapid fluctuations either of the internal field, by some intrinsic property of the sample, by fluctuation of the muon’ s position, muon diffusion.

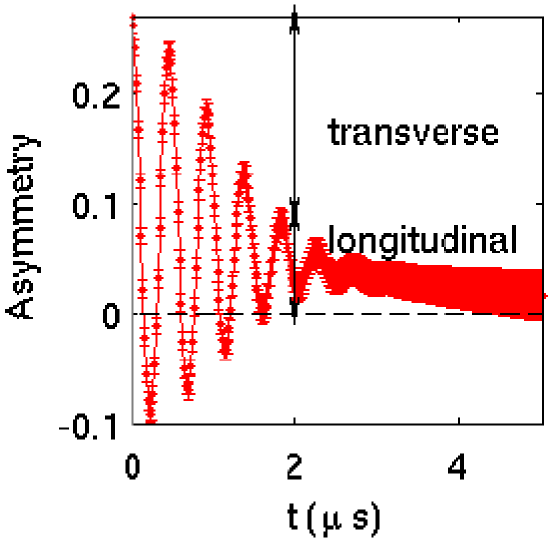

Figure 17 Powder average of the signal from a single muon site in a magnetically ordered material. The total asymmetry A=0.27 is subdivided into two thirds precessing and decayng time and one third decayng at slower rate.

III.ii Experimental Section

Experimental data

The μ^+SR experiments were performed on the GPS beamline of the Swiss Muon Source at the Paul Scherrer Institute (PSI), Villigen (CH). In such experiments, a 100% spin-polarized positive muons beam is addressed to the sample. As discussed before, the muons implant in sites corresponding to a minimum for the electric potential of the system and their spins can precess around any magnetic field that is not parallel to their initial polarization direction (precession in transverse field). Furthermore, the muons lose their polarization through spin-lattice and spin-spin relaxation processes due to the interaction with the local hyperfine magnetic fields (longitudinal and transverse relaxation). If a longitudinal magnetic field H_{LF} much greater than the local transverse field (average and fluctuations) is applied, the effect of the transverse dephasing is quenched and the decay of the muon asymmetry A(t) is dominated by the longitudinal relaxation, sensitive to the local magnetic field.
The investigation was performed on two samples : F_5 and H_2.8/7. The choice of the samples was driven by the idea of comparison of full and hollow spheres having similar anisotropy but different spin topology.

As the investigated samples are in powders, we expect that a significant fraction of the muons stops inside the magnetic core of the particles, while a much lower fraction stops in the particle coating (oleic acid). As the number of the electriv potential wells (negative) where the μ^+ tends to implant is high, the total muon asimmetry contains different components, whose polarization relaxation change as a function of temperature, reflecting the different spin dynamical regimes.

The muon asymmetries collected at different temperatures for samples F_5 and H_2.4/7 in a longitudinal field of 150G are shown in figures 18 and 19 for each sample. The muon total asymmetry at t=0 (A_0) and the background signal coming from muons implanted outside the sample (Bckg) were determined in zero field configuration.

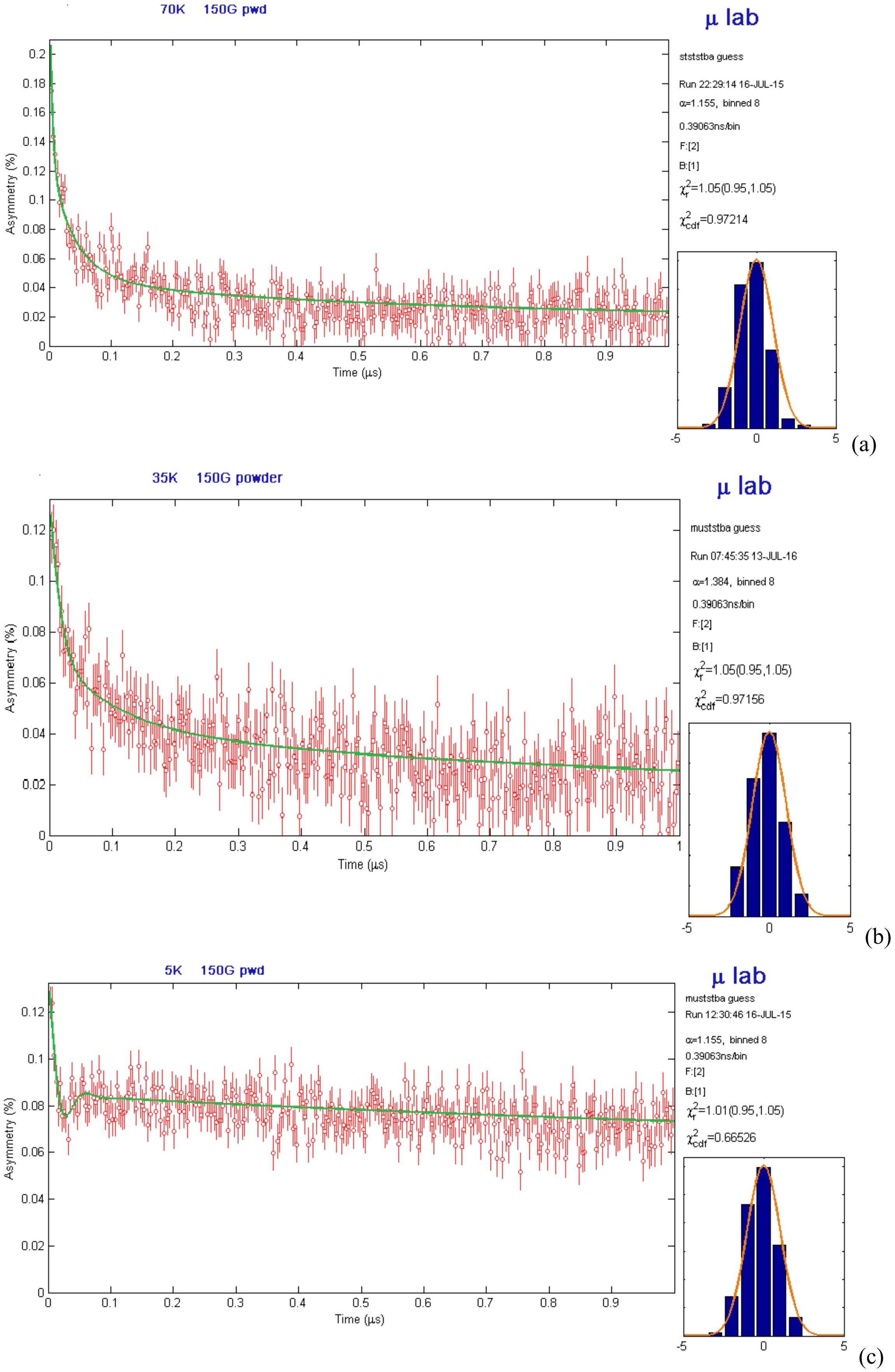

Figure 18 Muon asymmetry data at 150G for F_5: (a) above the critical temperature (T= 70K > T*), (b) around the critical temperature T=35K=T* where the relaxation rates reach its maximum and (c) below the critical temperature (T= 5K < T*) . The best fit curves, obtained as discussed in the text, are also shown in green. The collected statistics was 6 x10^{6} events.

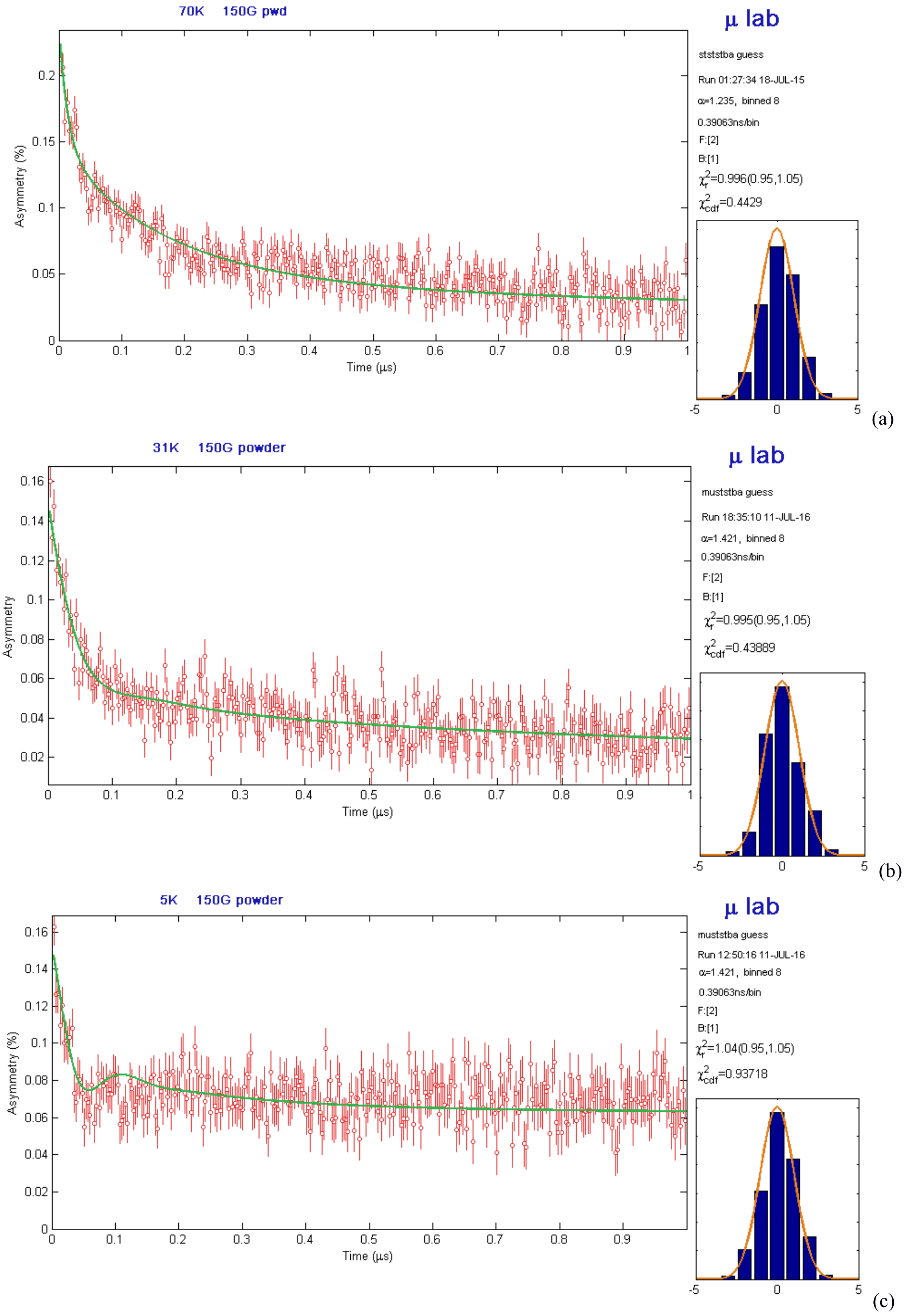

Figure 19 Muon asymmetry data at 150G for H_2.8/7: (a) above the critical temperature (T= 70K > T*), (b) around the critical temperature T=31K=T* where the relaxation ratesreach its maximum and (c) below the critical temperature (T= 5K < T*).The best fit curves, obtained as discussed in the text, are also shown in green. The collected statistics was 6 x10^6 events

From the raw experimental data one can notice that the total asymmetry relaxes faster and faster when the temperature decreases down to a critical value T*, below which a slowing down is observed (see figures 18 and 19 in which the asymmetry for three example temperatures is shown). In fact, as in other frequency-dependent resonance techniques, the capability to exchange enegy between the probe and the investigate system reaches its maximum when the condition $\omega_{\mu}\tau_{c}\sim 1$ is fulfilled, an event that occurs around the experimental temperature T* which we expect to approximate the blocking temperature of the spin system as seen by muons, that from now on will be called $T_B^{\mu+}$.

Data analysis

At high temperature, higher than the blocking temperature seen by muons (i.e. T> $T_B^{\mu+}$) the implanted muons experience a distribution of fluctuating magnetic fields and the muon relaxation in applied longitudinal field can be fitted by means of the function:

$$A(t) = a_1 e^{-\lambda_{Fast} \cdot t} + a_2 e^{-\lambda_{Int} \cdot t} + a_3 e^{-(\lambda_{Slow} \cdot t)^{0.5}} \tag{19}$$

The three components reflect the existence of "at least" three different muon implantation sites with different relaxation rates, i.e. λ_{Fast} (fast relaxation), λ_{Int} (intermediate relaxation) and λ_{Slow} (slow "stretched" relaxation). The weights of the three components were kept fixed in the whole range of investigated temperatures, respectively at a_1 , a_2 and a_3 (where $a_1 + a_2 + a_3 + Bckg = A_0$) whose values are listed in Table 3. Since the amplitude a_i is proportional to the percentage number of implanted muons corresponding to the same minimum values of the electric potential, the assumption of a fixed weights reflects the conservation of the number of equivalent sites (this occurrence for example can be violated in presence of structural phase transitions). Importantly, one should notice that each site corresponding to each a_i is not necessarily a single site but it is more probably a distribution of (dynamically) many almost equivalent sites, as in some cases explicitly witnessed by the presence of the stretched component.

In the above simplified scheme (of implantation sites), the slow relaxing component is (tentatively) ascribed to the muons implanted in (or near to) the particles coating, which experience a smaller local magnetic field, being far from the magnetic ions. The intermediate and the fast relaxing components can be tentatively attributed to muons implanting in the ferrite magnetic core, in different implantation sites corresponding to different minima of the electric potential. We expect that these potential minima are located at different distances from the magnetic centers thus leading to different muon relaxation rates (the fastest component is linked to the implantation site closer to the iron ions).

When the temperature decreases, the system approaches the so-called blocking temperature $T_B^{\mu+}$, at which the muons experience the gradual electron spin blocking. The experimental data show that there exists a temperature T* (of the order of $T_B^{\mu+}$) below which equation (19) is no longer suitable to fit the asymmetry.

The experimental raw data (see figures 17c and 18c) in the temperature range T < T* show that some muons feel a static local field H_{loc} because of the gradual freezing of the nanoparticles (electronic) spins. As a consequence of the high value of H_{loc} inside the magnetic core of the particle, the fast component, corresponding to the muons nearest to the core, presents a high-frequency (higher than the instrument frequency window) precession or very high-relaxation rate, and disappears. For the same reason, i.e. the presence of a local field, the a_2 component (with "intermediate values of relaxation rate") splits in two sub-components (labelled as $a_{2,1}$ and $a_{2,2}$) with a relative weight equal to 2/3 and 1 /3 of a_2, corresponding to the statistically averaged number of muons with polarization perpendicular and parallel to H$_{loc}$, respectively. Indeed, 2/3 of the muons pertaining to the component a_2 have their polarization in transverse direction with respect to the local field H$_{loc}$, that precesses around it. The remaining 1/3 of the muons have a polarization parallel to H$_{loc}$ that relaxes exponentially. Thus, it was possible to fit the total muon asymmetry by means of a three components function:

(20)

$$A(T) = a_{2,1}e^{-\lambda_{Int}\, t} + a_{2,2}\cos(\omega t)e^{-\lambda_{Int}\, t} \quad + a_3 e^{-(\lambda_{Slow} t)^{0.5}}$$

where $\omega = \gamma_\mu H_{loc}$ is the Larmor precession frequency of the muons around the local field H$_{loc}$, being this one a fit parameter. Values of $a_{2,1}$, $a_{2,2}$ and a_3 obtained from the fit are listed in Tab.1; it is worth to notice that $a_{2,1}$ and $a_{2,2}$ are in agreement with the previous consideration being around $1/3a_2$ and $2/3a_2$ respectively.

SAMPLE	T<T*	T>T*
F_5	$a_{2,1} = 0.05$ $a_{2,2} = 0.025$ $a_3 = 0.05$	$a_1 = 0.129$ $a_2 = 0.075$ $a_3 = 0.05$
H_2.8/7	$a_{2,1} = 0.0569$ $a_{2,2} = 0.0284$ $a_3 = 0.0574$	$a_1 = 0.085$ $a_2 = 0.0853$ $a_3 = 0.0574$

Tabel 3 List of the components weights used to fit the muon asymmetries at different temperatures by equations (19) and (20).

It is interesting to compare the value of T* with the temperature of the maximum of the ZFC curves at 150Oe shown in chapter 2. As T* is the experimental temperature at which the total muon asymmetry relaxes faster (i.e. the electronic dynamics at T=T* matches the probe frequency of the muons), T^{ZFC} can be seen as an average temperature at which a percentage of the whole system is blocked and corresponds to the configuration of maximum spin alignment in ZF cooling conditions (i.e. the electronic spin dynamics at T=T^{ZFC} maximizes the probability of alignment to the external field). In particular $T^*_{F\_5}$ = 35 K and $T^*_{H\_2.8/7}$ = 31 K have to be compared with $T^{ZFC}_{F\_5}$= 31 K and $T^{ZFC}_{H\_2.8/7}$ = 29 K respectively. Due to the higher probe frequency of muons, the temperature at which they see the spin dynamics slowing down is higher with respect to the one extracted from DC measuremts.

It is worth to notice that the coherent precession of the muons' polarization corresponding to the component $a_{2,2}$ is observed here for the first time, in literature being reported just cases of Kubo-Toyabe function corresponding to a distribution of local fields and thus of precession frequencies .

The local field behaviour felt by muons H$_{loc}$ = ω/γ$_\mu$ (γ$_\mu$ = muon gyromagnetic ratio) as a function of temperature was extracted and reported in Figure 20 for F_5 and H _2.8/7 samples. At a first approximation, the amplitude of H$_{loc}$(T) is proportional to the order parameter of the blocked state, i.e. the average local magnetization M. Thus, the $H_{loc}(T)$ curve traces M(T). Although the system has zero-dimensionality, a mean field theory generally adopted in the theory of phase transitions, can be tentatively used to describe the theoretical behaviour of M(T):

(21)

$$M(T) \propto H_{loc}(T) = H_{loc}(0)\left(1-\frac{T}{T_c}\right)^{\beta}$$

where β is the critical exponent, M(0) is the residual magnetization at T=0 and T_c is the Curie temperature, for us corresponding to the blocking temperature. The field dependence on temperature was fitted by equation (21); similar values of T_C~35K was found for both samples while different value of β=0.4 and β= 0.2 was found for F_5 snd H_2.8/7.4 respectively, the fit lines being shown in figure 20. It should be remarked however, that the assumption of a mean-field for magnetic nanoparticles, ideally zero-dimensional, is a strong approximation.

The local spin *order* of the system (i.e. H_{loc}) as seen by muons is in agreement with the results obtained from the DC magnetization experimental data which show a lower average order parameter (i.e. macroscopic magnetization) in the hollow sample. In particular, even if H_2.8/7 displays higher volume ($V^{H\_2.4/7}$ = 200 nm^3 and V^{F_5} = 68 nm^3) the value of H_{Loc} experienced by the muons is lower with respect to F_5 so that the evidence of the higher spin disorder in the hollow geometry due to the presence of the inner, outer and inter-crystallites surface, which don't contribute to the local field, is strengthened (see figure 21).

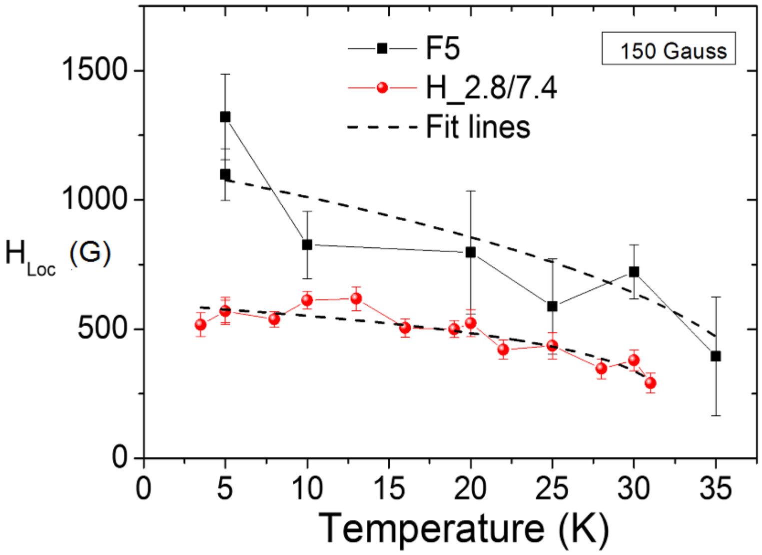

Figure 20 Internal magnetic field (H_{LOC}) values in the F_5 and H_2.8/7 samples. The dashed lines represent the best fit curves obtained with equation (21)

By fitting the muon asymmetry in the whole temperature range by means of equation (19) (for T<T*) and (20) (for T>T*) we obtained the temperature behavior of the muon longitudinal relaxation rates λ_i as a function of temperature. As already underlined in the above discussion concerning muons asymmetries, the behavior of the muon longitudinal relaxation rate as a function of temperature is strongly influenced by the electron spin dynamics of the magnetic nanoparticles. While λ_{Fast} is too fast (>100 μs^{-1}) to obtain values with physical meaning and λ_{Int} changes its form by crossing T_B, the relaxation rate λ_{Slow} can be easily monitored along the whole temperature range (figure 21) through the "eyes" of the muon-electron hyperfine interaction. At first, one should observe that $\lambda_{Slow}(T)$ of F_5 and H_2.8/7 shows an anomaly at $T_c^{F\_5} \sim 50K$ and $T_c^{4F} \sim 40K$ respectively. This anomaly is expected to occur when a critical dynamic behavior (like e.g. an order-disorder phase transition or a spin-freezing effect) sets in, with one or more characteristic correlation frequencies. Indeed, the dynamical response of the muon polarization has a maximum when the Larmor frequency of the muons ω_L matches the electronic correlation time τ_c, i.e. $\omega_L\tau_c \sim 1$.

In our samples, we hypothesized the existence of at least three typical correlation frequencies, reflecting namely the Néel reversal process of the single particle magnetization (corresponding to a frequency $1/\tau_N = \omega_N/2\pi$), the surface spins motion ($1/\tau_s = \omega_s/2\pi$) and the Brownian rotation of the organic groups (mainly CH_3 belonging to the oleic acid coating). Taking into account the blocking temperatures estimated by the DC magnetic measurements (see Chapter 2) and the muon Larmor frequency, one can easily calculate that the condition $\omega_L\tau_c \sim 1$ at T_c^{5F} and T_c^{7H} occurs because of the SPM spin blockage at $T_B^{\mu+}$ (Néel reversal with time τ_N).

Again, the dynamics of MNPs can be highlighted: for $T < T_B^{\mu+}$ the system is "seen" by muons in a blocked state, whereas for $T > T_B^{\mu+}$ the system results in a cooperative superparamagnetic state. The transition between the two states is gradually governed by the competition between the available thermal energy, the anisotropy barrier distribution and the interparticle interactions. As the muons access to a faster window time (in the LF applied in our case $\nu_L \sim 10^{-7} s^{-1}$) with respect to a DC magnetization measurements ($\nu \sim 0.1 - 10^2 s^{-1}$) one has $T_B^{\mu+} > T_B^{ZFC}$ (for comparison see table 3 Chapter 3 and table 4 Chapter 2).

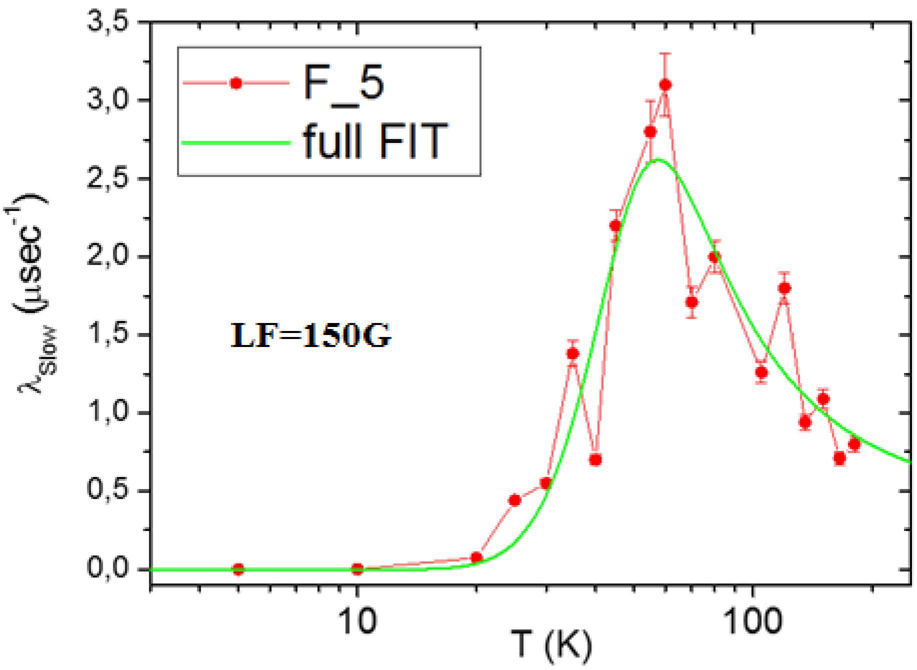

(a)

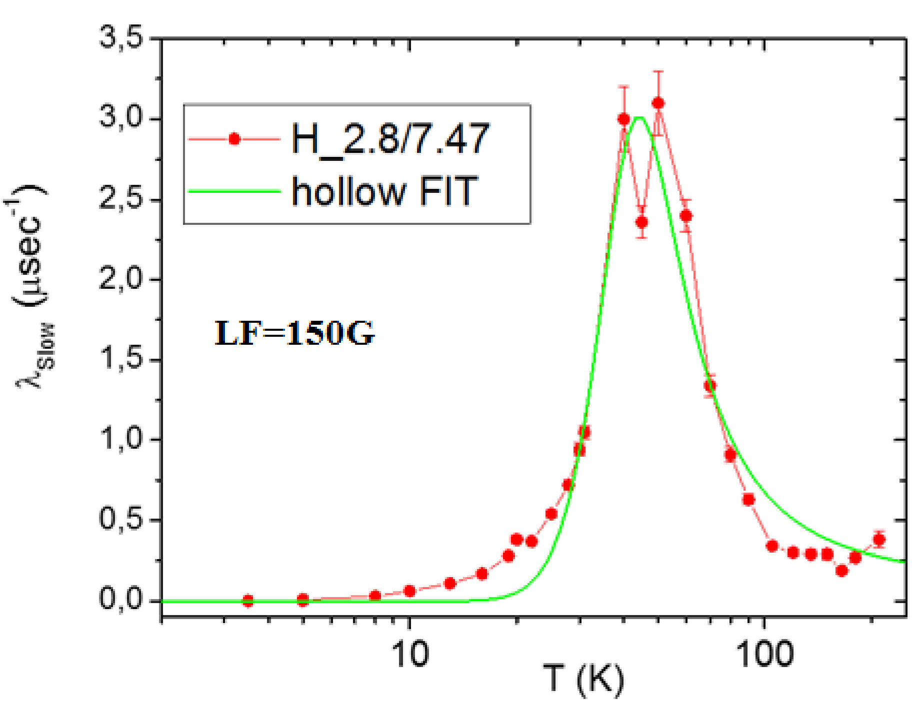

(b)

Figure 21 Relaxation rate λ_{Slow}(T) of (a) F_5 and (b) H_2.8/7 obtained from the fit of the muon asymmetries at different temperatures in a longitudinal field of 150G. The green curves are the best fits obtained for by means of equation (22). The fit parameters are reported in table 3.

Following well-assessed procedures reported in literature in case of spin freezing highlighted by NMR and μSR^{+} in molecular nanomagnets [99-100] and magnetic nanoparticles [93] we fitted the experimental λ_{Slow}(T) curves in the temperature range 5K<T<180K by means of the Bloembergen-Purcell-Pound (BPP) model [101]

$$\lambda(\mathrm{T}) = \frac{1}{T_1} = A\chi(T)T\frac{\tau_N}{1+\tau_N^2\omega_L^2}$$

(22)

where τ_N is the Néel time which is the dominating electronic correlation time in this temperature region and results to be related to the anisotropy barrier E_N by the Néel expression $\tau_N = \tau_{0,N}e^{(\frac{E_B}{K_BT})}$, A is the hyperfine constants and χ(T)T represents the effective magnetic moment of the system. In table 3 the parameters calculated from the fitting procedures of $\lambda_{Slow}(T)$ by means of (22) are summarized.

sample	***Field (G)***	***A (rad/s^2)***	***E_B^μ (K)***	τ_0^μ (*s*)	***T_B^μ(K)***
F_5	*150*	*(6.7±0.5)10^{11}*	*150±16*	*(5.6±1.5)10^{-9}*	58±5
H_2.8/7	*150*	*(7.7±0.4)10^{10}*	*172±10*	*(1.5±0.4)10^{-9}*	50±10

Tab.3 List of parameters extracted from the fit of experimental data λ vs T with Eq. (22). Columns, starting from the left: the external longitudinal applied field, the hyperfine constant A, the anisotropy barrier E_B, the attempt time τ_0 and the blocking temperature as seen by the muons.

Values of $\boldsymbol{\tau_0^{\mu}}$ are in the typical range of SPM coumpounds [74,96], and show a slightly slower spin dynamics at room temperature of the hollow nanoparticles with respect to the full. This is in agreement with the maximum relaxation rate's position which occurs at similar but lower temperature in H_2.8/7 (T_B^{μ}=50K) than in F_5 (T_B^{μ}=58K) and with the anisotropy energy barrier which is slightly higher in H_2.8/7 (E_B^{μ} =150K) than in F_5 (E_B^{μ} =172K).

It is worth to notice that it was observed just one peak in λ vs T, ascribed to the SPM spins, while the presence of disordered PM (surface) spins moving more rapidly, ideally resulting in a peak at low temperature, is not evident. On the other hand the lower values of the order parameter of H_2.8/7 with respect to F_5 over the whole T-range (already deduced from the hysteresis curves), were confirmed by the temperature behaviour of the local field. In this sense value of E_B^{μ} and T_B^{μ} in table 3 can be referred to the spins in the SPM state and thus compared to the DC magnetometry results of table 4, Chapter 2.

III.iii Conclusions

Here we demonstrated that μ^+SR can be used to unravel the effect of the hollow spin topology on the electronic correlation frequencies which dominate the spin dynamics of magnetic NPs in a wide range of temperature. To this aim we investigated the temperature and frequency evolution of the muon relaxation by means of longitudinal field (LF)-μ^+SR in the temperature range 2 K < T < 300 K on full and hollow monodisperse maghemite nanoparticles. At low temperature and weak applied longitudinal magnetic field we observed unprecedently reported coherent oscillations in the muon asymmetry, that reveal the presence of a local field felt by the muons implanted in the inner magnetic core of the nanoparticles. Thanks to high statistics, we were able to observe the local oscillating field induced by the blocked spins of the MNPs at low temperatures.

On the other hand, the dependence of the muon relaxation rate vs temperature allowed to characterize the system spin dynamics, that at T<300K can be reproduced by the well-known Bloemberger-Purcell-Pound model by assuming the Néel reversal time of the magnetization as dominating correlation time. This allowed to obtain information about the thermally activated correlation frequencies involved in the spin dynamics and probed at the measurement frequencies of the implanted muons. At low temperatures the relaxation is driven by the slowing down of the Néel reversal of the magnetization while at high temperatures the dynamics becomes superparamagnetic leading to a very slow muon relaxation. Moreover, despite the volume difference, the two samples display a similar blocking temperature as seen by the muon dynamics; in particular this experimental evidence is in agreement with the static investigation of Chapter 2.

CHAPTER 4:
FINAL REMARKS

This thesis has been developed within the framework of a general research concerning the chemico-physical of systems based on magnetic nanoparticles presenting different magnetic properties and spin topologies. In particular the experimental investigation and data analysis was focused on the effect of the hollow topology on the static and dynamic properties of magnetic nanoparticles. Hollow nanoparticle samples of maghemite (γ-Fe_2O_3) and magnetite (Fe_3O_4) have been investigated and full nanoparticle samples of the same batch were used as reference for the “bulk” superparamagnetic monodomain spin configuration. It is worth noticing that iron oxides with different spin topology have an important role in biomedicine other than recording and spintronics applications.

The static magnetic properties were investigated on powder samples by means of DC SQUID measurements of : (i) magnetization as a function on temperature in zero field cooled and field cooled conditions (H=5mT), in the temperature range of $2K<T<300K$; (ii) magnetization as a function of the external static magnetic field at two different temperatures (T=5K and T=300K) above and below the so-called blocking temperature, which defines the critical temperature at which half of the spin distribution is blocked in the time window of DC measurements.

From DC measurements, the hollow topology systems revealed the presence of more than one crystallographic domain with randomly oriented easy axes which “cooperate” to give an average saturation magnetization lower than the expected one (i.e. for a full nanoparticle having the same magnetic volume); the strength of this collective behaviour is tuned by the available thermal energy. As a consequence, the saturation magnetization and the blocking temperature extracted from the M vs T analysis were found not proportional to the magnetic volume of the hollow samples. This was ascribed to the presence of a high number of disordered spins in the outer, inner and inter-crystallites surfaces other than the presence of randomly orientated crystallographic axes. The thickness of the disordered surface layer was evaluated by previous Mossbauer analysis.

To prove the presence of two spin populations pertaining to bulk and surface spins and showing different dynamical behaviours, from ZFC and FC data we evaluated the energy barrier distributions (i.e. the blocking temperature distributions) for full and hollow samples. In the former case (full), one lognormal distribution was found while in the second case (hollow) two different lognormal distributions, with different mean blocking temperatures, showed up. In the last case, the distribution associated to the lower blocking temperature was ascribed to the surface spins and the mean blocking temperature resulted proportional to the mean canting angle calculated from the Mossbauer analysis, thus confirming the hypothesis of the lower blocking temperature of the “surface spins”. These spins are expected to be in a quasi-paramagnetic state (with low blocking temperature), being their exchange interaction much lower than the one among the core spins, this last having a higher coordination (higher number of neighbourhood in the environment).

The “local” spin dynamics were investigated by means of room temperature NMR-D profiles (on diluted samples, see Appendix B for the iron concentration) in the frequency range $10KHz < f < 100MHz$ and by means of MuSR spectroscopy measurements (on powder samples) performed at the GPS beamline of the Paul Scherrer Institute (Villigen, Switzerland), in the temperature range $2K<T<300K$ and under an external longitudinal static field of 150 G.

The NMR-D characterization of the hollow samples revealed the presence of a paramagnetic contribution at high fields (>30MHz), not visible in the NMR-D of the full samples, which was ascribed to disordered surface spins. To interpret the longitudinal relaxation experimental data a novel phenomenological model was proposed. The proposed model is a linear combination of the function describing the well-known superparamagnetic relaxation (Roch's model) and the one explaining the paramagnetic relaxation. As a first approximation, the weights of the linear combination were fixed at the same values obtained for the two energy barrier distributions obtained from the DC analysis cited above. All the longitudinal relaxometry profiles were successfully fitted with our model and the fitting procedures allowed the evaluation of the hyperfine coupling between the paramagnetic spins and the nuclear spins of the solution, which was found in the typical range of PM compounds.

The MuSR characterization was performed on a full (i.e F_5) and hollow (i.e. H_2.8/7.4) sample. Three different components in the asymmetry relaxation curves corresponding to 3 muon implantation sites, were observed. The muon asymmetry component corresponding to the lower relaxation rate λ_{slow} was measured over the whole temperature range and displayed a peak at a critical temperature T*. The λ vs T data were successfully fitted by means of a BPP model and the blocking temperature as seen by the muons ($T^* \sim T_B^{\mu+}$) was compared to the blocking temperature T_B^{ZFC} seen in DC measurements (i.e. where the ZFC magnetization curve exhibits a maximum). As the muons are a dynamical probe operating at frequencies higher than the DC SQUID, it was found that $T_B^{\mu+} > T_B^{ZFC}$. The values of $T_B^{\mu+}$ of F_5 and H_2.8/7.4 are equal in the error range, and the same behaviour can be observed for T_B^{ZFC}. These results tell us that the local dynamics data confirms the static data, a non trivial conclusion especially if one considerS the complicate spin topology for the investigated systems. Additionally, for the first time in a MuSR experiment on magnetic nanoparticles the presence of a static local field (H_{loc}) was observed when the temperature is decreased below T*, thus indicating a local magnetic order observable by muons. The local field was found to be lower in the hollow sample in the whole T-range, possibly due to the disordered spins which reduce the order parameter in these systems.

In conclusion this thesis gives new experimental evidences and a possible interpretation to the magnetic properties of hollow iron oxide magnetic nanoparticles.

APPENDIX A:

Measure of the self-diffusion coefficient of 1-octadecene

Pulsed field gradient NMR spectroscopy can be used to measure translational diffusion of molecules. By use of a gradient, the molecules can be spatially labeled i.e. marked depending on their position in the sample tube. If they move after this encoding during the following diffusion time Δ, their new position can be decoded by a second gradient. The measured signal is the integral over the whole sample volume and the NMR signal intensity is attenuated by a factor depending on the diffusion time Δ and the gradient parameters. This intensity change is described by:

$$I = I_0 e^{-D\gamma^2 g^2 \delta^2 (\Delta - \delta/3)}$$

where I is the observed intensity, I0 is the reference intensity (non-attenuated signal intensity), D is the diffusion coefficient, γ is the gyromagnetic ration of the observed nucleus, **g** the gradient strength, **δ** the length of the gradient and Δ the diffusion time. To simplify this equation some parameters are often combinedThe experiment on a 1-octadecente sample was performed in the Chemistry department of Università degli Studi di Milano, on a Bruker DRX400 equipped with a BBI probe.

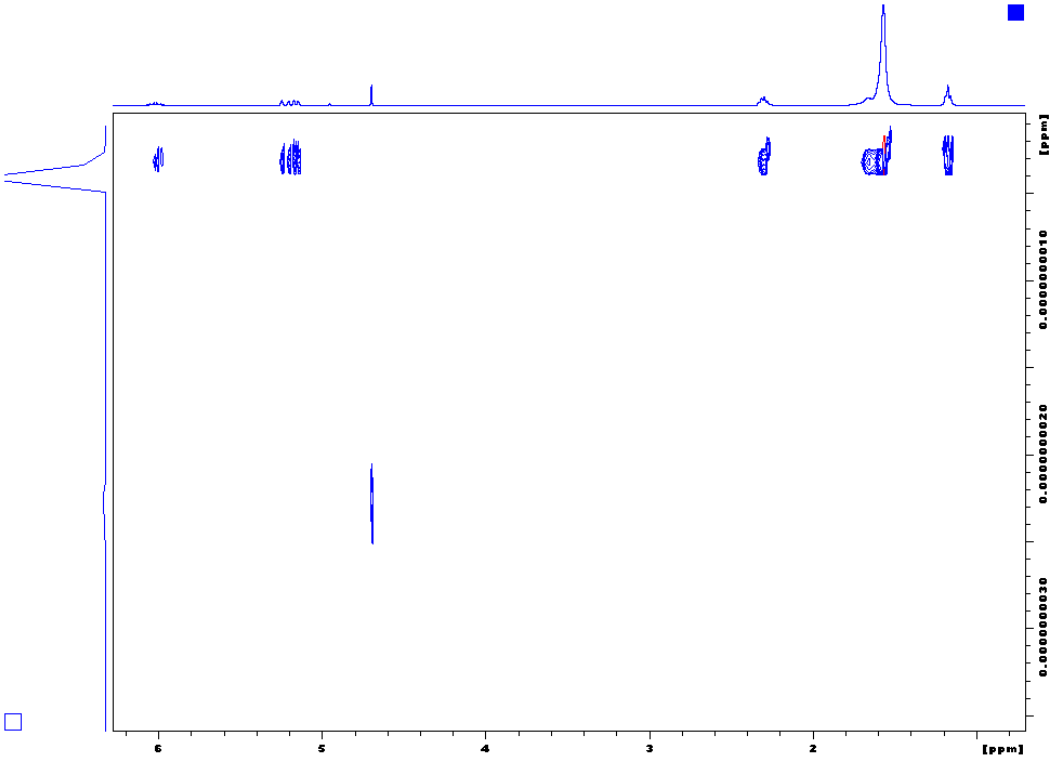

Figure A_1 ^{1}H-DOSY experiment performed on 1-octadecene with a reference of D_2O.

Figure A_1 show the DOSY experiment performed on 1-octadecene. The reference was put in a coaxial tube inside the sample. From the experimental data the self diffusion coefficient was calculated to be D=2.85x10-10 m2/s by means of (refer to figure A_2 for the data analysis).

$$D\ (m^2 s^{-1}) = -m/[-\gamma^2 \delta^2 (\Delta - \delta/3)]$$

where m is the angular coefficient of the line in figure A_2, $\Delta = 100\ ms$ and $\delta = 4\ ms$.

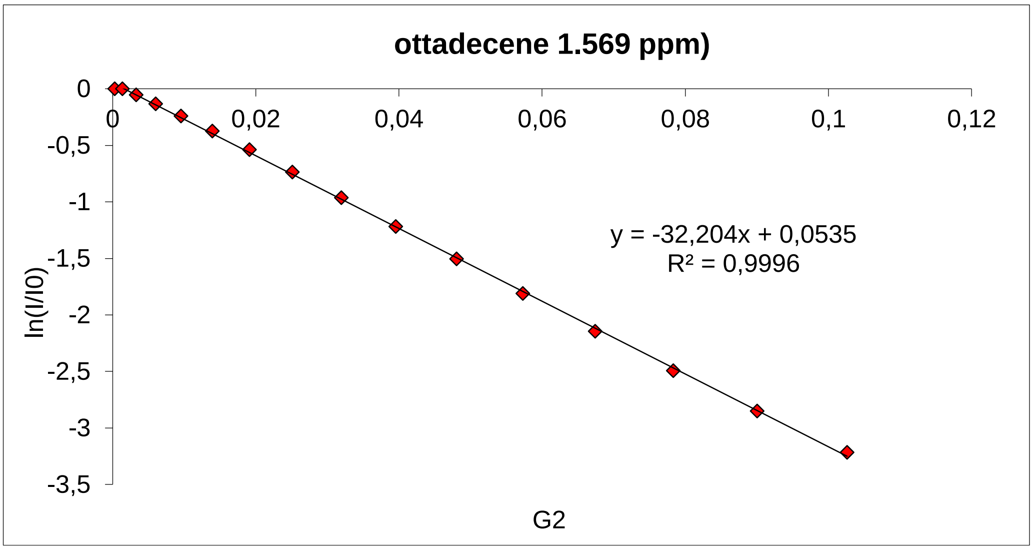

Figure A_2 Normalized NMR signal intensity in the DOSY experiment on 1-octadecene.

APPENDIX B

Evaluation of the iron concentration on F and H Sample

The evaluation of the iron concentration used to determine the relaxivity (relaxation rate normalized on iron concentration) was performed by an external industry's laboratory (i.e. S.P.S. Ecologia, Italy). The table reported here below contains the results. The concentration listed in table B_1 were used during the fit analysis of the NMRD profiles as a fixed parameter.

	F_5	**F_8.5**	**H_2.8/7.4**	**H_6/11**	**H_5/13**	**H_8/15**	**H_10/16**
[Fe](mg/l)	42	58	222	94	42	66	155

Table B_1 List of the iron concentration in mg/l of the solution measured by NMR relaxivity.

APPENDIX C

Instruments

The NMRD profiles were recorded in the NMR laboratory of the Università degli Studi di Milano. The NMR spectrometer works in a pulsed regime and in a wide range of field intensity (i.e. probing a wide range of ^{1}H nuclear frequency). Two different electromagnets were employed to cover the frequency range of 10 kHz - 10 MHz (low field) and 10 MHz - 60 MHz (high field) respectively. While in the high field (H > 0.1T) configuration the NMR signal is easily detected, when the proton Larmor frequency decrease below 4MHz the signal to noise ratio has to be increased by means of a fast field cycling (FFC) technique.
In the following paragraphs, the NMR spectrometer, the two electromagnets and the RF pulse sequences used to measure the longitudinal and transversal (i.e. T_1 and T_2) relaxation times, will be described .

NMR Spectrometer

In figure C_1(a) the blocks diagram of the employed spectrometer is shown. The blocks are named by alphabetic letters (A to I) and their function can be described as follow:

(A) *The synthesizer* generates the resonant radio frequency ω_{RF} with high stability and a precision of few Hz

The *gate* is able to shift the phase of the generated RF pulse in the xy plane (x, -x, y, -y) which results transversal with respect to the external applied field (z).

(B) The *gate* allows to modulate the pulse by the choosen RF frequency

(C) The *pulse programmer* generates and selects the time lenght and/or the shape of the RF pulse.

(D) The *pre-amplifier* gives the required amplitude to the transmitted RF pulse.

(E) The *duplexer* allows a bi-directional comunication between the coil containig the sample (F) and the spectrometer. In particular it separetes the transmitted exciting pulse to the received signal due to the proton relaxation.

(G) The two *mixers* multiply the nuclear magnetic relaxation signal coming from the sample by two pure oscillating signals dephased one with respect to each other by $\pi/2$.

(H) An *analogical to digital converter* (ADC) acquires the signal and send it to a *personal computer* PC (I) which elaborate the signal and control the spectrometer's parameters.

The *electromagnets* imposing the probing frequency, not included in the blocks diagram, offer a spatial homogeneity of 10 ppm (high frequency electromagnet) and of 40-60 ppm (low frequency electromagnet).

In resonance condition ($\omega_{RF} = \omega_{Larmor}$) the so-measured signal is called free induction decay (FID) whose amplitude at t = 0 is proportional to the net nuclear magnetization (M) generated by the electromagnet in the direction of its static magnetic fied. The time dependence of the FID contains informations about the longitudinal and transversal nuclear relaxation times. These last times (T_1 and T_2) allow to access indirectly the typical correlation times of the investigated system, probing the probability to find an electronic (the sample) spin oscillation resonant to the nuclear (the probe) spin oscillation ω_{Larmor}.

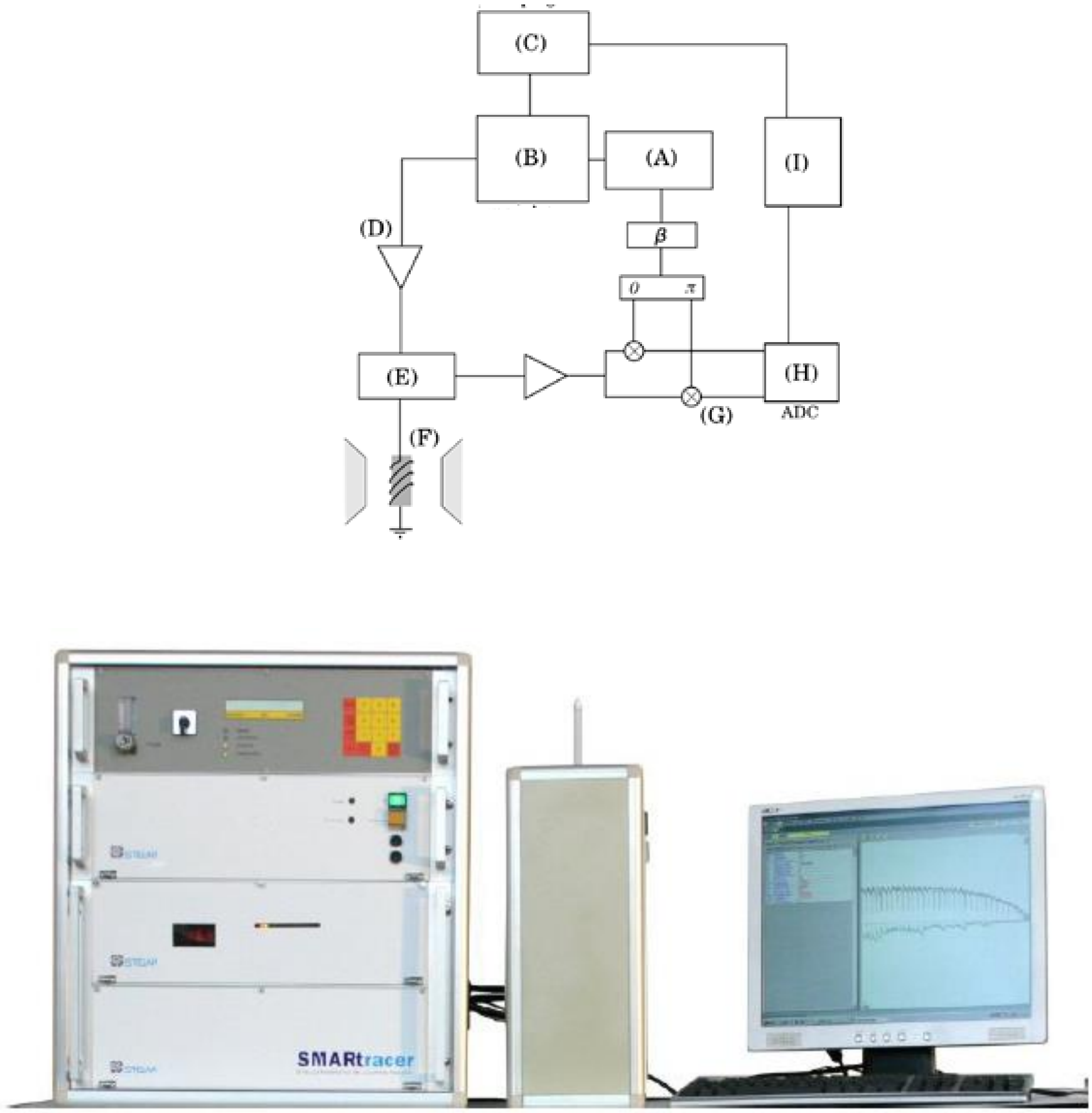

(a)

(b)

Figure C_1 Blocks diagram (a) and photograph (b) of the employed NMR spectrometer

T_1, T_2 Sequences

The longitudinal relaxation times T_1 measure the time required to the nuclear magnetization vector (**M**) to return back to the equlibrium imposed by the external static field after an external perturbation (ω_{RF}) occurs. Thetransversal relaxation time T_2 measures the dephasing of the nuclear spins.

So, in paricular T_1 measures the time required to **M** to rebuild up in the direction (z) of the external static field and T_2 measures the time required to **M** to become zero in the plane transversal to the static field (xy). Due to the quantum mechanical origin of the relaxation, the magnetization vector is not conserved during the relaxation so that $T_2 \leq T_1$ (i.e. the transversal relaxation is faster than the longitudinal one).

One has to keep in mind that since the receiver is connected to the coil, the acquisition of the relaxation signal is possible only in the transversal plane so that the measure of T_2 can be directly performed. In order to measure T_1 and to eliminate the field inhomogeneity which can affect T_2, dedicated pulse frequencies have to be applied. The time T_1 have been mesured by means of a saturation recovery (SR) sequence with the possibility to pre-polarize the sample (for frequencies < 4MHz). T_2 have been measured by means of a Carr-Purcell-Meiboom-Gill (CPMG) and of a pre-polarized spin echo (PP_SE) for high (i.e.f > 4 MHz) and low (i.e.f < 4 MHz) frequencies respectively.

A simple scketch of the above cited pulse sequences are listed below.

SR

(Saturation Recovery, T_1)

(a)

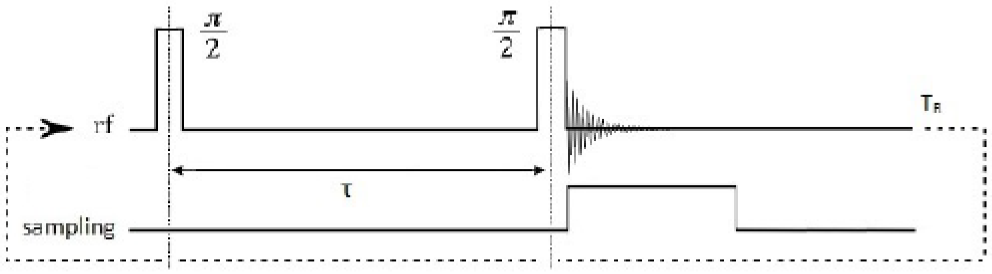

CPMG

(Carr-Purcell-Meiboom-Gill T_2)

(b)

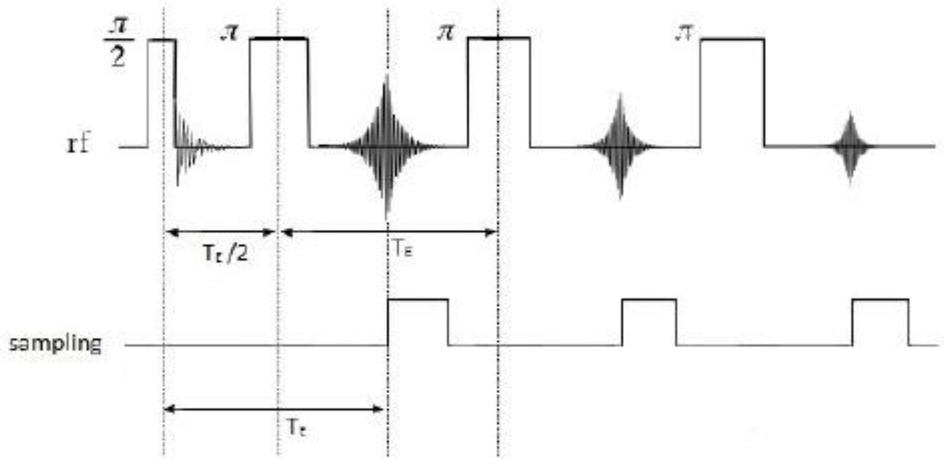

PP_SE

(Pre-Polarized Spin Echo, T_2)

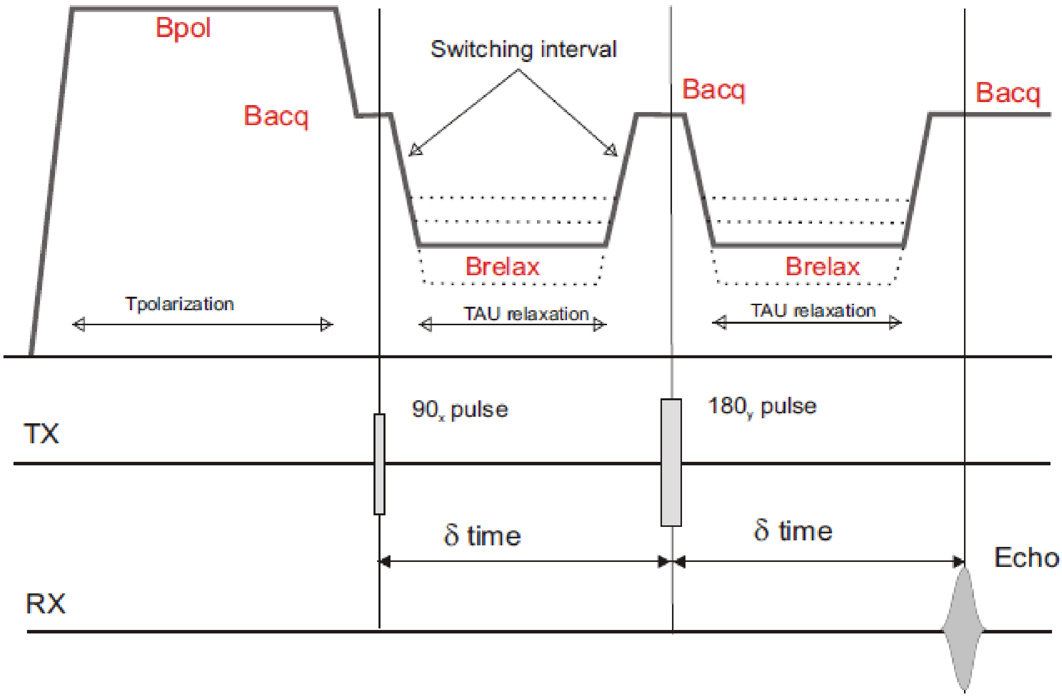

(c)

Figure C_2 (a) Saturation recovery (SR) sequence used to measure T_1 at high frequencies (i.e. $f > 4$MHz). In order to measure the T_1 at low frequencies (i.e. $f > 4$MHz) the same SR sequence was applied in a pre-polarized configuration (not shown). (b) CPMG sequence used to measure T_2 at high frequencies (i.e. $f > 4$MHz) and (c) pre-polarized spin echo used to measure T_2 at low frequencies (i.e. $f < 4$MHz).

Acknowledgments

We strongly acknoledge Dott. Davide Peddis *(ISM-CNR, Area della Ricerca Roma 1, 00016 Monterotondo Scalo, Rome, Italy)* not only for the samples synthesis but also for the TEM images and DC magnetic characterization of all the hollow samples and of the F_5 samples. We acknowledge Prof. M. Casula *(Dipartimento di Scienze Chimiche e Geologiche and INSTM, Università di Cagliari, Monserrato, Italy)* for the synthesis and TEM characterization of the F_8.5 samples. We acknowledge Dott. C. Innocenti (*Dipartimento di Chimica and INSTM, Università degli studi di Firenze, Sesto F.no, Italy*) and C. Sangregorio *(ICCOM-CNR and INSTM, Sesto F.no, Italy)* for the DC magnetic characterization of the F_8.5 sample. Last but not least we aknowledge Dott. D. Maggioni (*Dipartimento di Chimica, Univestità degli Studi di Milano, Italy*) for the mesurements she performed and which allowed the estimation of the 1-octadecene self-diffusion coefficient.

Bibliography

[1] Suber, L., and Peddis, D. Approaches to synthesis and characterization of spherical and anisometric metal oxide magnetic nanomaterials, in Magnetic Nanomaterials, Vol., 4, Wiley, Weinheim. (2010).

[2] Blundell, S. Magnetism in Condesed Matter, Oxford University Press, New York, (2003)..

[3] West, A. R. Solid State Chemistry and Its Applications, John Wiley & Sons, (1984).

[4] Morrish, A. H. The Physical Principles of Magnetism, Wiley, New York, (1965).

[5] Crangle, J. Solid State Magnetism, G. B. Edward Arnold, London, (1991).

[6] Leslie, D. L., Pelecky, R. D. R. (1996). Chem. Mater., **8**, 1770–1783. 40.

[7] Rondinone, A. J., Zhang, Z. J. Magnetic characterization, in Handbook Nanophase and Nanostructured Materials Vol. II, Kluwer Academic, New York (2000).

[8] Cannas, C., Peddis, D. La Chim. Ind (2012).

[9] Cannas, C *et al.* J. Nanopart. Res**., 8**, 255–267, (2006)..

[10] Peddis, D *et al.* G. Chem.–Eur. J., **15**, 7822–7829. (2009).

[11] Dormann, J. L., Fiorani, D., Tronc, E. Magnetic relaxation in fine particle systems, in Adances in Chemical Physics, Vol. XCVIII, New York (1997).

[12]Leslie-Pelecky and Rieke (1996)

[13] Peddis, D., Cannas, C., Musinu, A., Piccaluga, G. J. Phys. Chem. C, **112**, 5141–5147,(2008).

[14] Peddis, D *et al.* J. Phys. Chem. B, **112**, 8507– 8513, (2008)..

[15] Peddis, D *et al.* Nanotechnology, **21**, 125705. (2010).

[16] Trohidou, K. N. *et al.* Trans. Magn., **48**, 1305–1308. 34(2012)..

[17] Blaskov *et al.* J. Magn. Magn. Mater., **162**, 331–337, (1996)..

[18] A. E. Berkowitz, *et al.* Phys. Rev. Lett. **34**, 594 (1975)

[19] S. Linderoth, P. V. Hendriksen, F. Bo.dker, S. Wells, K. Davies, S. W. Charles, and S. Mo.rup, J. Appl. Phys. **75**, 6583 (1994)

[20] NBel L., J. Phys. Radium **15**, 225 (1954).

[21] A. Thiaville, J. Magn. Magn. Mat. **182**, 5 (1998).

[22] A. Thiaville, Phys. Rev. B **61**, 12221 (2000).

[23] L. NCel, Ann. Geophys. **5**, 99 (1949).

[24] L. NCel, C. R. Acad. Science 228, 664 (1949

[25] . P. Bean, J. Appl. Phys. 26, 1381 (1955).

[26] C. P. Bean and J. D. Livingstone, J. Appl. Phys. 30, 120s (1959)

[27] W. F. Brown, J. Appl. Phys. 30, **130s** (1959).

[28] W. F. Brown, J. Appl. Phys. **34**, 1319 (1963).

[29] W. F. Brown, Phys. Rev. **130**, 1677 (1963).

[30] W. T. Coffey, *et al.* Phys. Rev. B **52**, 15951 (1995).

[31] W. T. Coffey *et al.* Phys. Rev. Lett. **80**, 5655 (1998).

[32] I. Klik and L. Gunther, J. Stat. Phys. **60**, 473 (1990).

[33] I. Klik and L. Gunther, J. Appl. Phys. **67**, 4505 (1990).

[34] W. T. Coffey, Adv. Chem. Phys. **103**, 259 (1998).

[35] J. L. Dormann, D. Fiorani, and E. Tronc, Adv. Chem. Phys. **98**, 283 (1997).

[36] Frenkel J, Dorfman J., Nature;**126**:274 (1930).

[37] Kittel C. Phys Rev;**70**:965–71(1946)

[38] Ne´el L. Theorie Du Trainage Magnetique des feroomagnetiques en grain fins avec applications aux terres cuties. Ann Geophys **5**:99–136, (1949);.

[39] Dormann JL, Fiorani D, Tronc E. Advances Chemistry Physics, XCVIII. Wiley; (1997).

[40] Stoner EC, Wohlfarth EP. IEEE Trans Magn **27**:3475–518, (1991);.

[41] O’Grady K, Chantrell RW, El-Hilo M.J Magn Magn Mater **117**:21–8(1992).

[42] Meiklejohn WH, Bean CP. New magnetic anisotropy. Phys Rev **102**:1413–4, (1956);.

[43]. Grady KO, O’Grady K, Fernandez-Outon LEE, Vallejo-Fernandez G, O’Grady K.

[44]. Nogue´s J, Schuller IK. Exchange bias. J Magn Magn Mater;**192**:203–32 (1999).

[45] Berkowitz AE, Takano K. Exchange anisotropy a review. J Magn Magn Mater (1999).

[46].Malozemoff AP. Phys Rev B **35**:3679–82, (1987);.

[47] Nogue´s J, *et al.* Phys Rep; **422**:65–117 (2005).

[48]. Dormanni JL, Bessaist L, Fiorani D. J Phys C Solid State Phys**;21**:2015 (1988).

[49] Ali SR *et al.* Phys Rev B; **82**:020402(2010).

[50] Girgis E, *et al.* Phys Rev Lett ;**91**:187202 (2003).

[51] Laureti S *et al.* Phys Rev Lett **108**:77205, (2012).

[52] Suck SY et al. Appl Phys Lett;**95**:162503 (2009)

[53] O’Grady K, Chantrell RW. Sci. Rep.;**35**, p. 93–102 (1991).

[54] L. H. F. Andrade, *et. al.* Phys. Rev. Lett. **97**, 127401 (2006)

[55] Ana Balan, and Frithjof Nolting Phys. Rev. Lett. **112**, 107201 (2014)

[56] K. Komatsu *et. al*. Phys. Rev. Lett. **106**, 150603 (2011)

[57] J. Tejada, *et al.* Phys. Rev. Lett. **104**, 027202 (2010)

[58] A. Sukhov *et. al.* Phys. Rev. Lett. **102**, 057204 (2009)

[59] F. Gazeau *et. al.* Europhys. Lett., **40** (5), pp. 575-580 (1997)

[60] T. Hyeon, *et. al.* J. Am. Chem. Soc. **123**, 19798 2001.

[61] Saqlain A. *et. al.* Phys. Rev. B **92**, 094438 (2015)

[62] K. Parvin *et. al.*. JAP **95**, NUMBER 11;

[63] T N Shendruk *et. al.* Nanotechnology **18** 455704 (2007)

[64] A. Cabot, J. Am. Chem. Soc. **129**, 10358-10360 (2007)

[65] Smigelskas, A. D.; Kirkendall, E. O. *Trans. AIME* **171,** 130-142, (1947)

[66] E. V. Shevchenko, Adv. Mater. , **20,** 4323–4329 (2008)

[67] R. Xing, Nano Research **6**(1): 1–9 (2013)

[68] H. Khurshid *et al.* Appl. Phys. Lett. **101**, 022403 (2012)

[69] H. Kurshid *et al.* J. Appl. Phys. **115**, 17E131 (2014)

[70] G. Hassnain Jaffari J. Appl. Phys **107** , 013910 (2010)

[71] D.Goll *et al.* Phys. Rev. B **70**, 184432 (2004)

[72] A. Cabot *et al.* Phys. Rev. B **79**, 094419 (2009)

[73] H. Khurshid *et al.* scientific reports **5**:15054 (2014)

[74]] M. Basini et al. J. Chem. Phys. **146**, 034703 (2017)

[75] Singh *et al*.,Nano Reviews, **1**, 5358 (2010).

[76] P.Guardia *et al*. Chem. Commun. **46** 6108 (2010)

[77] P. Guardia *et al.* ACS Nano **6** (4), 3080 (2012)

[78] Chandra et al. J. Phys.: Condens. Matter 25 (2013) 426003

[79] Battle X. and Labarta A. J. of Physics D. : Applied Phys. **35**(6) R15 (2002)

[80] C. Moya J. Phys. Chem. C 2015, 119, 24142−24148

[81] A. H. Morrish. The Physical Principles of Magnetism (Wiley-IEEE Press), 2001.

[82] West F G 1961 *J. Appl. Phys.* **32** 249S

[83] E.C. Stoner and E.P. Wohlfarth Phiò.Trans. Roy Soc. Vol A249 p. 599, 1948

[84] F. Bloch, Phys. Rev. 70, 460 (1946)

[85] Roch *et al*., J. Chem. Phys.,, **110**, 5403, (1999).

[86]Gills P., Roch A. and Brooks R.A. Journal of Magnetic Resonance , **137**, 402 (1999)

[87] Lévy, M. et al. J. Phys. Chem. C **117**, 15369–15374 (2013).

[88] Solomon, Phys. Rev. 99, 559 (1955)

[89] N.J. Bloembergen, Chem. Phys. 27, 572 (1957)

[90] D. Procissi, *et al.*,Phys.Rev. B **3**, 184417 (2006)

[91] J. Lago *et al.* Phys. Rev. B **76**,064432 (2007)

[92] D. Procissi *et al.* Phys. Rev. B **80**, 094421 (2009)

[93] L. Bordonali *et al.* Phys.Rev. B **85**, 174426 (2012)

[94] T.Orlando *et al.* J. Appl. Phys.**119**, 134301(2016)

[95] A.Lascialfari P.Carretta NMR, Mosabauer and MuSR Specoscopy in molecular magnets

[96] L. Bordonali et al. Phys.: Condens. Matter, **25** 066008, (2013)

[97] R.N. Muller, Chem. Rev.**, 108**, 2064–2110 (2008)

[98] Igleasias O. and Labarta A Phys. Rev. B **63** 184416 (2001)

[99] "NMR in Magnetic Molecular Rings and Clusters", F. Borsa, A. Lascialfari, Y. Furukawa, ,pp.297-349 of the book "Novel NMR and EPR Techniques", eds.J. Dolinsek, M. Vilfan, S. Zumer, Springer (Berlin Heidelberg, (2006).

[100] F. Adelnia et al. J. Phys.: Condens.Matter **27**, 506001(2015)

[101] N. Bloengember, E. M. Purcell and R. Pound Phys. Rev, **75**, 7 ,679-712 (1948)

Publications

[1] Y. Gossuin,T. Orlando, M. Basini, D. Henrard, A. Lascialfari, C. Mattea, S. Stapf and Q. L. Vuong “NMR relaxation induced by iron oxide particles: testing theoretical models”” ,Nanotechnology **27**, 155706 (2016)

[2] T.Orlando, M.Albino, F.Orsini, C.Innocenti, M.Basini, P.Arosio, C.Sangregorio and A.Lescialfari. “On the magnetic anisotropy and nuclear relaxivity effects of Co and Ni doping in iron oxide nanoparticles”, J. Appl. Phys.**119**, 134301(2016)

[3] M. Basini,1 T. Orlando, P. Arosio, M. F. Casula, Davide Espa, Sergio Murgia,C. Sangregorio, C. Innocenti, and A. Lascialfari. “Local spin dynamics of iron oxide magnetic nanoparticles dispersed in different solvents with variable size and shape: A 1H NMR study”, J. Chem. Phys. **146**, 034703 (2017)

In submission

M.Basini et al. “Local Spin Dynamics in γ-Fe_2O_3 hollow nanoparticles unravelled by Muon Spin Relaxation”

THE JOURNAL OF CHEMICAL PHYSICS **146**, 034703 (2017)

Local spin dynamics of iron oxide magnetic nanoparticles dispersed in different solvents with variable size and shape: A ^{1}H NMR study

M. Basini,[1] T. Orlando,[2] P. Arosio,[1] M. F. Casula,[3] D. Espa,[3] S. Murgia,[3]
C. Sangregorio,[4] C. Innocenti,[5] and A. Lascialfari[1,6]
[1]*Dipartimento di Fisica and INSTM, Università degli Studi di Milano, Milano, Italy*
[2]*EPR Research Group, Max Planck Institute for Biophysical Chemistry, Göttingen, Germany*
[3]*Dipartimento di Scienze Chimiche e Geologiche and INSTM, Università di Cagliari, Monserrato, Italy*
[4]*ICCOM-CNR and INSTM, Sesto Fiorentino, Italy*
[5]*Dipartimento di Chimica and INSTM, Università degli studi di Firenze, Sesto Fiorentino, Italy*
[6]*Istituto di Nano scienze, CNR-S3, Modena, Italy*

(Received 5 August 2016; accepted 30 December 2016; published online 18 January 2017)

Colloidal magnetic nanoparticles (MNPs) based on a nearly monodisperse iron oxide core and capped by oleic acid have been used as model systems for investigating the superparamagnetic spin dynamics by means of magnetometry measurements and nuclear magnetic resonance (^{1}H NMR) relaxometry. The key magnetic properties (saturation magnetization, coercive field, and frequency dependent "blocking" temperature) of MNPs with different core size (3.5 nm, 8.5 nm, and 17.5 nm), shape (spherical and cubic), and dispersant (hexane and water-based formulation) have been determined. ^{1}H NMR dispersion profiles obtained by measuring the r_1 (longitudinal) and r_2 (transverse) nuclear relaxivities in the frequency range 0.01–60 MHz confirmed that in all samples the physical mechanisms that drive the nuclear relaxation are the Néel reversal at low temperature and the Curie relaxation at high frequency. The magnetization reversal time at room temperature extracted from the fitting of NMR data falls in the typical range of superparamagnetic systems (10^{-9}-10^{-10} s). Furthermore, from the distance of minimum approach we could conclude that water molecules do not arrive in close vicinity of the magnetic core. Our findings contribute to elucidate the local spin dynamics mechanisms in colloidal superparamagnetic nanoparticles which are useful in biomedical application as, e.g., contrast agents for magnetic resonance imaging. *Published by AIP Publishing.* [http://dx.doi.org/10.1063/1.4973979]

I. INTRODUCTION

In the last twenty years, superparamagnetic (SPM) iron oxide nanoparticles have captured the interest of multidisciplinary research activities and, recently, much attention has been devoted to understand the biomedical potential of theranostic systems based on magnetic nanoparticles (MNPs). The number of applications of magnetism to nanomedicine, including the well-known Magnetic Resonance Imaging (MRI), Magnetic Fluid Hyperthermia (MFH), cell separation, biosensing, and cellular functionalities study, is rapidly growing.[1–8] Though MNPs with different morphologies have been developed for biomedical applications, a full comprehension of the physical mechanisms and particularly the spin dynamics in the presence of biological media and related to their size, shape, coating, and dispersant has not been achieved yet. On the other hand, these morphological characteristics are crucial to determine their efficacy as contrast agents (CAs) in MR images quantified by an increase of the nuclear relaxation rate (referred to as nuclear relaxivity) of the ^{1}H nuclei contained in the human body.[9] The achievement of a higher nuclear relaxivity leads to a better contrast in the images and allows us also to envisage a reduction of the maximum dose injectable in living beings, a crucial issue for their safety. Both applied and fundamental[10–13] current researches on superparamagnetic ferrite-based CAs are therefore often devoted to understand the physical mechanisms of enhancement of the nuclear relaxation rates and to develop physical models able to predict the design of MNPs with optimized features. Within this framework, it is crucial to study the influence of the main MNP microscopic characteristics like size, shape, and composition of the magnetic core, surface coating, and the dispersant on the magnetic properties and on the nuclear magnetic resonance (NMR) relaxation rates. This task is very hard to achieve because of the mutual dependence of the above parameters and the data in the literature are very often difficult to compare.

With the present work we aim at contributing to clarify the influence of some MNPs properties, like size, shape, and dispersant on the nuclear longitudinal (r_1) and transversal (r_2) relaxivities and on the dynamical magnetic properties of colloidal suspensions. For this purpose, we performed ^{1}H nuclear magnetic resonance dispersion (NMR-D) and DC/AC magnetization measurements on iron-oxide based nanocrystals synthesized by high temperature colloidal routes. To study the role of the core size, we investigated nearly spherical MNPs with three different sizes, whereas to take into account the effect of the shape, MNPs with the same volume and different morphology (spherical and cubic) were considered. Moreover, in order to study the effect of the dispersing media on the contrast efficiency, the same sample was suspended either in an organic non-polar solvent (hexane) or in water, without removing the ligand directly attached at the surface of the inorganic core.

IOP Publishing Nanotechnology

Nanotechnology **27** (2016) 155706 (11pp) doi:10.1088/0957-4484/27/15/155706

NMR relaxation induced by iron oxide particles: testing theoretical models

Y Gossuin[1], T Orlando[2], M Basini[3,4], D Henrard[1], A Lascialfari[3], C Mattea[5], S Stapf[5] and Q L Vuong[1]

[1] Biomedical Physics Department, University of Mons, 24, Avenue du Champ de Mars, B-7000, Mons, Belgium
[2] Department of Physics, University of Pavia, Via Bassi 6, I-27100 Pavia, Italy
[3] Department of Physics, Università degli studi di Milano and INSTM Unit, Via Celoria 16 I-20133 Milano, Italy
[4] CNR Nano S3 Via Campi 213/A, 41125 Modena, Italy
[5] Technische Universität Ilmenau, Fakultät für Mathematik und Naturwissenschaften, FG Technische Physik II/Polymerphysik, PO Box 100 565, D-98684 Ilmenau, Germany

E-mail: yves.gossuin@umons.ac.be

Received 19 October 2015, revised 25 January 2016
Accepted for publication 9 February 2016
Published 2 March 2016

Abstract

Superparamagnetic iron oxide particles find their main application as contrast agents for cellular and molecular magnetic resonance imaging. The contrast they bring is due to the shortening of the transverse relaxation time T_2 of water protons. In order to understand their influence on proton relaxation, different theoretical relaxation models have been developed, each of them presenting a certain validity domain, which depends on the particle characteristics and proton dynamics. The validation of these models is crucial since they allow for predicting the ideal particle characteristics for obtaining the best contrast but also because the fitting of T_1 experimental data by the theory constitutes an interesting tool for the characterization of the nanoparticles. In this work, T_2 of suspensions of iron oxide particles in different solvents and at different temperatures, corresponding to different proton diffusion properties, were measured and were compared to the three main theoretical models (the motional averaging regime, the static dephasing regime, and the partial refocusing model) with good qualitative agreement. However, a real quantitative agreement was not observed, probably because of the complexity of these nanoparticulate systems. The Roch theory, developed in the motional averaging regime (MAR), was also successfully used to fit T_1 nuclear magnetic relaxation dispersion (NMRD) profiles, even outside the MAR validity range, and provided a good estimate of the particle size. On the other hand, the simultaneous fitting of T_1 and T_2 NMRD profiles by the theory was impossible, and this occurrence constitutes a clear limitation of the Roch model. Finally, the theory was shown to satisfactorily fit the deuterium T_1 NMRD profile of superparamagnetic particle suspensions in heavy water.

S Online supplementary data available from stacks.iop.org/NANO/27/155706/mmedia

Keywords: iron oxide particles, superparamagnetic particles, NMR relaxation theory, MRI contrast agent

(Some figures may appear in colour only in the online journal)

JOURNAL OF APPLIED PHYSICS **119**, 134301 (2016)

On the magnetic anisotropy and nuclear relaxivity effects of Co and Ni doping in iron oxide nanoparticles

T. Orlando,[1,2,a)] M. Albino,[3] F. Orsini,[4] C. Innocenti,[3] M. Basini,[4,5] P. Arosio,[4]
C. Sangregorio,[3,6] M. Corti,[1] and A. Lascialfari[4,5]
[1]*Department of Physics, Università di Pavia, and Consorzio INSTM, Pavia 27100, Italy*
[2]*Research Group EPR Spectroscopy, Max Planck Institute for Biophysical Chemistry, Göttingen 37077, Germany*
[3]*Department of Chemistry "Ugo Schiff," Università di Firenze, and Consorzio INSTM, Sesto Fiorentino 50019, Italy*
[4]*Department of Physics, Università degli Studi di Milano, and Consorzio INSTM, Milano 20133, Italy*
[5]*CNR-S3, Istituto di Nanoscienze, Modena 41125, Italy*
[6]*CNR-ICCOM and Consorzio INSTM, Sesto Fiorentino 50019, Italy*

(Received 30 October 2015; accepted 19 March 2016; published online 1 April 2016)

We report a systematic experimental study of the evolution of the magnetic and relaxometric properties as a function of metal (Co, Ni) doping in iron oxide nanoparticles. A set of five samples, having the same size and ranging from stoichiometric cobalt ferrite ($CoFe_2O_4$) to stoichiometric nickel ferrite ($NiFe_2O_4$) with intermediate doping steps, was *ad hoc* synthesized. Using both DC and AC susceptibility measurements, the evolution of the magnetic anisotropy depending on the doping is qualitatively discussed. In particular, we observed that the height of the magnetic anisotropy barrier is directly proportional to the amount of Co, while the Ni has an opposite effect. By Nuclear Magnetic Resonance Dispersion (NMR-D) experiments, the experimental longitudinal r_1 and transverse r_2 relaxivity profiles were obtained, and the heuristic theory of Roch *et al.* was used to analyze the data of both r_1 and, for the first time, r_2. While the experimental and fitting results obtained from r_1 profiles were satisfying and confirmed the anisotropy trend, the model applied to r_2 hardly explains the experimental findings. © *2016 AIP Publishing LLC.* [http://dx.doi.org/10.1063/1.4945026]

I. INTRODUCTION

Magnetic nanostructured materials usually display physical properties that are significantly different from the ones of the bulk. In ferro- or ferrimagnetic nanoparticles (NPs), the multi-domain spin arrangement typical of the bulk ferromagnets is absent, and the energy equilibrium configuration favours a single magnetic domain. As a consequence, the spins inside each NP are aligned along a particular direction and give rise to a large magnetic moment, which can be thought as a "superspin."

Their basic properties have been studied both theoretically and experimentally since the 1950s[1,2] but, in the last two decades, the evolution of the synthesis techniques allowed obtaining excellent quality monodispersed samples, having a well-defined size and shape. This allowed to explore and understand the physical phenomena at the nanoscale.[3] At the same time, the possibility to coat the magnetic nanoparticles with different kind of organic materials opens the possibility to use them in several state-of-the-art biomedical and technological applications.

Among the magnetic materials, iron oxides, such as magnetite (Fe_3O_4) or maghemite (γ-Fe_2O_3), are generally used as magnetic core, being the only ones which have been already approved by U.S. Food and Drug Administration (FDA) and European Medicines Agency (EMA).[4] These systems can help in various aspects of clinical practice,[5,6] working as contrast agents in magnetic resonance imaging (MRI),[7,8] drug carriers in magnetic transport,[9] or therapeutic agents in magnetic fluid hyperthermia (MFH).[10] Furthermore, new perspectives are opening in the field of the multifunctional magnetic nanostructures, which can be used simultaneously for different tasks.

Nevertheless, even if novel synthesized nanostructures are able to successfully accomplish one or two tasks, a real multifunctional object has not been completely realized yet. Consequently, the research of new materials whose properties can be properly tailored is of great interest. To this aim, the possibility to dope the iron oxide magnetic core with transition metal ions, obtaining optimized magnetic properties, can boost the use of nanoparticles for such applications.[11,12] In particular, a greater magnetization can improve the performance in magnetic transport, a high transverse nuclear relaxation rate brings to a better image contrast, while the kind of magnetic ion, the coating, and particularly the size are critical parameters for all applications.

The doping of the ferrite magnetic core with high anisotropy metal ions can be a feasible strategy. Several iron oxide nanostructures doped with cobalt, zinc, or gadolinium have been already synthesized and investigated,[13–17] but a complete and systematic study on the effect of Co and Ni doping on the magnetic properties is still missing. In order to address this issue, five cobalt and nickel substituted ferrite ($Co_xNi_yFe_{3-x-y}O_4$) nanoparticles with fixed size were synthesized, using a step-by-step doping, from stoichiometric Co-ferrite to stoichiometric Ni-ferrite.

[a)] Electronic mail: tomas.orlando@mpibpc.mpg.de